ULTRASHORT-LASER-PULSE MULTI-PHOTON EXCITATION SCHEMES FOR COMBUSTION DIAGNOSTICS

A Dissertation

by

AYUSH JAIN

Submitted to the Office of Graduate and Professional Studies of
Texas A&M University
in partial fulfillment of the requirements for the degree of

DOCTOR OF PHILOSOPHY

Chair of Committee,	Waruna D. Kulatilaka
Committee Members,	Eric L. Petersen
	Dorrin Jarrahbashi
	Simon W. North
Head of Department,	Andreas A. Polycarpou

August 2020

Major Subject: Mechanical Engineering

ABSTRACT

Laser-based diagnostic approaches using ultra-short femtosecond (fs) laser pulses is a promising method for investigating complex chemically reacting flow fields such as flames. Femtosecond pulses offer several advantages over traditionally used nanosecond (ns) and picosecond (ps) pulses because of their broad spectral bandwidth, high peak power, and high repetition rates. Thus, the objective of this thesis research is to investigate methodologies to extend the applications of ultrashort, fs-pulse-based laser-induced fluorescence (LIF) techniques to imaging studies in realistic flame environments. This thesis consists of four main research tasks to understand the importamce of the detection of H-atom and OH radicals in combustion systems.

The first task was to understand the role of H-atoms in soot formation by implementing fs two-photon LIF (fs-2pLIF) imaging. The previously demonstrated H-atom 2pLIF scheme (λ = 205 nm) in laminar methane/air flames was extended to the harsh environment of heavily sooting flames for the first time.

The second task was to explore the applicability of fs imaging schemes in practically relevant hardware containing thick optical windows by using fs 3-photon LIF (fs-3pLIF) detection of H-atoms. A detailed 2pLIF vs 3pLIF comparison was performed to characterize different levels of photolytic production, photoionization, and stimulated emission interferences. To the best of our knowledge, the H-atom 3pLIF scheme using λ = 307.7-nm photons was realized for the first time during this work.

In the third task, the extension of fs LIF methods for simultaneous multi-species detection using a single laser pulse by demonstrating H-atom and OH radicals imaging was achieved using the excitation wavelength of $\lambda = 307.7$ nm.

In the last part of this thesis research, a more efficient wavelength generation scheme for acquiring high-energy tunable fs laser pulses was developed via direct frequency conversion for fs LIF imaging applications with increased dimensionality. The availability of high pulse energy is important for diagnosis in practical combustion systems to account for numerous transmission losses as well as increase the size of the field of view to discern turbulent structures.

The above developments and the associated results discussed in this thesis is a significant step forward in implementing ultrashort pulse laser imaging techniques of intermediate chemical species for practically relevant combustion studies.

DEDICATION

To my parents, for all their love and support and putting me through the best education possible. I am indebted to their sacrifices and I would not have simply been where I am today without them.

ACKNOWLEDGMENTS

While thinking back with gratitude on the wonderful time I spent at Texas A&M University, I realize that the work described in this thesis could not have been completed without the support of my supervisor and exemplary colleagues with whom I was fortunate to work with. I would like to express my profound and most sincere appreciation for my thesis supervisor Dr. Waruna D. Kulatilaka for his careful guidance and continuous encouragement during the entire period of the thesis. I am grateful to him for providing me the freedom to work on this topic and for being a great mentor and motivator. I would also like to thank Drs Eric Petersen, Dorrin Jarrahbashi, and Simon North for serving on my advisory committee, and providing me numerous academic and research guidance.

I would like to thank my parents for their sacrifices and guidance, without their support I couldn't have achieved anything. I am also very thankful to my brother for continuously supporting and encouraging me in different phases of life.

It was a pleasure to be associated with Optical Diagnostics and Imaging Laboratory, here at Texas A&M University. I would like to thank all my colleagues, Pradeep Parajuli, Christian Schweizer and William Swain for helping me in all stages of my experimental work. I would like to especially thank Dr. Yejun Wang for motivating and guiding me throughout my thesis.

I would like to take this opportunity to thank my friends, here in College Station, particularly my roommate Ajinkya Deshpande for his continuous support in all the phases and for cherishing some wonderful memories over the past four years. I would also like to

thank my friends Nimish Kumar, Abhinav Gupta and Anubhav Vardhan for their motivation and belief in me.

Lastly, a very sincere and special thanks to my friend Ishan Tyagi, for being there as a mentor, guide and friend, without whose help and assistance, things would have been very difficult.

CONTRIBUTORS AND FUNDING SOURCES

Contributors

This work was supervised by a dissertation committee consisting of Dr. Waruna Kulatilaka, Dr. Eric Petersen and Dr. Dorrin Jarrahbashi of the Department of Mechanical Engineering, and Dr. Simon North of the Department of Chemistry.

All work for the dissertation was completed by the student, in collaboration with Dr. Yejun Wang, Pradeep Parajuli, Christian Schweizer and William Swain of the Department of Mechanical Engineering.

Funding Sources

This research was funded by grants from the National Science Foundation (NSF), Combustion, Fire and Plasma Systems Program, Office of Naval Research (ONR). The facilities support from the Texas A&M Engineering Experimental Station Turbomachinery Laboratory (TEES-TL) is also highly acknowledged.

Ayush Jain was also supported by the Ralph E. James Fellowship and the Emil Buehler Aerodynamic Analog Fellowship during this period.

The contents are solely the responsibility of the authors and do not necessarily represent the official views of NSF, ONR, or TEES-TL.

NOMENCLATURE

λ	Wavelength
H	Hydrogen atom
O	Oxygen atom
N	Nitrogen atom
CO	Carbon monoxide
NO	Nitrous oxide
OH	Hydroxyl radical
LIF	Laser Induced Fluorescence
ns	Nanosecond
fs	Femtosecond
fs-2pLIF	femtosecond two photon Laser Induced Fluorescence
fs-3pLIF	femtosecond three photon Laser Induced Fluorescence
S/N ratio	Signal to noise ratio
PMT	Photo-multiplier tube
ICCD	Intensified Charge Coupled Device
CMOS	Complementary Metal-Oxide Semiconductor
UV	Ultra-violet
VUV	Vacuum Ultra-violet
DUV	Deep Ultra-violet
2p	Two-photon
3p	Three-photon

Φ	Equivalence ratio
LII	Laser Induced Incandescence
LE	Laser Extinction
PICLS	Photo-Ionization Controlled Loss Spectroscopy
LIGS	Laser Induced Grating spectroscopy
2P4WMS	Two-photon four wave mixing spectroscopy
CWMT	Coherent Wave Mixing Techniques
SHG	Second Harmonic Generation
THG	Third Harmonic Generation
FHG	Fourth Harmonic Generation

TABLE OF CONTENTS

Page

ABSTRACT ii

DEDICATION iv

ACKNOWLEDGMENTS v

CONTRIBUTORS AND FUNDING SOURCES vi

NOMENCLATURE vii

TABLE OF CONTENTS x

LIST OF FIGURES xii

LIST OF TABLES xvii

1. INTRODUCTION 1

1.1 Motivation and Challenges 1
1.2 Laser-Based Imaging Diagnostics 3
1.3 Ultra-short Femtosecond Pulse Based Imaging in Combustion 4
1.4 Dissertation Outline 5

2. LITERATURE REVIEW 8

2.1 Selection Rules 8
2.1.1 Selection Rules for Atomic Spectroscopy 8
2.1.2 Selection Rules for Molecular Spectroscopy 9
2.2 Laser-Induced Fluorescence 10
2.2.1 Single-photon LIF Detection 12
2.2.2 Multi-Photon LIF Detection of Atomic Species 13
2.2.3 Prior Work on H-atom Detection 15
2.2.4 Prior Work on OH Radicals Detection 25
2.3 Soot Imaging via Laser-Induced Incandescence 33
2.3.1 Role of H-atoms in PAHs formation 39
2.4 High-Speed Laser Diagnostics Instrumentation 40
2.4.1 Fundamentals of Femtosecond Laser Systems 40

2.4.2 High-Speed Imaging Systems 43

3. ROLE OF ATOMIC HYDROGEN CONCENTRATION ON SOOT FORMATION 44

3.1 Experimental Details and Procedure 45
3.2 Results and Discussion 49
3.3 Summary 58

4. THREE-PHOTON LIF DETECTION OF ATOMIC HYDROGEN 59

4.1 Multi-Photon Excited H-atom Detection 59
4.2 Comparison of 2pLIF and 3pLIF detection schemes 64
4.2.1 Related Instrumentation 64
4.2.2 Results and Discussion 66
4.3 H-atom Detection in Adiabatic Flames via 3pLIF 73
4.3.1 Experimental Details 73
4.3.2 Results and Discussion 74
4.4 Summary 81

5. SIMULTANEOUS IMAGING OF ATOMIC HYDROGEN AND HYDROXY RADICALS 83

5.1 H-atom and OH Radical Excitation Schemes 84
5.2 Related Instrumentation for OH Imaging 85
5.3 Results and Discussion 88
5.4 Summary 95

6. IMAGING APPLICATIONS OF DIRECT FREQUENCY CONVERSION SYSTEMS 96

6.1 Frequency Tripling and Quadrupling Stage 98
6.2 Hydroxyl Radical Imaging in Turbulent Diffusion Flames 103
6.3 Atomic Carbon and Oxygen Detection 115
6.3.1 Atomic Carbon (C-atom) Detection 115
6.3.2 Atomic Oxygen (O-atom) Detection 118
6.4 Summary 120

7. CONCLUSION AND RECOMMENDATION FOR FUTURE WORK 121

7.1 Conclusion 121
7.2 Recommendation for Future Work 123

REFERENCES 125

LIST OF FIGURES

Page

Figure 1.1: Dissertation outline.....5

Figure 2.1: Laser-Induced Fluorescence scheme shown in (a) Fluorescence emission lines resulting in an emission spectrum (b) Fluorescence excitation resulting in an excitation spectrum reprinted from [7].....11

Figure 2.2: Energy level diagram showing different process that occurs along with LIF. 12

Figure 2.3: Multi-photon excitation schemes shown for different atoms reprinted from [8] 14

Figure 2.4: Multi-photon excitation schemes in H-atom reprinted from [9].....15

Figure 2.5: H-atom number density as a function of HAB obtained for PICLS and LIF at $\Phi = 1.0$ in H_2/ O_2/ N_2 flame at a pressure of 20 Torr rerinted from [14].....17

Figure 2.6: Simultaneous complicating processes in LIF detection.....18

Figure 2.7: Intensity dependence of SE (triangles) and LIF (circles) at $\Phi = 0.6$ at 72-torr in H_2/O_2/Ar flame reprinted from [11].....19

Figure 2.8: Forward and backward lasing SE in CH_4/air flame reprinted from [19].....20

Figure 2.9: 2p excitation schemes of Kr, H-atom and N-atom reprinted from [21] 21

Figure 2.10: Comparison of nanosecond (left) and picosecond (right) pulses for H detection in $CH_4/O_2/N_2$ jet flame reprinted from [26].....22

Figure 2.11: Peak-normalized H distribution profiles in $CH_4/O_2/N_2$ flame using femtosecond laser pulses different pulse energies reprinted from [27]. 23

Figure 2.12: 2-D single laser shot image of H-atom in premixed Bunsen jet flame obtained using direct frequency quadrupling reprinted from [31].....24

Figure 2.13: Schematic of different excitation schemes in OH radical.....26

Figure 2.14: Excitation and detection parameters for OH fluorescence measurement reprinted from [34].....27

Figure 2.15: Schematic of the experimental apparatus for OH-PLIF and PAH-PLIF measurements in piloted spray flames reprinted from [54].....30

Figure 2.16: Simultaneous single-laser-shot PLIF images of PAH and OH in R1 and R2 for commercial kerosene and its surrogate reprinted from [54] 31

Figure 2.17: Broadband spectrum of the fs laser pulse (dotted line), the calculated OH-LIF excitation spectrum obtained at 2200 K and 1 atm using the LIFBASE software package reprinted from [55].....32

Figure 2.18: Spectral response of the normalized LII signal at an excitation wavelength of 1064-nm reprinted from [68].....35

Figure 2.19: Schematic of soot formation in flame reprinted from [97].....36

Figure 2.20: 2-D images of LIF and soot volume fraction (Fv) in diesel and surrogate liquid spray flames reprinted from [103] 37

Figure 2.21: (a) LIE (LII + LIF) spectra at 3 different excitation wavelengths. (b) LIF emission spectra at 355 and 532-nm reprinted from [113] 38

Figure 2.22: Schematic of the laser assembly 41

Figure 3.1: Schematic of (a) LII and (b) fs-2pLIF experimental systems for obtaining f_V and relative [H], respectively, in rich C_2H_4/air flames stabilized over a modified McKenna flat-flame burner reprinted from [119].....46

Figure 3.2: Digital images of series of flames over the McKenna burner with an axisymmetric disc mounted above reprinted from [119].....49

Figure 3.3: A sample OH PLIF image recorded at Φ=1.0 flame reprinted from [119]....49

Figure 3.4: OH-PLIF signal intensity and calculated equilibrium [OH] along with measured flame temperatures as a function of Φ reprinted from [119].....50

Figure 3.5: f_v as a function of laser fluence for Φ = 2.8 and 3.0 recorded using excitation wavelength of 1064 nm reprinted from [119] 51

Figure 3.6: 2-D f_v images obtained using 1064-nm LII experiments at different Φ reprinted from [119] 52

Figure 3.7: Variation of f_v as a function of Φ, obtained using three LII schemes reprinted from [119] 54

Figure 3.8: Variation of measured and equilibrium H-atom LIF signals, together with experimental f_v as a function of Φ reprinted from [119] 55

Figure 3.9: Variation of H-atom LIF signal and f_v as a function of HAB reprinted from [119] 56

Figure 4.1: Energy level diagram for H-atom 60

Figure 4.2: Schematic of the experimental apparatus reprinted from [132] 65

Figure 4.3: Dependence of 2pLIF and 3pLIF signals as a function of laser energy. Solid lines represent the curve fits given by the shown equations reprinted from [132] 66

Figure 4.4: H-atom LIF line profiles as a function of distance from the center of the burner, for different laser energies. (a) 2pLIF at HAB = 5 mm, (b) 2pLIF at HAB = 10 mm, (c) 3pLIF at HAB = 5 mm, and (d) 3pLIF at HAB = 10 mm. 2pLIF profiles corresponding to 4μJ/pulse cases are also overlaid in (c) and (d) for easy comparison reprinted from [132] 68

Figure 4.5: 2-photon stimulated emission profiles as a function of laser power at HAB = 5 mm and 10 mm. Solid lines are smoothing spline fits to guide the eye reprinted from [132] 71

Figure 4.6: 2pLIF and 3pLIF H number density as a function of Φ reprinted from [132] 71

Figure 4.7: 3pLIF signal intensity as a function of excitation wavelength in H_2/air flame 74

Figure 4.8: Variation of 3pLIF signal intensity and # on-CCD accumulations 75

Figure 4.9: Variation of LIF signal as a function of laser power in H_2/air flame 76

Figure 4.10: Vertical H mole fraction profiles along the centerline of the burner for a series of flames ranging from lean (Φ = 0.8) to very rich (Φ = 2.10). Calculated H mole fraction using numerical modeling code data were extracted from [23] 77

Figure 4.11: Comparison of experimental H-atom mole fraction with equilibrium calculations and numerical data calculation at (a) 30-mm HAB and (b) 50-mm HAB 79

Figure 5.1: Energy level diagrams showing excitation and emission schemes for (a) OH-LIF, and (b) H-atom 3pLIF 84

Figure 5.2: Schematic representing the experimental apparatus 87

Figure 5.3: OH and H excitation scan along with laser beam profile and OH simulated spectra 89

Figure 5.4: Experimental and calculated OH emission spectra from the v'=0 → v"=0 band of OH. The root mean square error is shown on the top 89

Figure 5.5: Variation of OH LIF and H-atom 3pLIF signal as a function of laser pulse energy 91

Figure 5.6: (a) and (c) OH number density in CH_4/Air and C_2H_4/Air flame respectively; (b) and (d) H-atom number density in CH_4/Air and C_2H_4/Air flame respectively along with calculated equilibrium values 91

Figure 5.7: Vertically stacked LIF line profiles of H-atom and OH radical as a function of Φ; (c) and (f) 2-D sheet imaging of OH as a function of Φ 93

Figure 6.1: Spectrum of 193-nm fs pulses with FWHM = 0.4 nm reprinted from [136] 97

Figure 6.2: Spectra showing tunability at the FHG scheme with average power shown corresponding to each FHG wavelength reprinted from [137] 98

Figure 6.3: Schematic of direct THG and FHG setup 99

Figure 6.4: Digital image of the FHG setup (a) non-working condition (b) working condition 100

Figure 6.5: Complete wavelength tuning range of the direct frequency tuning apparatus 102

Figure 6.6: Schematic of the experimental apparatus 103

Figure 6.7: Spectrum of the (a) fundamental beam and (b) THG beam 105

Figure 6.8: (a) Regular (b) Normalized OH-PLIF spectra recorded using 1200 lines/mm grating for different equivalence ratios 106

Figure 6.9: (a) Regular (b) Normalized OH-PLIF spectra recorded using 2400 lines/mm grating for different equivalence ratios.....107

Figure 6.10: Comparison of OH-PLIF spectra obtained using THG with the simulated spectra obtained using LIFBASE and the spectra obtained using 283-nm generated from OPA.....109

Figure 6.11: Laser sheet beam profile 110

Figure 6.12: Variation of OH number density as a function of Φ in H_2/air flame.....111

Figure 6.13: Consequent single-laser-shot OH-PLIF images at 1kHz repetition rate demonstrating the flame development and dynamic flame structure in the CH_4/H_2 diffusion flame 112

Figure 6.14: Schematic of the energy level diagram of C-atom reprinted from [139]...115

Figure 6.15: (a) Excitation (b) Emission spectra in C-atom recorded for different transitions reprinted from [139] 116

Figure 6.16: Energy level diagram of O-atom depicting various VUV 2p excitation schemes reprinted from [145].....118

Figure 6.17: Schematic of the energy level diagram of O-atom reprinted from [8] 118

LIST OF TABLES

Page

Table 2.1: Summary of atomic transition selection rules for LS Coupling [7].....8

Table 2.2: Selection rules for molecular electronic transition [7].....9

1. INTRODUCTION

1.1 Motivation and Challenges

Over the past several decades, hydrocarbon-based compounds have served as the major fuel sources in various energy sectors including transportation and aviation industries and have been accepted as the most reliable fuels for internal combustion engines, aviation gas turbines and industrial burners. Therefore, it becomes important to understand the combustion chemistry in these systems to resolve the issues associated with the fuel economy, emissions and hardware design in order to optimize the efficiency of these practical combustion systems.

The combustion of hydrocarbons involves thousands of intermediate reactions and the production of numerous intermediate radical species such as H, O and N along with molecular intermediates such as CO, NO and OH. The quantitative measurement of these intermediates depends on the type of fuel burnt, combustion environment and the location (inside the flame) where we want to measure these species. Further, the lifetime of these intermediate species is very short in dynamic combustion environments and therefore, it becomes challenging to measure these species quantitatively using the conventional methods of measurement used in heat transfer and fluid dynamics.

Over the recent years, with the significant improvement in the quality of lasers, laser diagnostics have proved to be one of the best non-invasive methods to detect such short-lived species accurately. In laser diagnostic methods, all the measurements are recorded in probe volume (typically of the order of few millimeters) and the flow around

that probe volume remains unchanged. Thus, accurate measurements can be performed. However, even with the use of modern laser diagnostics, the accurate measurement of intermediate radical species is still challenging due to interferences from different species resulting in a low S/N ratio.

The intermediate radicals play a pivotal role in the combustion chemistry and chemical kinetics of hydrocarbon combustion reactions. Experimental measurements are important to understand the flame chemistry (ignition/extinction process) and to validate different chemical kinetics models that are being used for developing new combustion and propulsion systems, as well as in remote sensing, fundamental plasma science and in biomedical applications. Computational models have to be verified by the experimental data so that the endorsed models can be used for various applications and will eliminate the need for expensive experimentation. Therefore, extensive research is being conducted for qualitative and quantitative measurement of key intermediate species such as H, O, N, OH [1-5] however, detailed information about their fundamental chemistry is largely unknown due to the lack of accurate measurements because of the limited optical access in realistic harsh combustion environments. Therefore, the flames are generally replicated on a small scale over the calibration burners and the measurements are performed on those flames. However, even the measurements on a small scale are challenging because the species concentrations are very low and there are large uncertainties associated with their temporal resolution.

1.2 Laser-Based Imaging Diagnostics

In the recent decade, with the development and advancement in the quality of lasers, laser-based diagnostics have been implemented in numerous applications ranging from medical, defense, weather forecasting, microscopy etc. Indeed, due to its non-invasive nature, laser-based optical imaging spectroscopy has been widely used to study combustion processes. Further, laser absorption, laser-induced fluorescence, Rayleigh and Raman scattering, particle image velocimetry and four-wave mixing spectroscopy are some of the common laser diagnostic techniques that are being implemented to understand harsh environments such as reaction zones in internal combustion engines, gas turbines, propellant combustion etc. The main advantage of using laser diagnostics over the traditionally used probing devices is that the former is remote and always non-perturbing. Lasers can be used to get a single point, a line, 2-D as well as 3-D measurements at ultrafast speeds without disturbing the flame or changing the basic nature of the flow fields. In combustion, the aforementioned laser techniques can be used to quantitatively measure the minor species concentration (such as H, O, N, C, OH and NO), temperature and to get 3-D velocity distributions with negligible uncertainty as compared to the traditional probing systems. However, some of the disadvantages associated with implementing lasers are the limited optical access to the test volume. Further, no single laser technique is proficient enough to detect all the species and temperature, often two or more techniques have to be combined when working with practical systems, thereby resulting in higher uncertainties. Lastly, very high implementation and maintenance cost (as compared to the

traditional techniques) often limits their applicability to a wide range of practical applications.

1.3 Ultra-short Femtosecond Pulse Based Imaging in Combustion

In the recent decade, fs pulse-based laser systems are being extensively used by researchers worldwide for investigating complex combustion environments because of their advantages over the traditionally used ns or ps pulse-based lasers [6]. Further, it has been realized that LIF is the most promising and hence, widely used diagnostic method for species and temperature measurement in flames and plasma systems because of its high detection sensitivity and easy implementation for 2-D imaging of species such as OH radicals via planar LIF (PLIF). However, high pulse energy of ns and ps pulses, results in serious interferences from photolytic dissociation and production of the probed species. For example, the photo-dissociation of hydroxyl radical, water and methyl radical results in the formation of H-atom and thereby, resulting in its overestimation. However, this issue can be resolved using fs pulses, being high in peak power but low average energy which makes them ideal for multi-photon excitation of species such as H-atom and O-atom. Further, the fs pulses have proved to be very effective for reducing and potentially eliminating the quenching losses (resulting in lower excited state population) that were observed with traditionally used ns pulsed lasers. Moreover, the broad bandwidth of fs pulses contribute to efficient excitation and high-repetition rates (kHz) makes them ideal for multi-dimensional imaging of species.

1.4 Dissertation Outline

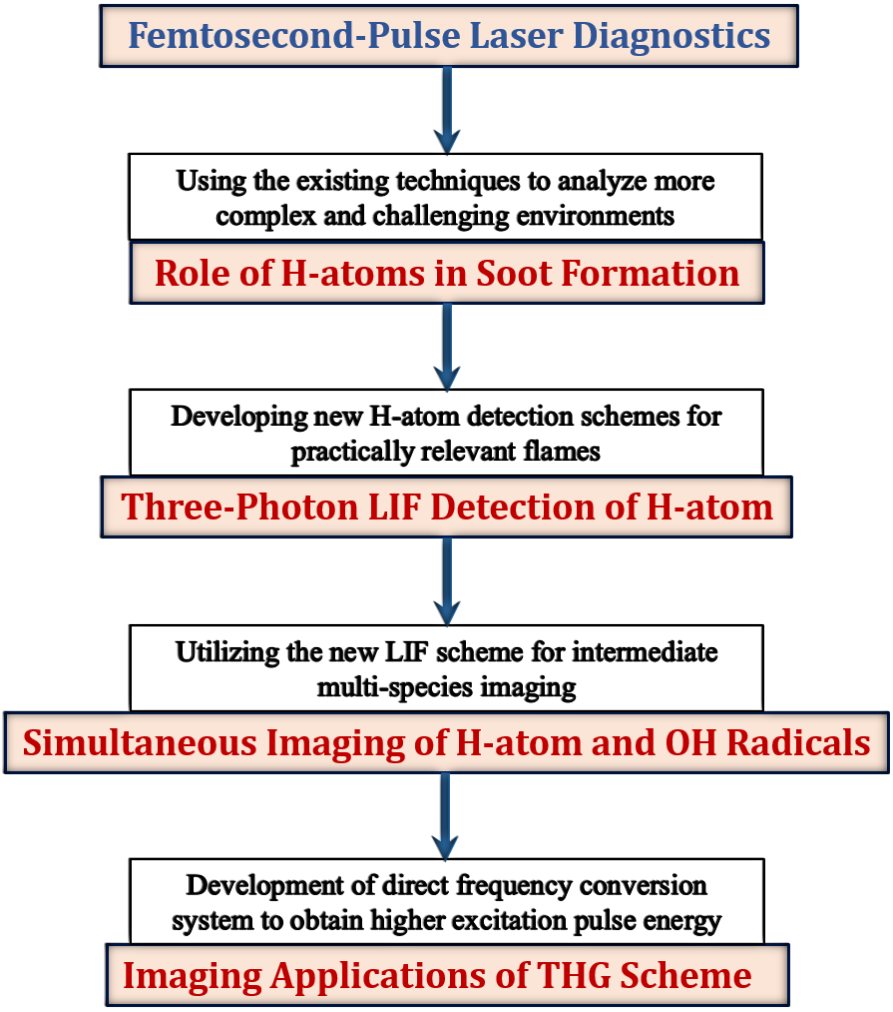

Figure 1.1: Dissertation Outline.

The flow chart shown in Figure 1.1 represents the dissertation outline. It gives an overall view of the chronological order of the thesis and highlights the sequential developments taking place in each chapter.

The objective of the present research is to demonstrate the use of ultrashort (fs) pulsed laser system for the detection of atomic hydrogen (H-atom) and hydroxyl radical

(OH) in different laboratory flames using LIF. H-atom and OH are two key intermediate species in the combustion of hydrocarbon fuels. H-atom is an important reaction intermediate governing the chemical kinetics of combustion reactions and plasma systems. Spatial and temporal distribution of H-atom is useful to better understand the ignition/extinction processes, and soot formation pathways, whereas OH distribution profiles can yield flame structure and reaction zone in different flames conditions.

An extensive literature review of the theory of laser-induced fluorescence, laser induced incandescence and recent developments in high-speed laser diagnostics instrumentation has been presented in Section 2. Further, the existing techniques of H-atom and OH detection were employed in harsh and complex environments to analyze the effect of H-atom concentration on soot formation, described in detail in Section 3. However, the UV wavelengths used for H-atom detection posed limitations (in terms of absorption and photolytic interferences) in practical combustion systems. Thus, we developed a new scheme (by red-shifting the excitation wavelength) for simultaneous H-atom and OH detection for diagnosis in more advanced optical combustion systems. This new 3-photon excitation scheme has been described in detail in Section 4 and Section5. It should be noted that all the frequency conversion explained in the previous sections had been performed via commercially available OPAs. As a result of the low conversion efficiency of OPA, the output UV beam generated from OPA does not have enough pulse energy for the excitation of minor intermediate species. Therefore, as an alternative to OPA, more efficient direct frequency conversion schemes using nonlinear BBO crystals have been discussed in Section 6. The high energy pulses (λ = 283-nm) generated using

this scheme were used to detect OH to study the flame structure and reaction zone in turbulent liquid spray flames using high-speed imaging optics. Lastly, Section 7 consists of the conclusion of the current work and recommendation for the future research needed to implement the LIF in practical combustion systems such as an internal combustion engine, gas turbines, supersonic and hypersonic flow field.

2. LITERATURE REVIEW

2.1 Selection Rules

Electron transitions in either an atom or a molecule do not occur between all the possible states. However, they occur only between certain states and are driven by a set of quantum-mechanically driven selection rules.

2.1.1 Selection Rules for Atomic Spectroscopy

Table 2.1: Summary of atomic transition selection rules for LS Coupling [7].

Principal quantum number, n	Δn – no restriction
Total orbital angular momentum, L	$\Delta L = 0, \pm 1$
Electron orbital angular momentum, l	$\Delta l = \pm 1$
Total angular momentum, J	$\Delta J = 0, \pm 1$ $J = 0 \nleftrightarrow J = 0$
Total spin, S	$\Delta S = 0$
Total angular momentum projection along magnetic field, M	$\Delta M = 0, \pm 1$ $M = 0 \nleftrightarrow M = 0$, when $\Delta J = 0$

The selection rules for atomic transitions have been summarized in Table 2.1 [7]. There is no restriction on the change in principal quantum number, thus, Δn can be 0, 1, 2 etc. Further, the total orbital angular momentum must satisfy, $\Delta L = 0, \pm 1$. However, in the case of single-electron systems or when the interaction between the electrons is very weak, the electronic orbital angular momentum, $\Delta l = 0, \pm 1$ must be satisfied. The constraint on the total spin quantum number for lighter atoms is $\Delta S = 0$; however, there can be some exceptions to this rule in case of heavier atoms. The total angular momentum must satisfy

$\Delta J = 0, \pm 1$ with the exception that the transition between two states with J = 0 cannot happen.

2.1.2 Selection Rules for Molecular Spectroscopy

Table 2.2: Selection rules for molecular electronic transitions [7].

Total Angular Momentum: Zero nuclear spin Nonzero nuclear spin	 $\Delta J = 0, \pm 1$; $J = 0 \nleftrightarrow J = 0$ $\Delta F = 0, \pm 1$; $J = 0 \nleftrightarrow J = 0$
Electronic Quantum Numbers: Hund's case (a) Hund's case (b)	$\Delta\Lambda = 0, \pm 1$ $\Delta S = 0$ $\Delta\Sigma = 0; \Delta\Omega = 0, \pm 1$ $\Delta N = 0, \pm 1$
Parity	Must change
Homonuclear molecules: Symmetry state	 No change $g \nleftrightarrow u$
Σ states:	even $\nleftrightarrow$ odd

The selection rules for molecular electronic transitions have been summarized in Table 2.2. The total angular momentum J must follow, $\Delta J = 0, \pm 1$, with the exception of forbidden transition between two states with J = 0. Further, there has to be a change in parity during the transition i.e. only ($+ \leftrightarrow -$) is allowed. Moreover, the even states must combine only with odd states in case of homonuclear molecules i.e. only $(g \leftrightarrow u)$ is allowed.

For electronic quantum number, the selection rule $\Delta\Lambda = 0, \pm 1$ and $\Delta S = 0$ must be satisfied. For molecular electronic transitions, the total electronic angular momentum must

satisfy $\Delta\Omega = 0, \pm 1$. Lastly, there is no restriction on the change of vibrational quantum number i.e. Δv can be 0, 1, 2 etc., however, within a given electronic state, transitions with $\Delta v = \pm 1$, are the strongest.

2.2 Laser-Induced Fluorescence

Laser-Induced Fluorescence (LIF) spectroscopy is a technique of detecting atomic (H, O, N, C and S) and molecular (OH, CH, NH, CO etc.) species residing in relatively lower concentrations in combustion flames. In LIF, a particular atom or molecule is excited to a higher energy level by absorbing the laser light tuned to a specific excitation wavelength. For a particular species, the excitation wavelength is chosen where the atom/molecule has maximum absorption cross-section. Generally, the lifetime of the species in the excited state is of the order of a few picoseconds or nanoseconds. Thus, the spontaneous decay of the excited species results in the emission of light (fluorescence), typically at a wavelength red-shifted with respect to the excitation wavelength. The fluorescence is then detected by devices such as PMTs, filtered photodiodes or ICCD cameras.

Figure 2.1 shows the schematic of two types of LIF process; fluorescence spectrum (left) where, the laser is tuned to a specific excitation wavelength and the fluorescence is recorded at various emission wavelengths and excitation spectrum (right) where a broadband fluorescence spectrum is recorded for a series of absorption transitions. LIF is experimentally less complicated as compared to other, Raman-based and wave-mixing techniques, which require multiple laser beams for excitation. Moreover, the S/N ratio in LIF is much higher than Raman scattering; thus, LIF has high detection sensitivity for

species concentration below 100 ppm. Further, the fluorescence takes place in all directions and is isotropic in nature, therefore, it can be used for capturing 2D and 3D flow fields in combustion and plasma applications.

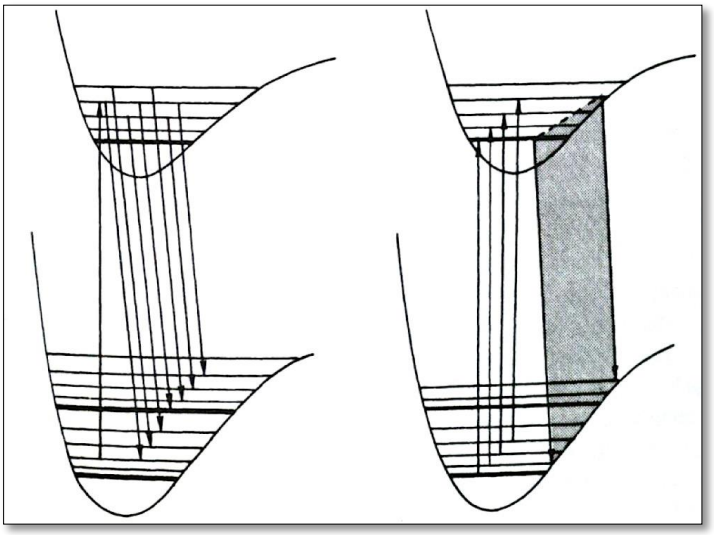

(a) **(b)**

Figure 2.1: Laser-Induced Fluorescence scheme shown in (a) Fluorescence emission lines resulting in an emission spectrum (b) Fluorescence excitation resulting in an excitation spectrum reprinted from [7].

However, when an atom/molecule is excited, several processes can take place simultaneously along with LIF. The species in the excited state may dissociate before spontaneously decaying to the lower state. This process is called pre-dissociation. Further, if nanosecond pulsed lasers are used for the excitation, the large pulse energies of the nanosecond pulses result in the compound breakdown by photolytic dissociation. This process may result in the undesired production of species being probed, which leads to uncertainties in quantitative measurement since the total number density of the radical

(being detected) is now more than that was naturally present in the flame. Further, radiation due to collisions in the excited state results in the loss of excited state population. This process of quenching increases the decay rate and results in uncertainties in quantitative measurements.

2.2.1 Single-photon LIF Detection

Figure 2.2 shows a 2-level energy diagram depicting the excitation mechanism using a single photon. It has been assumed here that the fluorescence (spontaneous emission) will occur at a single wavelength when the electron descends from level 2 to level 1.

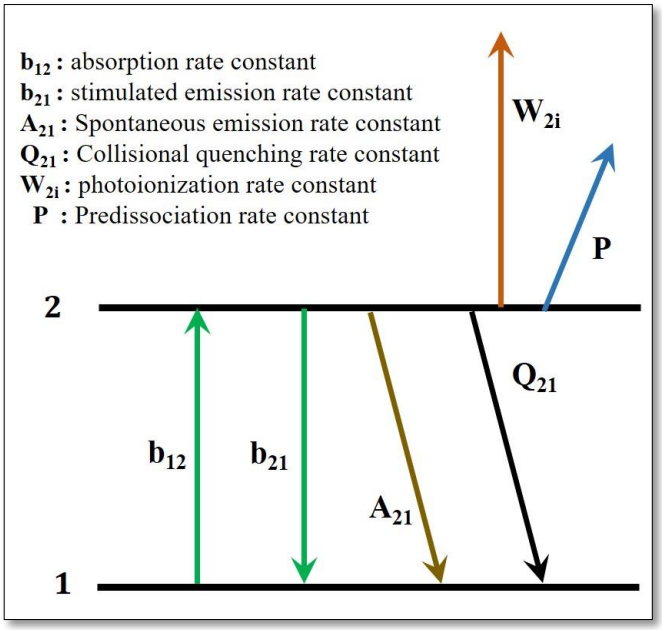

Figure 2.2: Energy level diagram showing different process that occurs along with LIF.

Assuming that we are operating in the linear regime, fluorescence signal power is given by:

$$F = \frac{h\upsilon}{c}\frac{\Omega}{4\pi} lAN_1 B_{12} I_\upsilon \frac{A_{21}}{A_{21}+Q_{21}} \qquad (1)$$

Where,

F = fluorescence signal power

h = Planck's constant

ν = frequency of emitted florescence

N_1 = ground state population

Ω = collection solid angle

A = focal area of the laser beam

l = axial extent along the beam from which florescence is observed

I_ν = incident laser irradiance per unit frequency interval

A_{21} = spontaneous emission rate constant

B_{12} = absorption rate constant

Q_{21} = collisional quenching rate constant

2.2.2 Multi-Photon LIF Detection of Atomic Species

Most of the atomic/molecular transitions from the ground state to the excited state require very high pulse energies resulting in shorter excitation wavelengths. Single-photon absorption wavelengths for various atoms fall in the vacuum UV (VUV) range of the electromagnetic spectrum typically < 200 nm as shown in Figure 2.3 [8].

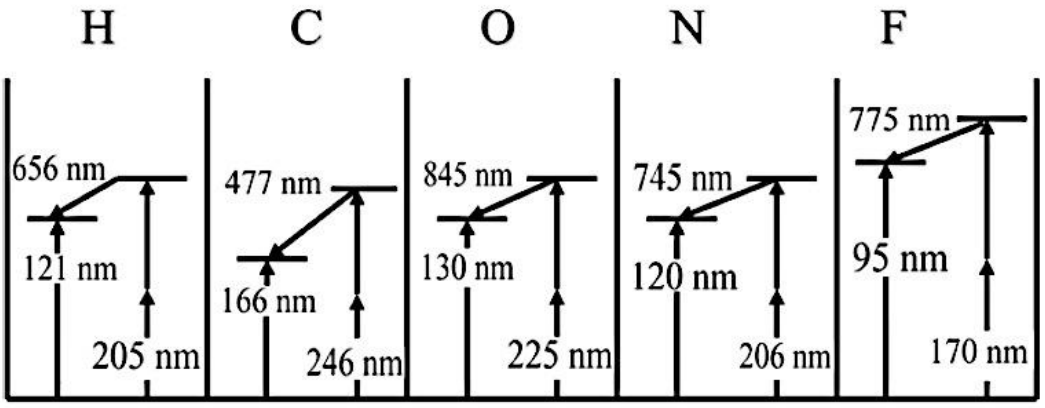

Figure 2.3: Multi-photon excitation schemes shown for different atoms reprinted from [8].

However, it is difficult to use VUV wavelengths for experimentation purposes due to atmospheric absorption by oxygen and ozone. Therefore, such transitions are achieved by simultaneous absorption of multiple photons which red-shifts the excitation wavelength. Few examples of 2p excitation LIF are shown in Figure 2.3. Further, since the absorption cross-sections decrease with an increase in number of photons required for excitation, the signal strength in case of multi-photon excitation will be significantly lower as compared to single-photon excited LIF. For 2p excited LIF, 2p excitation rate per molecule is given by;

$$W_{12} = \frac{\alpha_{12} I^2}{\hbar\omega} \qquad (2)$$

where,

α_{12} = 2p absorption cross-section from state 1 to state 2

Further, $N_1 b_{12}$ in Equation (1) will be replaced by $N_1 W_{12}$.

In general, for multi-photon excitation, when there is no saturation, the LIF signal is given by:

$$Sig_{LIF} \propto I^n$$

$$log_{10}(Sig_{LIF}) = c + nlog_{10}(I)$$

Where,

I = laser intensity

n = number of photons involved in the transition from the ground electronic state to the excited electronic state

c = constant

2.2.3 Prior Work on H-atom Detection

Over the past several decades, laser-based detection of H-atom has been of considerable interest amongst the researchers. The study of H-atom provides an understanding of the fundamental flame structure which can significantly alter the efficiency of various combustion systems.

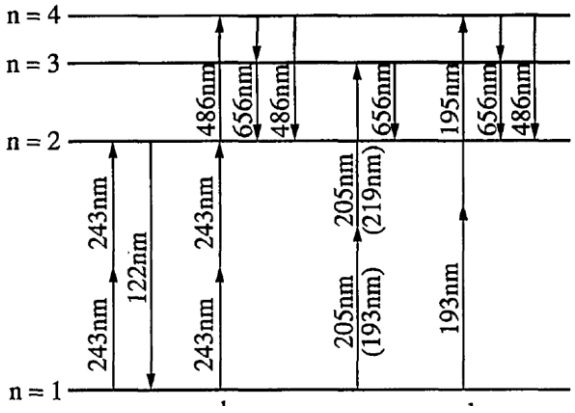

Figure 2.4: Multi-photon excitation schemes in H-atom reprinted from [9].

Figure 2.4 shows the energy level diagram depicting different excitation schemes in H-atom. It is quite evident that if single photon is used to excite the electron from n=1 → n= 3 or n= 4, the excitation λ (< 103-nm) will fall in the VUV region of the electromagnetic spectrum. It is very difficult to work with VUV wavelengths in practical combustion systems since such λ gets absorbed by oxygen present in the air. Therefore, multi-photon absorption laser-induced fluorescence (LIF) has been considered as a relatively simple and reliable technique to detect H in combustion flames and plasma devices. The technique of two-photon LIF (2pLIF) (as shown in Figure 2.4) has been extensively explored by the researchers worldwide [10-13]. The implementation of 2pLIF for detecting H was first demonstrated by Lucht et al. [10] in 1983. An excitation wavelength (λ = 205.1-nm) was used for n=3 level excitation and the fluorescence signal was collected at 656-nm radiative decay from n=3 → n= 2 electronic state; however, quantitative measurements could not be done because the population in the excited state is significantly reduced because of quenching. In order to overcome the quenching issues, a technique of photoionization controlled loss spectroscopy (PICLS) was implemented to remove the signal dependence on quenching.

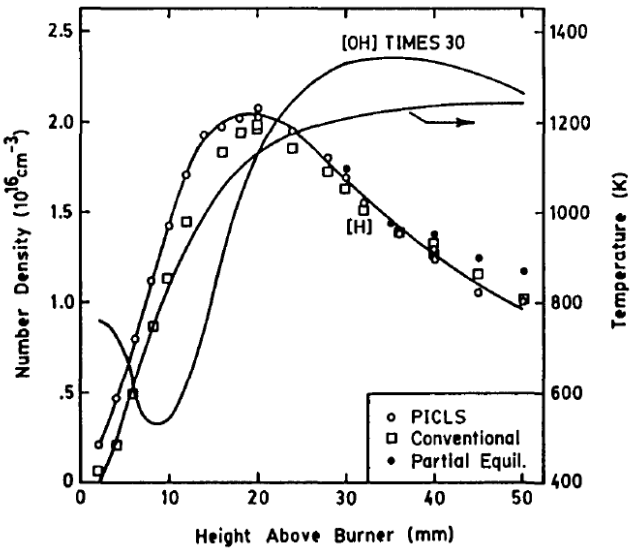

Figure 2.5: H-atom number density as a function of HAB obtained for PICLS and LIF at Φ = 1.0 in H_2/ O_2/ N_2 flame at a pressure of 20 Torr reprinted from [14].

Figure 2.5 shows the comparison of H-atom number density obtained using PICLS and conventional LIF. It was observed that conventional LIF measurements agreed with the PICLS in the post-flame region, implying a negligible quenching rate. However, in the preheat region near the surface of the burner, PICLS measurements reported higher number densities compared to conventional fluorescence measurements. This is because of the dominant effect of quenching in the preheat zone. Thus, PICLS proved to be an effective tool for minimizing the signal loss due to quenching. However, because of high ionization, the fluorescence signal obtained in PICLS has significantly lower S/N ratio. Further, to enhance the S/N ratio two-step saturated LIF detection of H-atom was demonstrated by Goldsmith [12]. Moreover, absolute atomic densities using LIF have been determined for various atomic intermediates using 2pLIF [8].

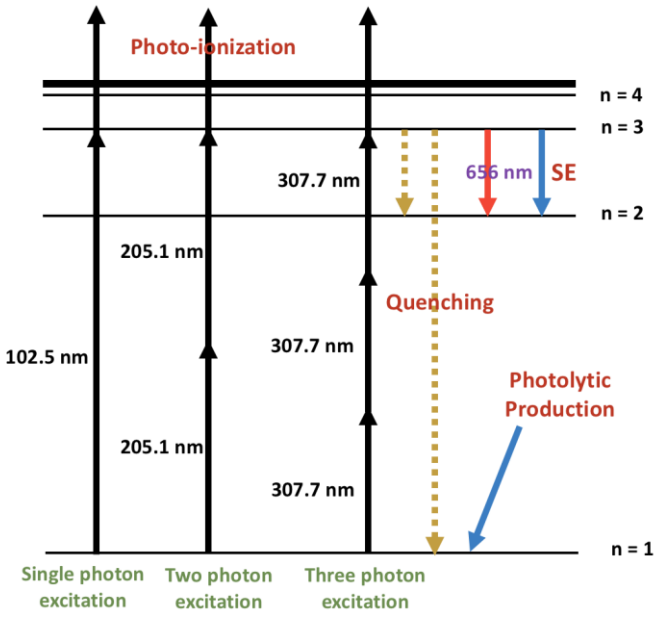

Figure 2.6: Simultaneous complicating processes in LIF detection.

Figure 2.6 shows different processes that occur simultaneously and interfere with LIF quantitative measurements. These include photolytic production of intermediate species in the ground state, photoionization, stimulated emission, electronic and collisional quenching. Photolytic production generally occurs as a result of molecular breakdown due to high energy laser pulses. For example, while detecting H-atom in flames, photolysis of water molecules (due to high energy ns pulses) results in the production of H-atom and OH, thus leading to the over-estimation of H than what is naturally present in the flame [13]. Further, to reduce the effect of quenching and for absolute H-atom concentration measurement, experiments were performed in low pressure (sub-atmospheric) flames [14-18]. It was realized that better spatial resolution (within the reaction zone) was obtained at lower pressures because of reduced flame speed and slower reaction rates.

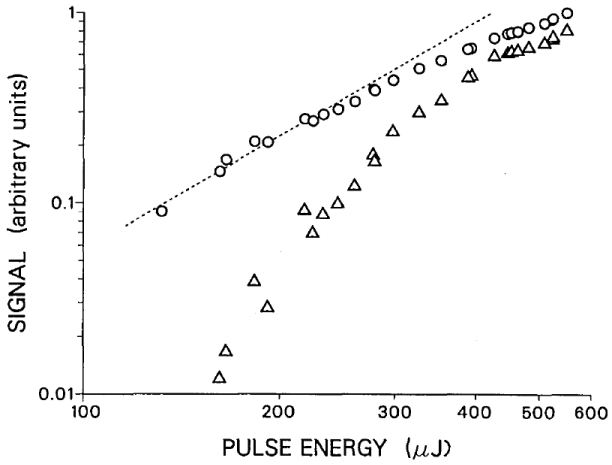

Figure 2.7: Intensity dependence of SE (triangles) and LIF (circles) at Φ = 0.6 at 72-torr in H_2/O_2/Ar flame reprinted from [11].

Figure 2.7 shows stimulated emission in 2pLIF H-atom detection was observed by Goldsmith [11] using ns pulses and by Ding et al. [19] (Figure 2.8) using resonant fs-2pLIF excitation. SE has a highly nonlinear dependence on laser pulse energy. Higher SE increases the rate of loss of the excited state population which results in lower fluorescence yield. Therefore, it is necessary to eliminate the effect of different simultaneous processes (discussed above) to make precise quantitative measurements. Further, Czarnetzki et al. [9] have compared different 2pLIF excitation schemes amidst polarization schemes and excitation wavelengths. They concluded that 2pLIF excitation scheme ($n=1 \rightarrow\rightarrow n=3$) using λ = 205-nm and fluorescence detection at Balmer-α gives maximum signal intensity for a given pulse energy. Further, λ = 205-nm excitation wavelength with linear polarization results in minimum photolytic dissociation of molecules by laser radiation.

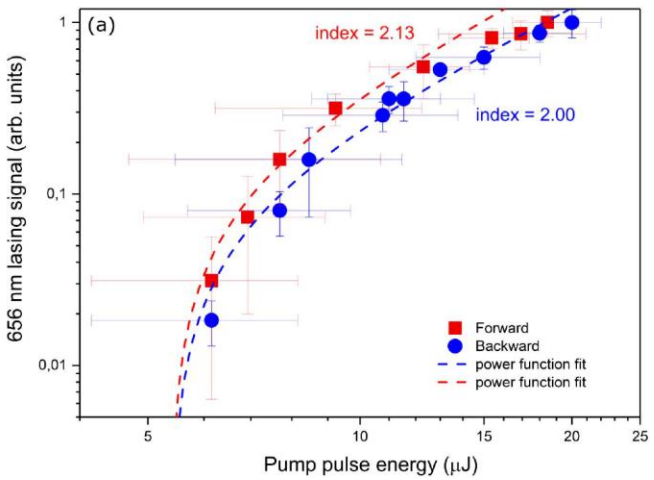

Figure 2.8: Forward and backward lasing SE in CH_4/air flame reprinted from [19].

In 2001, Niemi et al. demonstrated a technique to obtain the absolute atomic densities of H-atom, N-atom and O-atom using 2pLIF. The LIF in these atomic species were investigated together with two noble gases, namely, Krypton (Kr) and Xenon (Xe), since they have same excitation resonant wavelengths. Figure 2.9 demonstrates the excitation schemes for Kr, H-atom and N-atom. The former noble gas was used to determine the calibration factor which can be used to measure the quenching coefficients and cross-sections, excited-state lifetimes and collisional dependencies for H-atom and N-atom and the latter was used for O-atom. Winters et al. [20] also reported absolute concentrations of H-atom and OH radical number densities in ns pulse discharge plasmas at the liquid-vapor interface using 2p absorption LIF.

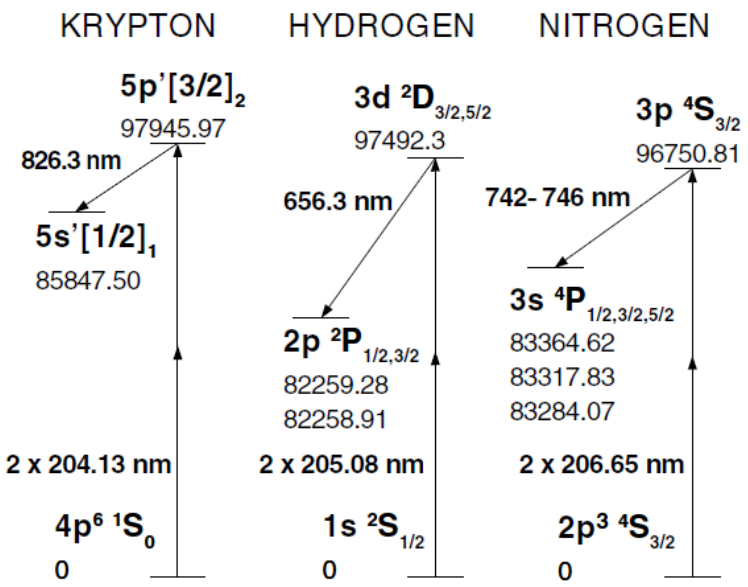

Figure 2.9: 2p excitation schemes of Kr, H-atom and N-atom reprinted from [21].

However, it was realized that obtaining quantitative H-atom number density by implementing 2pLIF using ns laser pulses is very challenging because the detection technique is very sensitive to collisional quenching in an excited state. In order to resolve this issue, researchers tried to implement few other detection techniques to detect H-atom, namely, 2p resonant four-wave-mixing (FWM) spectroscopy [3], two-color laser-induced grating spectroscopy [22] and two-color, 2p laser-induced polarization spectroscopy [23]. It was observed that all these techniques were insensitive to collisional quenching in the excited state and hence, gave a better estimation of atomic number density of H-atom. However, these detection schemes were limited by their complex experimental setup as compared to LIF.

So far, all the work discussed was conducted using ns laser pulses and the researchers have realized the drawbacks of ns-excitation in terms of various interferences.

Extensive research on 2pLIF using nanosecond, and picosecond pulses has been done by Kulatilaka et al. [24-26]. A comparative study of nanosecond and picosecond pulses revealed that photolytic interferences were lower for picosecond pulses (due to lower average pulse energy), however, the latter was limited by higher SE emission. Figure 2.10 shows the comparison of normalized H-atom distribution profiles detected using ns and ps laser pulses depicting the effect of photolytic production of H-atom in $CH_4/O_2/N_2$ flames. For different pulse energies, a reasonable H-atom distribution profile overlap was observed in the case of ps-excitation, implying a significant reduction in photolytically produced H-atom as compared to ns-excitation scheme.

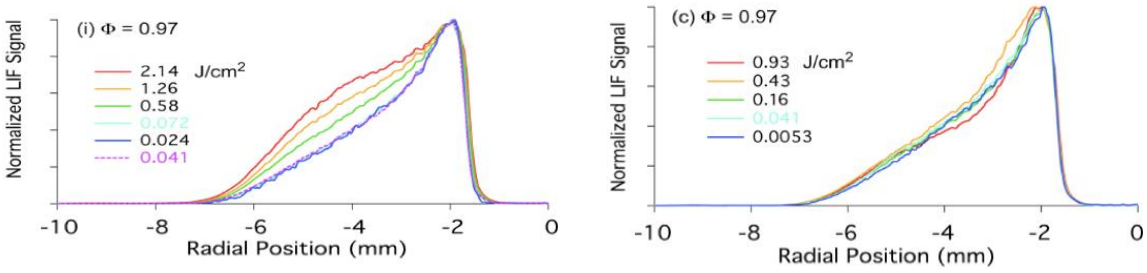

Figure 2.10: Comparison of nanosecond (left) and picosecond (right) pulses for H detection in $CH_4/O_2/N_2$ jet flame reprinted from [26].

However, the slight deviation in profile overlap in the case of ps-excitation indicated that even picosecond pulses produce some interferences leading to uncertainties in fluorescence signal detection. This motivated the researchers to implement femtosecond laser pulses to eliminate the observed interferences. The major advantage of using ultrashort femtosecond pulse is the high intensity and lower average energy compared to picosecond pulses.

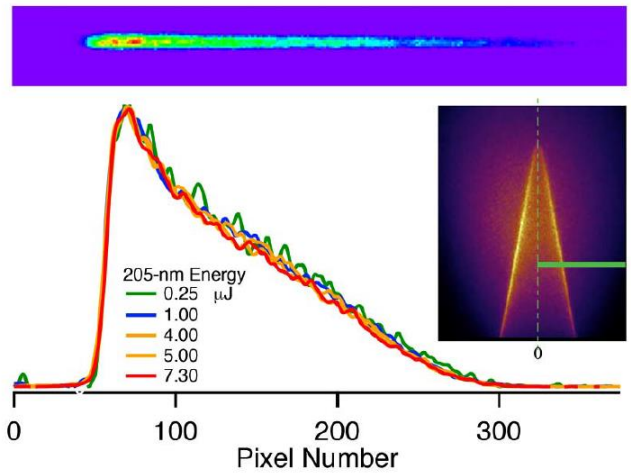

Figure 2.11: Peak-normalized H distribution profiles in $CH_4/O_2/N_2$ flame using femtosecond laser pulses different pulse energies reprinted from [27].

The quantitative H-atom number density in premixed hydrogen tubular flames have been reported by Hall et al. [28] using sub-picosecond laser pulses. The results indicated nearly 40% offset in peak number densities compared to simulations [29], however, the numbers reported were impressive considering high uncertainties in detector spatial response and over low number density of the atomic species. Recently, Mulla et al. [30] have demonstrated the implementation of LIF of CH_2O and H-atom to estimate heat release rate in Bunsen jet premixed flames.

Figure 2.11 shows the 2pLIF H-atom distribution profiles in jet flame using femtosecond laser pulses at an excitation wavelength of 205-nm (generated using commercially available OPA). The advantage of using fs pulses is clearly evident by an excellent profile overlap for different pulse energies as compared to Figure 2.10. It was realized that 2-D imaging of H-atom was not possible because of low energy of 205-nm pulses as a result of the low conversion efficiency of the OPA (~ 0.3%). Therefore, direct

frequency quadrupling (conversion efficiency >1%) was used to generate 205-nm femtosecond laser pulses to be used for planar (2D) LIF imaging of H-atom as shown in Figure 2.12.

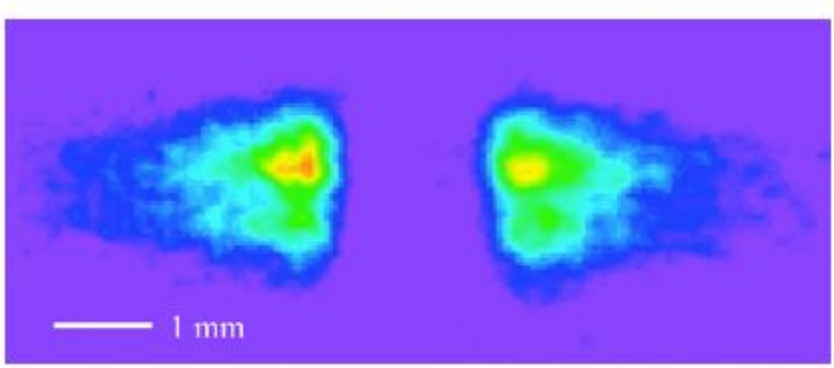

Figure 2.12: 2-D single laser shot image of H-atom in premixed Bunsen jet flame obtained using direct frequency quadrupling reprinted from [31].

Recently, fs-2pLIF has been demonstrated by Schmidt et al. [32] for imaging of atomic hydrogen and oxygen in sub-atmospheric non-equilibrium plasmas. In summary, the technique of 2pLIF has been extensively investigated by researchers, however, the combustion chemistry of H-atom in different flame reactions is still largely unknown. Moreover, the DUV excitation wavelength (used for 2pLIF) cannot be used while working with thick transmission optics (example optical windows in pressure vessels or I.C. engines). Therefore, red-shifting the excitation wavelength, such as in 3pLIF (more details in Chapter-4), would be advantageous while operating in such harsh practical environments.

2.2.4 Prior Work on OH Radical Detection

Hydroxyl radical (OH) number density can be measured using different laser diagnostic techniques such as laser-induced fluorescence (LIF), wave-mixing techniques and laser saturated fluorescence. However, LIF is the most straight forward and experimentally convenient method for detecting species concentration below 100 ppm. It is experimentally convenient because a typical experimental setup for LIF requires only one laser beam (wavelength) to get the desired signal. For over decades, nanosecond pulsed lasers have been used for the detection of OH in flames [33-40], however, large pulse energies of the nanosecond pulses result in the compound breakdown by photolytic dissociation and thus generating undesired radical species. Further, it can lead to uncertainties in OH measurement because sometimes high energy nanosecond pulse tends to dissociate water (a combustion product) and generate OH radicals. Therefore, the total number density of the OH radicals is now more than that was naturally present in the flame. Moreover, since the pulse duration of the nanosecond pulse is longer compared to the lifetime of the intermediate species of interest, we would not be able to capture the actual dynamics of the combustion as it keeps on changing with time. Further, we mostly deal with the real combustion environments which are highly turbulent in nature and the repetition rates of the nanosecond pulsed lasers are on the order of 10-50 Hz, which is not sufficient to capture the combustion events in the turbulent flame.

The schematic of the OH energy level diagram is shown in Figure 2.13. The excitation data has been taken from [34, 41-44]. Four different excitation schemes have been shown in the schematic of Figure 2.13. ‘A’ and ‘X’ represent the electronic levels

and three vibrational levels (v = 0,1,2) have been shown corresponding to each electronic level. Rotational states corresponding to the vibrational levels have not been depicted. The blue arrows depict the excitation wavelength and the red arrows depict the fluorescence emission wavelength. The two main excitation schemes shown are two-photon fluorescence (TPF) [45] using an excitation wavelength of 612 nm and single-photon fluorescence (SPF) using excitation wavelengths of 306 nm and 281 nm. The notation TPF (v', v") and SPF (v', v") show the excitation from the upper electronic state vibrational levels (v') to the lower electronic state vibrational levels (v"). A relative comparison among TPF, SPF and LSF [46-48] (laser saturated fluorescence) on the basis of excitation and detection band and spectral and temporal detection has been summarized in Figure 2.14.

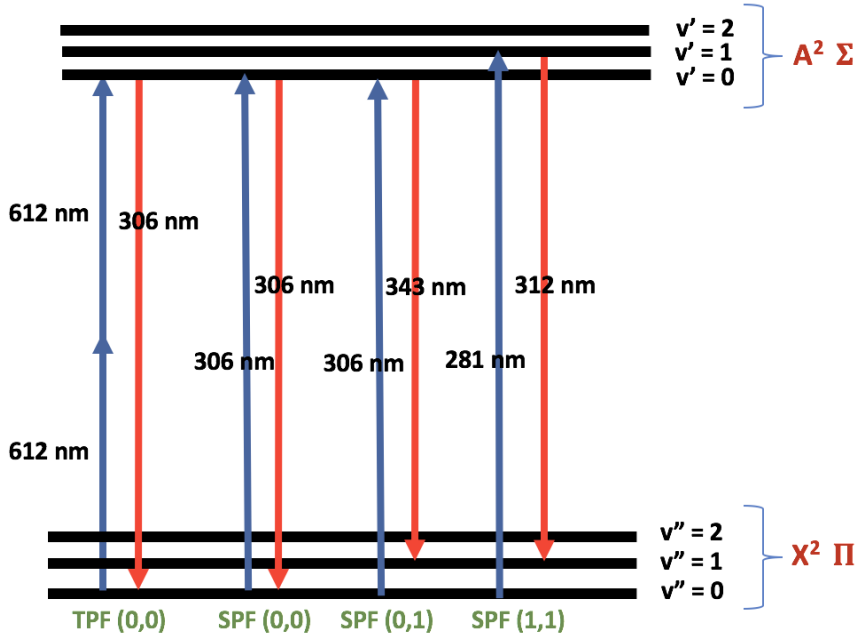

Figure 2.13: Schematic of different excitation schemes in OH radical.

Method	Excitation (v', v'') $A_{v'v''}/A_{0,0}$[a] Bandhead (nm)[a]	Detection (v', v'') $A_{v'v''}/A_{0,0}$[a] Bandhead (nm)[a]	Spectral Detection	Temporal Detection
SPF(0,0)	(0,0) 1.000 306 nm	(0,0) 1.000 306 nm	Broadband (306–320 nm)	Broadband (~ 10 ns)
SPF(0,1)	(0,0) 1.000 306 nm	(0,1) 0.004 343 nm	Broadband (343–357 nm)	Broadband (~ 10 ns)
SPF(1,1)	(1,0) 0.37 281 nm	(1,1) 0.60 312 nm	Broadband (312–326 nm)	Broadband (~ 10 ns)
TPF	(0,0) – 612 nm	(0,0) 1.000 306 nm	Broadband (306–320 nm)	Broadband (~ 10 ns)
LSF	(0,0) 1.000 306 nm	(0,0) 1.000 306 nm	Narrowband (~ 312 nm)	Narrowband (~ 1 ns)

Figure 2.14: Excitation and detection parameters for OH fluorescence measurement reprinted from [34].

The authors observed that SPF (0,1) profile has the highest peak due to negligible self-absorption of the radiation. SPF (1,1) profile values were lower due electron transfer to v' = 1 to v' = 0 due to collisional quenching. However, the researchers mentioned that under ideal conditions SPF (1,1) profiles have to be higher than SPF (0,1) and SPF (0,0) due to less absorption of the laser beam in the former case and less self-absorption compared to the latter. Moreover, TPF profiles were in excellent agreement with the SPF (0,0) profiles.

Further, planar LIF (PLIF) of OH has been explored in detail by the researchers worldwide to investigate the reaction zones (marked by OH) in different reacting and non-reacting flow fields [1, 2, 33, 35, 36, 49, 50]. Allen et al. [33] recorded the instantaneous OH spatial distribution in the heptane air spray flame. OH number density was found to

be negligible in the central part of the spray which represents the unignited vaporized cold liquid fuel where the stoichiometric ratio is inappropriate (below flammability limits) for ignition. It should be noted that detection of OH spatial profile helps in determining the reaction zones inside the flame. Further, it was observed that, other than the central reaction zone, there is an envelope of gases entrained on the outer periphery of the inner reaction zone. The reactions in this region take place when the vaporized fuel comes in contact with the surrounding atmospheric air which serves as an oxidizer for combustion. Further, the effect of increasing the flow rate of atomizing air on OH distribution profiles was investigated. It was realized that the area of the reaction zone got significantly reduced when the airflow rates were increases.

Further, Yip et al. [35] showed some results obtained by simultaneous imaging of acetone and OH PLIF in acetone seeded methane low-speed jet flames. The excitation wavelength used for both acetone and OH was 308 nm generated using XeCl excimer laser. Two separate ICCD cameras were used to detect acetone and OH simultaneously. It was observed that the acetone LIF lies in the visible spectrum (380 nm - 540 nm) and was present mostly in the central part of the flame whereas the long streaks on the periphery of the flame represent the OH detected in the flame reaction zone. However, there some blurred jet images in between the two OH streaks arise as a result of Rayleigh scattering from the methane-acetone fuel. The overlap of OH-PLIF and acetone PLIF represented the complete reaction zone. There was an empty region between the acetone jet images and OH reaction zone which occurred as a result of acetone pyrolysis.

Another demonstration of OH-PLIF detection in spray jet flame produced using liquid methanol was reported by Cessou et al. [36]. The excitation schemes followed was (0,1) and the fluorescence was detected for SPF (0,0) and SPF (1,1) so that the spectrum can be distinguished from methanol droplet elastic scattering. Along with the OH fluorescence signal, the authors observed some bright white spots in the flame fronts as a result of Raman scattering from bigger methanol droplets. The researchers concluded that the double flame structures observed for air and oxygen atomization could be a result of premixed flame surrounded by a diffusion flame. The diffusion flame burns the excess fuel with the external air. This belief was seconded by the fact that only single diffusion flame-lets were observed when the spray was atomized using N_2 gas.

OH has also been investigated using PLIF in high-pressure spray flames [51] at pressures ranging from 1 – 10 bar. In high-pressure liquid spray flames, researchers observed a non-resonant fluorescence interference (from hydrocarbon fuel fragments in fuel-rich areas of the flame) that increased with an increase in pressure. Further, OH-PLIF in laminar premixed CH_4/air flames for pressures varying from 5 – 36 bars has been reported by Atakan et al. [52]. The authors reported the advantages of using A-X (1,0) transition near 281-nm over the more commonly used (0,0) and (3,0) transition excitation. Moreover, for quantitative measurements of species number density or heat release rate, the dependence of rotational quantum number on pressure broadening coefficient and quenching corrections must be taken into account to correct for the temperatures. Recently, OH detection using PLIF in high-pressure cryogenic Lox/GH_2 jet flames has been reported by Singla et al. [53]. Recently Jain et al. [54] investigated the flow flame

interactions using simultaneous OH and PAH PLIF imaging in kerosene and kerosene surrogate spray flames.

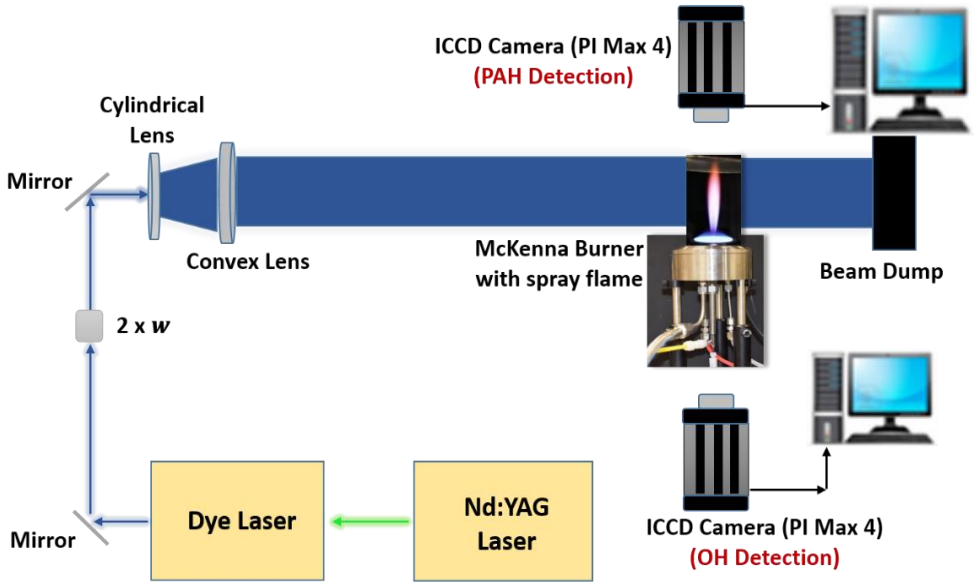

Figure 2.15: Schematic of the experimental apparatus for OH-PLIF and PAH-PLIF measurements in piloted spray flames reprinted from [54].

Figure 2.15 shows the schematic of the experimental apparatus used for the simultaneous detection of OH and PAH via PLIF. Single-photon rotational transitions of $Q_1(5)$ (282.750-nm) of the OH $A^2\Sigma^+$-$X^2\prod$ (1,0) band were used, and subsequent fluorescence from the OH $A^2\Sigma^+$-$X^2\prod$ (0,0) and (1,1) bands were detected. The same UV wavelength of 282.75-nm was used to excite smaller (2-4 rings) PAHs.

Figure 2.16 represents the simultaneously acquired single-laser-shot OH-PLIF and PAH-PLIF images for kerosene and surrogate liquid spray flame in range 20-60 mm above the burner, marked by region 1 (R1) and in the range 60-100 mm, marked by region 2 (R2). It can be seen in Figure 2.18 that PAHs mainly exist in the central region of the flame surrounded by flame fronts marked by OH. Further, based on these instantaneous

images, fine wrinkling effects along the flame fronts can be observed as a result of turbulent mixing of the fuel droplets with the surrounding air.

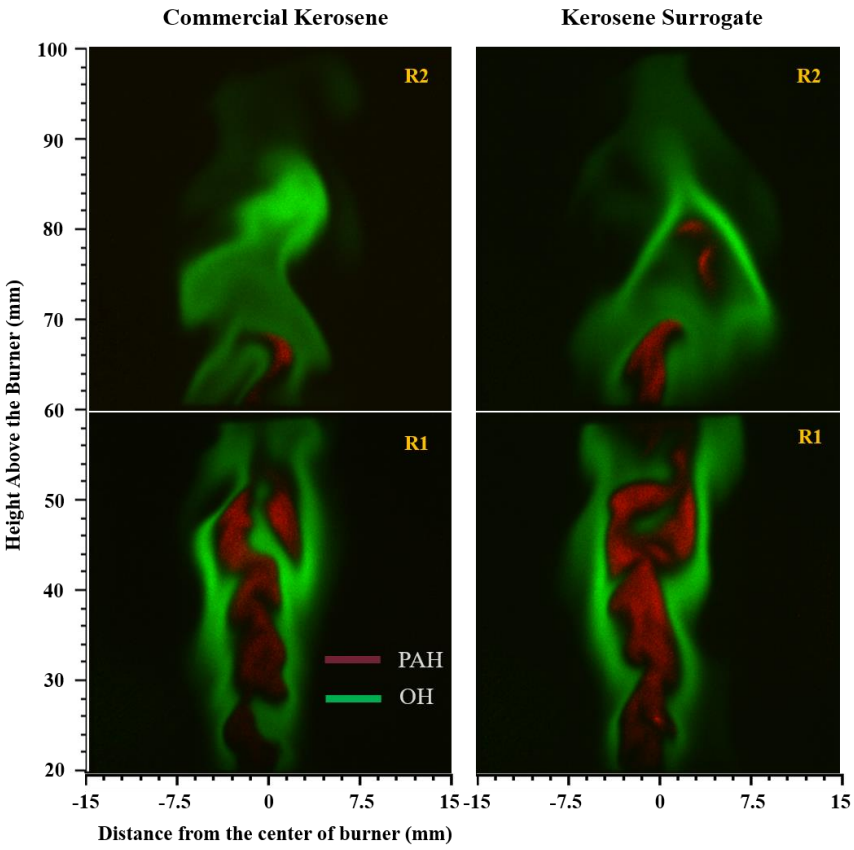

Figure 2.16: Simultaneous single-laser-shot PLIF images of PAH and OH in R1 and R2 for commercial kerosene and its surrogate reprinted from [54].

In addition, flame quenching and reignition events can be observed in Figure 2.16. The liquid droplets coming out of the nebulizer, evaporate and expand along with the flame height and gets converted into smaller (2-4 rings) PAHs in R1. Further, since excitation wavelength depends strictly on the size of the PAHs and UV wavelengths can only excite smaller PAHs, the concentration of PAHs decreased as the two flame fronts

merged downstream along the flame height in R2. It is also known that higher temperature effects in R1 convert smaller PAHs into larger PAHs (present mostly in R2). These larger PAHs could not be detected by UV wavelength (282.75-nm) and are responsible for broader fluorescence emission when excited by visible wavelengths. Further downstream in R2, these large PAHs coagulate and lead to the formation of nascent soot particles responsible for the luminosity.

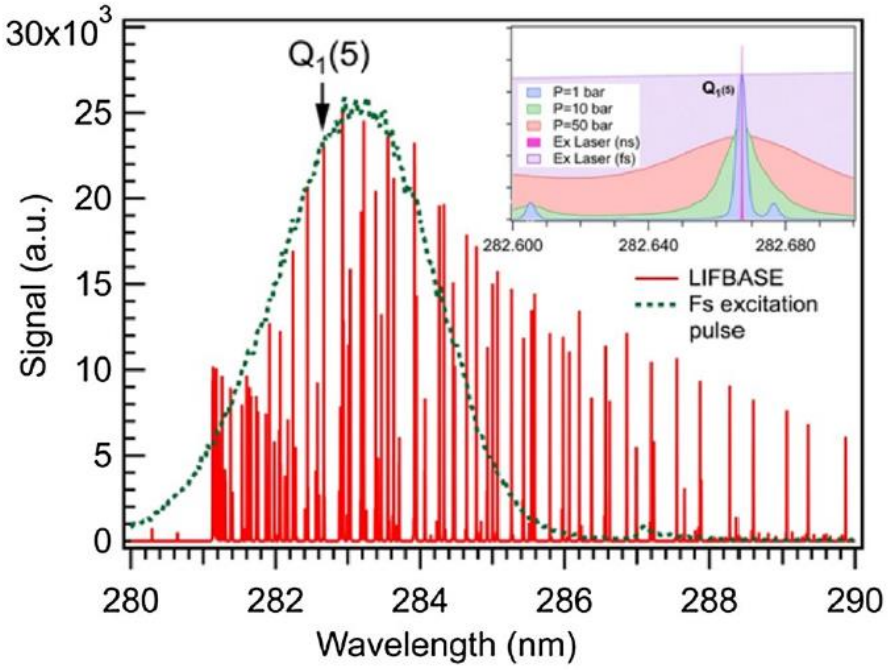

Figure 2.17: Broadband spectrum of the fs laser pulse (dotted line), the calculated OH-LIF excitation spectrum obtained at 2200 K and 1 atm using the LIFBASE software package reprinted from [55].

Further, quantitative concentration measurements of OH radicals in the CH_4/air diffusion flame has been reported by Smyth et al. [56]. The authors reported the maximum absolute concentration to be $1.8 \pm 0.2 \times 10^{16}$ cm^{-3} at 2080 K. Moreover, they mentioned that this concentration is nearly double of that calculated assuming total equilibrium and

half of that predicted from partial equilibrium. Two-color OH PLIF has also been used for temporally resolved 2-D temperature measurement in reacting flows [57]. Further, high repetition rate PLIF of OH using ns laser pulses has been used for understanding the flame dynamics and temperatures in flow fields turbulent flames [58, 59]. Kulatilaka et al. [60-63] have extensively explored the utilization of fiber-coupled high repetition rate ns laser pulses for point and planar OH PLIF. The major advantage of utilizing the all-fiber-coupled optics is the easement of taking the laser diagnostics tool from research laboratory to the practical flow fields of interest. Thus, it was realized that, even though the utilization of traditional ns laser pulses for the detection of OH via PLIF proved to be a major leap, the low repetition rate of ns pulses (typically 10-50 Hz) limits their ability to completely capture complex reactive flow fields of turbulent nature. In the past few years, the development of ultrashort femtosecond laser pulses has been quite significant.

These ultrafast laser systems operate at very high repetition rate of 1 kHz-10 kHz, which makes it very convenient to capture high-speed flow dynamics in harsh combustion environments. Further, femtosecond pulses have low average power and high intensity, thereby, eliminating the photolytic interferences as was seen in case of nanosecond pulses. Over the past few years Kulatilaka et al. [55, 64-67] have utilized ultrafast (fs) laser pulses for detecting OH in various harsh environments. Figure 2.17 shows a typical 80-fs duration pulse that was used for the excitation of the multiple OH lines. It should be noted that because of the broadband nature of fs pulses, the pulse need not be exactly centered on the excitation line, unlike in the case of ns pulses.

2.3 Soot Imaging via Laser-Induced Incandescence

Soot formation occurs as a result of incomplete hydrocarbon combustion and can cause serious environmental and health hazards. Extensive research has been done on soot formation pathways but the mechanism has not been fully understood because of the lack of accurate, spatially resolved experimental data of reactive intermediates such as H, which play a critical role in soot formation pathways [68-74].

Since, Eckbreth [75] first observed the incandescence from heated soot particles, laser-induced incandescence (LII) has been established as a major diagnostic tool for measuring soot and determining its properties [68, 69, 76-91]. In LII, soot particles are heated to a temperature below its vaporizing point using a laser pulse and the continuous black body incandescence spectrum of soot is observed in the visible spectral range.

Figure 2.18 [68] shows the normalized LII signal obtained by heating the soot particles at an excitation wavelength of 1064-nm. The figure shows the distribution of the LII signal in the visible region of the spectrum along with the black-body emission curves shown at different temperatures. It was observed that the soot temperature in this wavelength range varied between 5000-6000 K. Quay et al. [68] obtained spatially resolved f_V and soot particle size in laminar diffusion flames using LII and Vander Wal et al. [69] observed that the LII signal was directly proportional to f_V. In previous studies, quantitative measurements for particle size and f_V had been demonstrated using light scattering and extinction measurements [69, 76, 92-94]. Vander Wal et al. [69, 95] performed 1-D and 2-D LII imaging in rich C_2H_4/air flames stabilized using disc setup and a chimney setup over a McKenna burner. They reported that major interferences to be

avoided while observing the incandescence signal in the visible spectral range were mainly from PAHs, C_2, OH and O-atom emissions. Goulay et al. [96] observed the dependence of the LII signal on the laser fluence. They suggested that for fluence values greater than 0.2 J/cm^2, the detection range between 380-680 nm should be avoided because of the interference from C_2, and C_3 emissions.

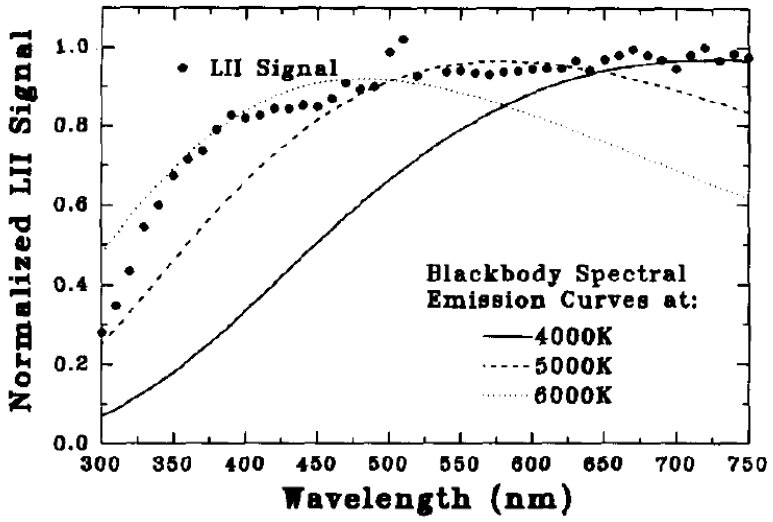

Figure 2.18: Spectral response of the normalized LII signal at an excitation wavelength of 1064-nm reprinted from [68].

In a recent review article by Michelsen [97] and Schulz [98], different soot diagnostic techniques have been discussed in terms of their advantages for measuring soot properties. Figure 2.19 [97] shows the schematic of the soot formation mechanism. It can be seen that intermediate combustion radicals such as H, O, OH and N. play a critical role in the formation of small aromatic hydrocarbons such as phenyls and benzene. These aromatic compounds result in the formation of larger hydrocarbon radicals like PAHs which acts as soot precursors. In general, soot formation comprises of the four major sequential processes, [99] namely, the formation of soot particle precursors, coagulation

of particles, particle growth, and particle agglomeration. Different studies have reported soot particle precursors as ionic species [100], polyacetylenes [101], and polycyclic aromatic hydrocarbons (PAHs) [102]. However, PAHs are widely accepted to be the major precursors as suggested by numerous modeling and experimental studies [72, 73]. Further, it has been observed that H-atoms play a critical role in the formation of small aromatic rings from straight-chain aliphatic hydrocarbons.

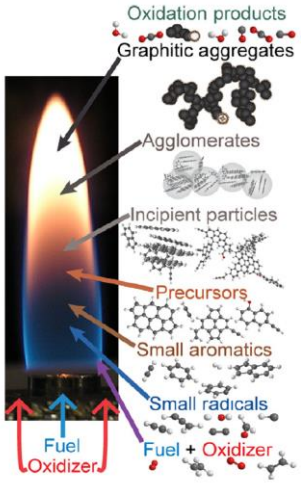

Figure 2.19: Schematic of soot formation in flame reprinted from [97].

Lemaire et al. [103-105] implemented LII to obtain soot volume fraction in liquid pilot spray flames for different fuels (diesel, gasoline and kerosene) and their surrogates. The fuel surrogates were used to replicate the complex commercially available hydrocarbon fuels (which usually contains hundreds of compounds with varying compositions) with respect to the flashpoint, sooting tendency, heat release rate and other physiochemical properties. For example, typical kerosene Jet A-1 is a mixture of alkanes (50-65% vol), polyaromatics (10-20% vol) and cycloalkanes or naphtenes. Figure 2.20 shows the 2-D distribution of soot and soot precursors (mainly PAHs) in diesel and surrogate liquid spray flames.

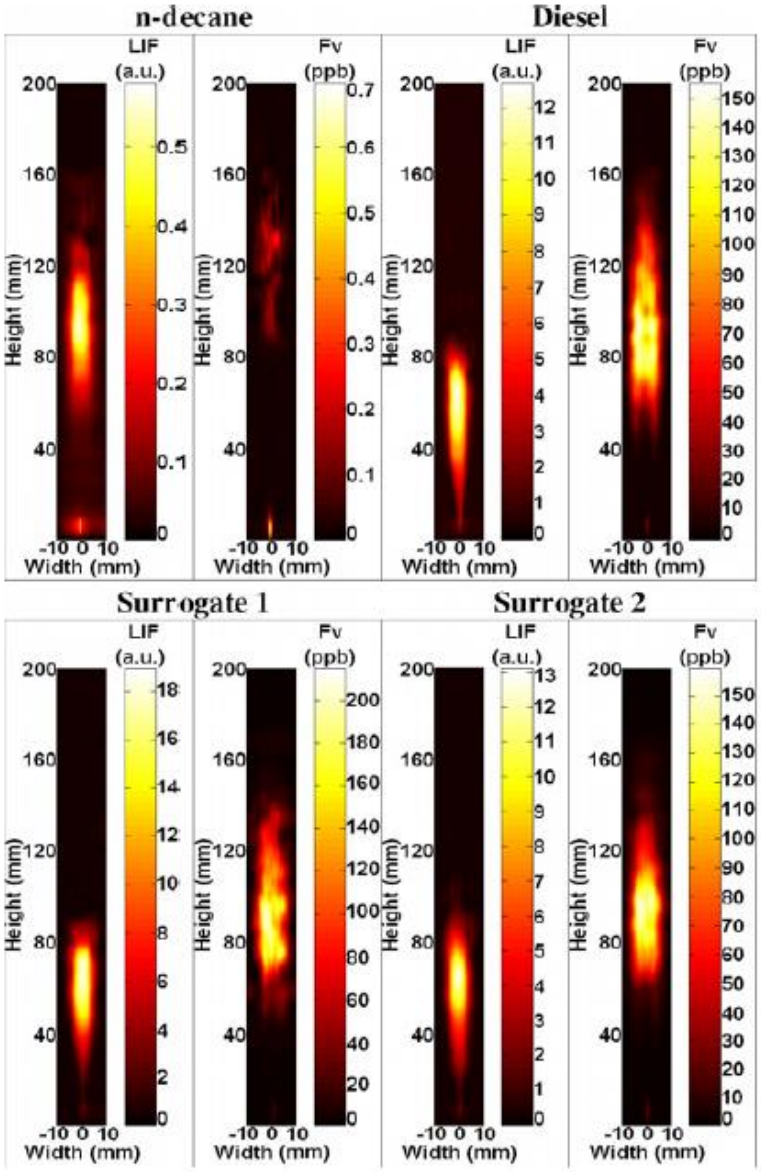

Figure 2.20: 2-D images of LIF and soot volume fraction (Fv) in diesel and surrogate liquid spray flames reprinted from [103].

Further, various numerical studies regarding modeling of PAHs in sooting flames have been reported [106-108]. Moreover, the effect of morphology and soot particle size distribution on LII has been investigated in detail [79, 109, 110]. Also, Mouton et al. [111]

were able to separate the two major isomers contributing to the formation of PAHs, namely pyrene and fluoranthene, using jet-cooled LIF.

Recently, several successful attempts for the simultaneous measurement of soot volume fraction, PAHs and OH distribution using UV, visible and IR wavelengths have been demonstrated [112-115].

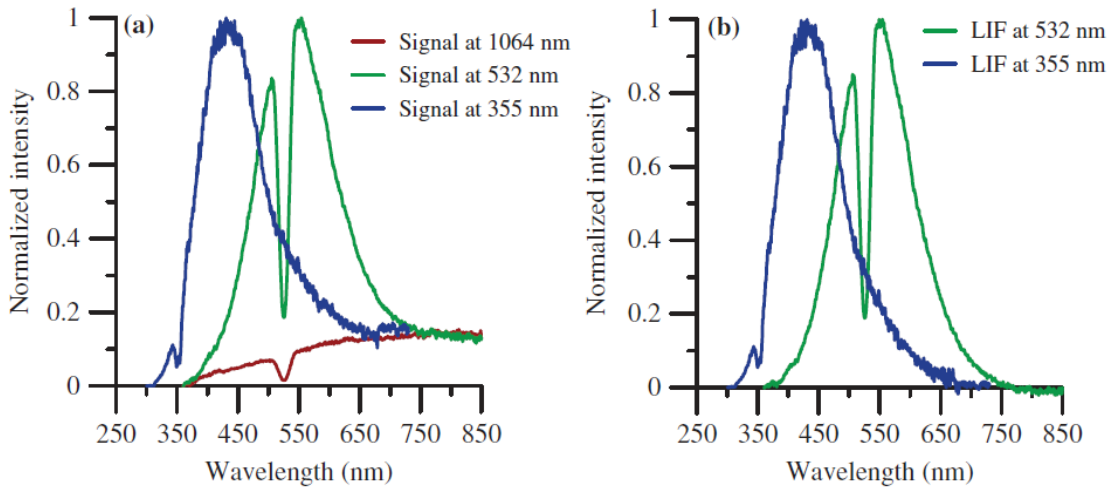

Figure 2.21: (a) LIE (LII + LIF) spectra at 3 different excitation wavelengths. (b) LIF emission spectra at 355 and 532-nm reprinted from [113].

Over the recent decade, it has been well understood that only IR wavelengths can generate pure LII signals. As shown in Figure 2.21, the total emission (LIE) at UV or visible excitation wavelengths is a combination of LIF (from PAHs) and LII (from soot particles). Further, it was observed that red-shifting the wavelength red-shifts the LIE spectra. Also, larger PAHs are more likely to be excited by the longer excitation wavelengths and the highest excitation wavelength that can excite PAHs in flame conditions has been reported to be 680-nm.

2.3.1 Role of H-atoms in PAHs formation

Different pathways have been suggested for the formation of the first aromatic ring, primarily phenyl (C_6H_5) or benzene (C_6H_6). Common pathways for even C-atom compounds include [70]:

$$n - C_4H_3 + C_2H_2 \rightarrow phenyl \quad (1)$$

$$n - C_4H_5 + C_2H_2 \rightarrow benzene + H \quad (2)$$

Further, some odd carbon atom pathways via highly stable propargyl radical (C_3H_3) and several other radicals have been suggested [116]:

$$C_3H_3 + C_3H_3 \rightarrow benzene\ or\ phenyl + H \quad (3)$$

$$C_5H_5 + CH_3 \rightarrow benzene + H + H \quad (4)$$

$$C_5H_5 + C_5H_5 \rightarrow naphthalene + H + H \quad (5)$$

Once the soot precursors are formed, small aromatic rings combine together to form PAHs. An important observation has been the change in the [H] at the time of growth of PAHs [72]. Various chemical kinetic pathways have been suggested for PAH formation from smaller aromatics based on the common and frequently used principle of "H-Abstraction-C_2H_2-Addition" (HACA) [70]. The model of HACA mechanism for PAH growth can be expressed as [71]:

$$A_i + H \rightleftharpoons A_{i-} + H_2 \quad (6)$$

$$A_{i-} + C_2H_2 \rightleftharpoons A_iC_2H_2 \quad (7)$$

$$A_iC_2H_2 + C_2H_2 \rightarrow A_{i+1} + H \quad (8)$$

In reaction (6), gaseous H atoms react with aromatic compound A_i via collision, resulting in the formation of A_{i-} radical and hydrogen gas [117]. It is important to note

here that both these steps (reactions 6 &7) are reversible. Thus, the formation of PAHs depends on the irreversibility of the final reaction (reaction 8) [71].

From the above discussion it is quite evident that the H-atoms play a critical role in the formation of PAHs and soot. Spatially resolved H-atom concentration measurements are invaluable for an in-depth understanding of soot formation, thereby improving the current soot models. In our study, we investigated the dependence of soot formation on H in laboratory sooting flames (Φ = 0.8-3.0). We have followed the work of Vander Wal et al. [69] to determine f_V using LII in C_2H_4/Air flames and have implemented fs-2pLIF to detect H in sooting flames.

2.4 High-Speed Laser Diagnostics Instrumentation

2.4.1 Fundamentals of Femtosecond Laser Systems

It should be noted that most of the prior discussion on LIF, CWMT has been performed using ns pulsed laser systems and therefore, the results were limited by the various interferences including photolytic production of species and lower SNR. Moreover, since the pulse duration of the nanosecond pulse is longer compared to the lifetime of the intermediate species of interest, it is very challenging to determine the actual collisional dynamics of gas-phase molecules. Further, in real combustion environments which are highly turbulent in nature and the repetition rates of the nanosecond pulsed lasers (on the order of 10-50 Hz) is not sufficient to capture the combustion events in the turbulent flame.

In the past few years, the development of ultrashort femtosecond laser pulses has been quite significant. These ultrafast laser systems operate at very high repetition rate of

1 kHz-10 kHz, which makes it very convenient to capture high-speed flow dynamics in harsh combustion environments. An extensive comparison of the ns and fs pulses amid different grounds for 2pLIF has been done recently by Schmidt et al [118]. The significantly shorter duration of femtosecond pulses compared to the excited state decay times results in accurately resolving the signal without any interference from the laser pulse as was seen in case of ns pulses. Further, fs lasers have only a solid-state medium and the system is mode-locked (responsible for ultrashort pulse generation) as opposed to the dye-based system in ns lasers. Therefore, pulse energy fluctuations are lower in case of fs systems. Moreover, fs pulses have low average power and high intensity, thereby, eliminating the photolytic interferences as was seen in case of ns pulses and yields more accurate signal. Further, for 2-D imaging of species, the spatial homogeneity of fs-laser systems is superior and intensity fluctuations along the laser sheet are minimal. Also, the broad bandwidth of fs pulses results in more efficient excitation and thus, for fs pulses, the single-shot detection limit in approximately three times better than that of ns laser systems [118].

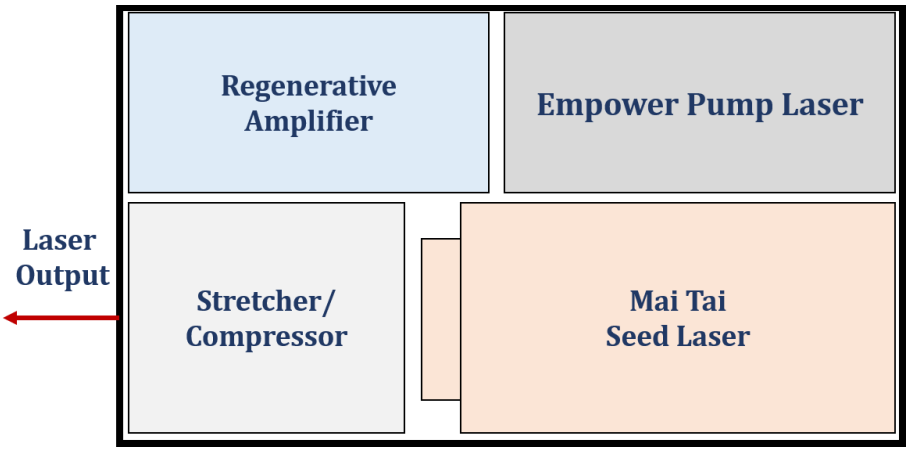

Figure 2.22: Schematic of the laser assembly.

Figure 2.22 represents the assembly of the Solstice laser amplifier system producing pulses less than 100-fs in duration operating at 1-kHz repetition rate. The output wavelength can be varied between 750-nm to 850-nm. The system comprises of 4 major components namely Mai Tai seed laser, Empower pump laser, regenerative amplifier and pulse stretcher/compressor system. The Mai Tai consists of two lasers, a CW diode-pumped laser (Nd: YVO_4 crystal) giving an output wavelength of 532-nm at 5W and a mode-locked Ti: Sapphire pulsed laser generating IR wavelengths tunable over a range from 750 – 850 nm operating at 80 MHz with pulse duration less than 100 fs. The 532-nm output of the CW laser is an ideal pump source for Ti: Sapphire laser. Further, Empower pump laser is a frequency-doubled Q-switched diode-pumped Nd:YLF laser producing pulsed, 527-nm green beam.

The output fs pulse train coming out of the Mai Tai head enters the stretcher section of the Solstice Ace system and gets stretched and thus, reduces in power. The train of stretched seed pulses leaves the stretcher and enters the regenerative amplifier. The pockels cell inside the amplifier selects one out of every 80000 stretched fs pulses and the selected pulse gets amplified when it passes through the Ti: Sapphire crystal (inside the regenerative amplifier). The Ti; Sapphire crystal is excited to a condition of population inversion by a high energy pulse coming from the Empower pump laser. The amplified pulse then re-enters the compressor region, gets compressed and comes out of the laser.

2.4.2 High-Speed Imaging Systems

A high-speed CMOS camera (Model: FASTCAM SA-Z; Photron) and a high-speed UV intensifier (Model: HS-IRO; LaVision) was used for ultrafast imaging in combustion and for flow visualization such as in PIV. A high-speed CMOS camera is coupled with the intensifier (attached at the back). HS-IRO can provide the frame rates up to 22kHz at full resolution to up to 600 kHz at lower resolution. Further, a high-speed camera can provide megapixel image resolution at the frame rate of 21 frames per second (fps) and low-resolution images when operating at 2 million fps. These high-speed imaging systems have proved to be ideal for capturing the high turbulent flow fields in harsh combustion environments. This system can be used to record the shot-to-shot variations while detecting the radicals in laboratory flames. In this study, this imaging system has been used to record consequent single-laser-shot OH-PLIF images at 1kHz repetition rate in CH_4/H_2 (1:1) diffusion turbulent flames. The details of the experiment have been discussed in Chapter-6.

3. ROLE OF ATOMIC HYDROGEN CONCENTRATION ON SOOT FORMATION*

Soot formation is a major challenge in the development of clean and efficient combustion systems based on hydrocarbon fuels. Fundamental understanding of the reaction mechanisms leading to soot formation can be obtained by investigating the role of key reactive species such as atomic hydrogen taking part in soot formation pathways. In this study, two-dimensional laser-induced incandescence (LII) measurements using λ = 1064-nm laser have been used to measure soot volume fraction (f_V) in a series of rich ethylene (C_2H_4)/air flames, stabilized over a McKenna burner fitted with a flame stabilizing metal disc. Moreover, a comparison of UV (λ = 283 nm), visible (λ = 532 nm) and IR (λ = 1064 nm) laser excited LII measurements of soot is discussed. Recently developed, femtosecond two-photon laser-induced fluorescence (fs-2pLIF) technique has been applied for obtaining spatially resolved H-atom concentration ([H]) profiles under the same flame conditions. The structure of the flames has also been determined using hydroxyl radical (OH) planar laser-induced fluorescence (PLIF) imaging. The results indicate an inverse dependence of f_V on [H] for a range of C_2H_4/air rich flames up to an equivalence ratio, Φ=3.0. Although an absolute relationship between [H] and f_V cannot be easily derived owing to the multiple steps involving H and other intermediate species in soot formation pathways.

---

* Part of this chapter is reprinted with permission from "Effect of H-atom concentration on soot formation in premixed ethylene/air flames" by A. Jain, Y. Wang, and W. D. Kulatilaka, Proceedings of the Combustion Institute 37 (2019) 1289-1296. Copyright [2018] by The Combustion Institute. Published by Elsevier Inc.

The present study demonstrates the feasibility to couple [H] and f_V obtained using advanced optical techniques for soot formation studies. Further, the background of H-atom detection via 2pLIF has been discussed in detail in Section 2.2.3. Moreover, soot detection via LII and the role of H-atoms in soot formation pathways have been thoroughly discussed in Section 2.3. The experimental specifications of the apparatus and the key observations have been discussed here.

3.1 Experimental Details and Procedure

Figure 3.1 (a) shows the schematic of the experimental apparatus used for LII measurements. Experiments were performed in premixed C_2H_4/air flames stabilized over a 60-mm diameter stainless-steel, water-cooled porous plug McKenna burner. This particular McKenna burner also consisted of a 7.4-mm diameter central feed tube, which was completely sealed from the bottom during the current experiments. The burner also has a 5-mm wide annular shroud ring. The flame equivalence ration (Φ) was varied from very lean (0.8) to very rich (3.0) conditions. The total gas flow rate was held constant at 10 slpm, while the C_2H_4 flow rate was varied between 0.24–1.50 slpm. Dry nitrogen gas was used as a shroud at a constant flow rate of 10 slpm.

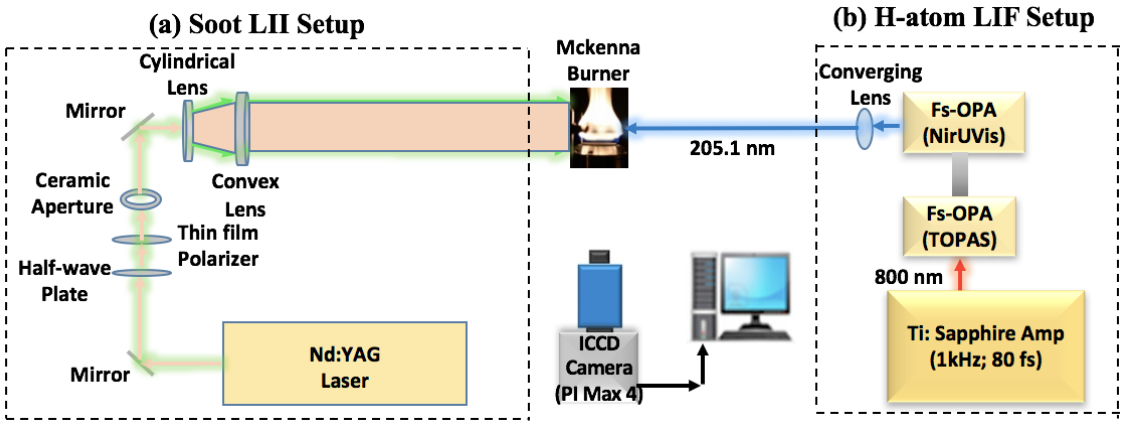

Figure 3.1: Schematic of (a) LII and (b) fs-TPLIF experimental systems for obtaining f_V and relative [H], respectively, in rich C_2H_4/air flames stabilized over a modified McKenna flat-flame burner reprinted from [119].

The flame was stabilized using a 60-mm-diameter, 20-mm-thick stainless-steel disc, mounted asymmetrically at the height of 20 mm above the burner surface. A similar flame stabilization setup has also been used previously for LII and Coherent Anti-Stokes Raman Spectroscopy (CARS) thermometry measurements [69, 77, 120, 121], however, the researchers used the standard flat flame Mckenna burner.

The output from a 10-Hz, Nd:YAG-pumped dye laser system was frequency doubled to generate approximately 4-ns-duration, tunable UV radiation near 283-nm for OH PLIF. The flame structure was observed by OH PLIF imaging by using an excitation laser sheet completely spanning the gap between the burner surface and the disc. Using UV radiation at 282.750 nm, multiple rotational transitions of the OH $A^2\Sigma^+$-$X^2\prod$ (1,0) system was excited, followed by (0,0) and (1,1) fluorescence imaging through a 315±15-nm bandpass filter. Fluorescence images were recorded using an intensified CCD (ICCD) camera fitted with a UV camera objective. The details of the OH PLIF apparatus are described in previous publications [27].

A 10-Hz, Nd:YAG laser system (Continuum, Powerlite DLS Series) was used to generate 1064 nm and 532-nm frequency-doubled, approximately 8-ns-duration laser pulses for LII experiments. The 9-mm diameter, near Gaussian laser beam was passed through a combination of a half-wave plate and a thin film polarizer to attenuate the beam energy as required. A 5-mm diameter ceramic aperture was inserted in the beam path to select the near-top-hat portion of the Gaussian beam for the experiment.

Full 2D LII images were recorded using an intensified CCD (ICCD) camera (Princeton Instruments Model: PIMax4) fitted with a narrow bandpass (485–500 nm) filter (Semrock Corp.) spanning the entire gap between the burner surface and the disc. The gate width used for capturing the LII data using 1064 nm and 532 nm excitation wavelength was 100 ns [77] and 200 ns respectively. In addition, a 400 ns gate delay with respect to the laser pulse was applied to eliminate the PAHs fluorescence during approximately first 50 ns [98]. A telescope arrangement consisting of an f=-50-mm cylindrical lens followed by an f=+400-mm spherical lens was used to generate a laser sheet of approximately 50-mm high and approximately 0.5 mm thick. The central portion of this sheet was passed through the burner-disc gap and full 2D LII images were recorded using the same ICCD camera setup. Further, the laser sheet intensity was recorded using a beam profiler (Ophir-Spiricon) for LII and OH-PLIF experiments and the data was corrected for the variations arising due to uncertainties in intensity along the height of the laser sheet. A continuous-wave, 632-nm He-Ne laser beam was used for f_V calibration by extinction measurements for each equivalence ratio at 15-mm HAB. Further, the calibration procedure was same for all three excitation wavelengths (283, 532 and 1064-nm). However, considering the

slight instability of the very rich flames (Φ = 2.9 and 3.0), final calibration was performed at Φ = 2.8.

For H-atom fs-2pLIF measurements, same burner system was used under the identical flow conditions. The 2pLIF apparatus shown in Figure 3.14 (b) consists of a 1-kHz-repetition-rate Ti:Sapphire laser system (Spectra Physics, Model: Solstice Ace), generating approximately 80-fs-duration laser pulses for pumping an optical parametric amplifier (OPA) system. The peak pulse energy of the pump laser at 800 nm is 6 mJ/pulse and parametric conversion of the pump beam followed by frequency mixing and subsequent up-conversion of the idler beam generates approximately 10 μJ/pulse of UV radiation near 205 nm. An f = +200 mm plano-convex lens was used to focus the 205-nm beam which is then transmitted through the probe volume. A similar ICCD camera system as described above was used to capture the Hα fluorescence line through 656±3nm bandpass filter (Andover Corporation). In all OH PLIF, LII and H-atom fs-2pLIF measurements, backgrounds were recorded separately while blocking the respective laser beams, and subtracted off from the subsequent signal images.

3.2 Results and Discussion

Figure 3.2 shows the series of images from C_2H_4/air flames (Φ=0.8–3.0), recorded using a digital SLR camera. A key observation from these images is that flames appear light bluish in color until the soot appears around Φ = 1.7. The bright region of the flame also tends to slightly lift off from the burner surface with increasing Φ. These qualitative observations are in good agreement with the subsequent quantitative data described below.

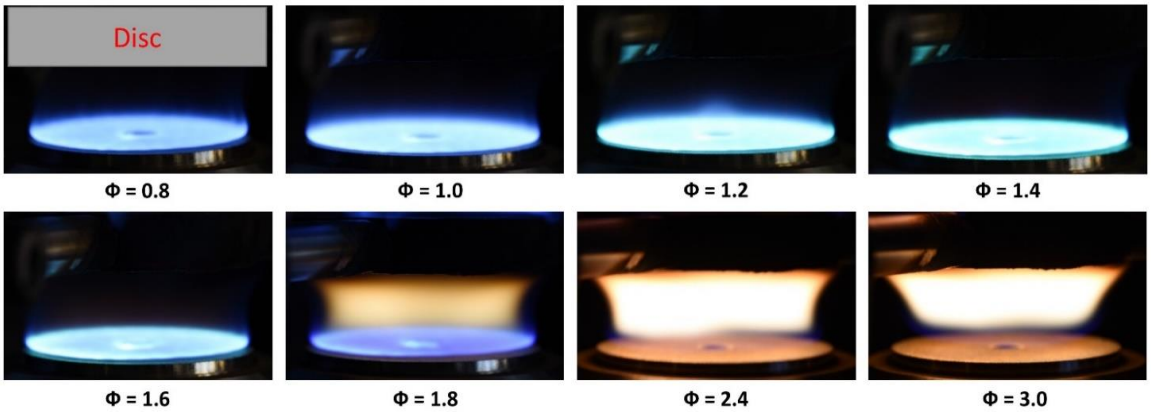

Figure 3.2: Digital images of series of flames over the McKenna burner with an axisymmetric disc mounted above reprinted from [119].

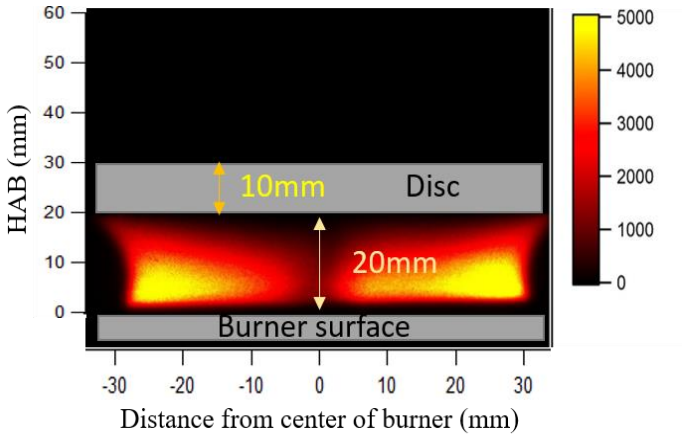

Figure 3.3: A sample OH PLIF image recorded at Φ=1.0 flame reprinted from [119]

Shown in Figure 3.3 is a sample OH PLIF image of a stoichiometric C_2H_4 /air flame. The presence of a 7.4-mm diameter central tube is clearly visible in the flame structure. OH radicals are present mainly in the hot reaction zone and hence a good marker of the reaction zone.

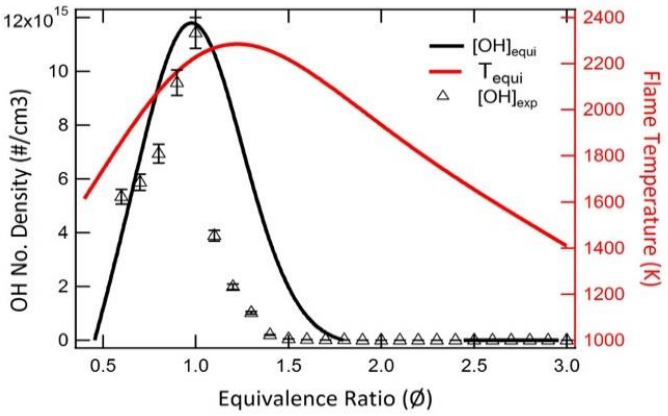

Figure 3.4: OH-PLIF signal intensity and calculated equilibrium [OH] along with measured flame temperatures as a function of Φ reprinted from [119].

The OH PLIF intensity distribution is symmetric around the central vertical axis; however, the maximum intensity was observed approximately 5–6 mm height above burner (HAB) location indicating a flame lift-off. Furthermore, with increasing HAB, OH intensity reduced because of lower temperatures resulting from incomplete combustion and wall quenching effects near the disc. OH PLIF images recorded for other flames conditions exhibit similar behavior.

Figure 3.4 shows the variation of total integrated OH signal as a function of Φ. Calculated equilibrium OH number densities and adiabatic flame temperatures using the Cantera equilibrium code [14] are also shown. Each data point is an average of accumulation of 300 laser shots in one frame and the uncertainty has been estimated as 5% of the signal value based on typical experimental observations. Meibner et al. [121] performed spatially resolved temperature measurements using three-color vibrational CARS on flat flame Mckenna burner using a similar flame stabilizing disc setup. Their experimental temperatures [121] were approximately 7% lower than the adiabatic temperatures shown in Figure 3.4. Negligible OH signals were observed for rich flames beyond Φ=1.5.

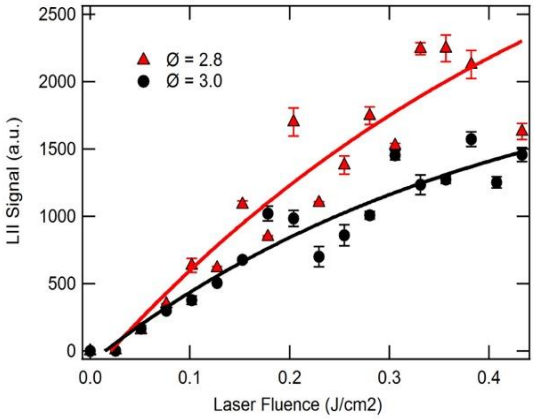

Figure 3.5: f_v as a function of laser fluence for Φ = 2.8 and 3.0 recorded using excitation wavelength of 1064 nm reprinted from [119].

The equilibrium OH profile is slightly broader on the rich side. This effect can be explained because Cantera calculations neglect the heat transfer effects, which is also verified by T_{CARS} [121] being lower than T_{equi}. As Φ is increased beyond 1.5, the rapid drop of the flame temperature and the diminishing the hot reaction zone as evident by the OH signals indicate incomplete oxidation and potential sooting flame conditions.

An initial laser fluence dependence study was conducted by varying the laser fluence from 0.1–0.4 J/cm^2 and the corresponding 1064-nm results are shown in Figure 3.5. The plotted LII signal is the average value of the total signal between the disc and the burner surface. The data has been accumulated as an average of 40 laser shots over 3 frames. A deviation from the linear dependence can be observed beyond approximately 0.2 J/cm^2, hence the laser fluence was maintained at 0.2 J/cm^2 for all subsequent experiments. This observation is in good agreement with previous LII studies where the soot particle heating is maintained below their vaporization temperature [68, 69, 77, 98].

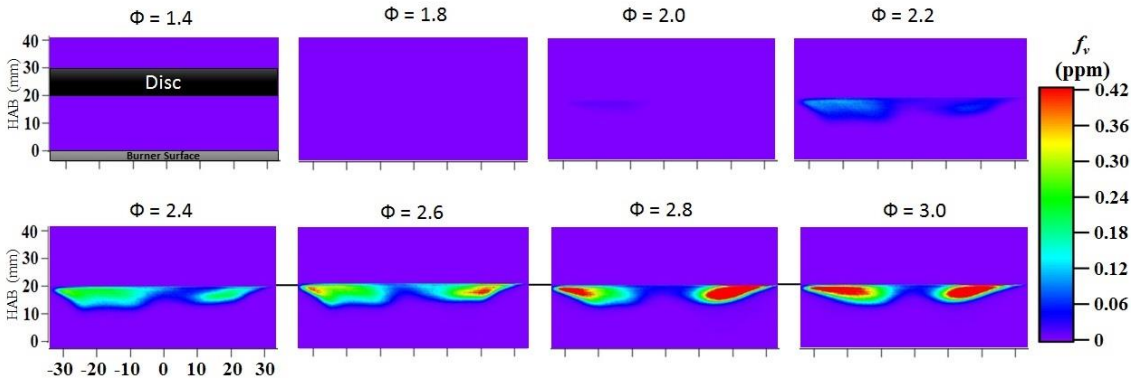

Figure 3.6: 2-D f_v images obtained using 1064-nm LII experiments at different Φ reprinted from [119].

Figure 3.6 shows the calibrated f_V images for a selected set of flames obtained at an excitation wavelength of 1064 nm. There is an apparent decrease in LII intensity at the center of the burner resulting from the no-flow region corresponding to the sealed, central tube. The LII images were calibrated to obtain spatial distribution of fv using the light scattering data from [69]. The path averaged fv was calculated using the equation;

$$f_v = [\lambda/6\pi\, L\, E(m)] \ln(I_0/I) \qquad (9)$$

where, λ is the wavelength, L is path length, Io and I are incident and transmitted intensity respectively, and E(m) is a function of complex refractive index, m of soot. For m= 1.57-0.56i, E (*m*) = 0.2595 [69]. The effective path length obtained from LII images at HAB = 15 mm was approximately 50 mm. The 632-nm He-Ne laser beam was passed through the same spatial location to find the ratio of the incident and transmitted intensities, which varied between (87.8%–99.5%) ± 2.5% for (Φ=3.0–2.1) respectively. Plugging all these values to Equation (9), the values of f_V (in ppm) were obtained for different Φ. The typical uncertainty value range of f_V was estimated to be nearly ±30 %, based on the estimated uncertainties of corresponding experimental parameters.

Interestingly, LII signals were also observed through the 315±15-nm bandpass filter in rich flame conditions during the above OH PLIF experiments. Therefore, care was taken to collect the OH LIF signal at on-resonance (282.581 nm) and at off-resonance (282.592 nm) wavelengths while maintaining the laser energy constant. At each flame condition, background images were also collected with the laser beam blocked. The corrected OH PLIF image was taken as the difference between the on-resonance and off-resonance images. An additional set of LII images were generated by the difference between off-resonance and background signals, and appear nearly identical to the LII images shown in Figure 3.6.

Figure 3.7 shows the variation of f_V as a function of Φ for the three different excitation wavelengths, 1064, 532 and 283 nm. The data was extracted from the corresponding 2D images at 15-mm HAB location using laser fluence of 0.20 J/cm^2 for 532 and 1064 nm, 0.13 J/cm^2 for 283-nm. The 532-nm and 1064-nm data set correspond to an average of 3 frames each with 100 laser shot om-CCD accumulation. The uncertainty was estimated as the standard deviation of the 3 frames. The 283-nm data set was recorded as a single frame at each Φ value, with an accumulation of 300 laser shots per frame, hence the error bars correspond to an estimation of 5% of the signal value. The f_V values obtained using three different excitation wavelengths and at three different detection regimes agree well.

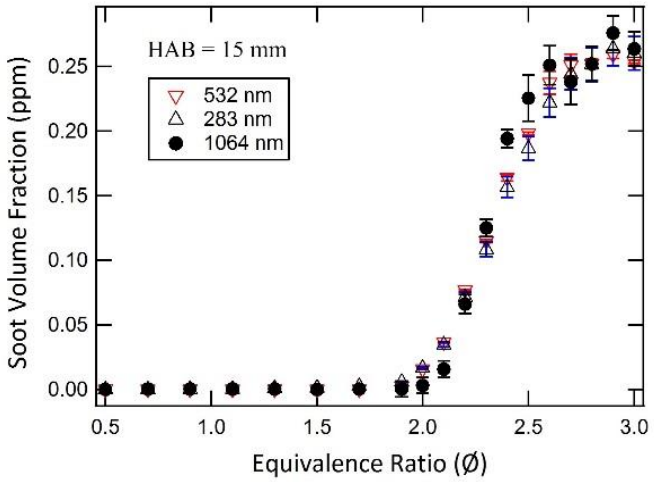

Figure 3.7: Variation of f_v as a function of Φ, obtained using three LII schemes reprinted from [119].

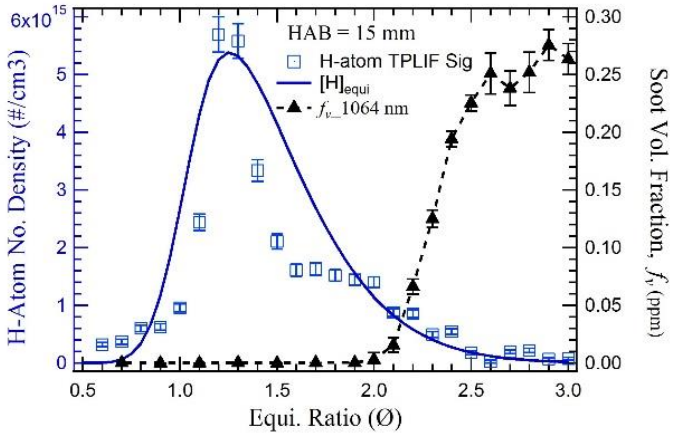

Figure 3.8: Variation of measured and equilibrium H-atom LIF signals, together with experimental f_v as a function of Φ reprinted from [119].

For all excitation wavelengths, f_V is identical at Φ=2.8, since Φ=2.8 was considered for LII calibration. The f_V is almost zero for Φ<1.8 and then increases rapidly up to Φ=2.8 before reaching a near plateau. We took extra care to eliminate fluorescence interference from PAHs while exciting with the 532-nm by implementing a large delay of 400 ns. Since the lifetime of PAHs is much shorter, in the order of approximately 50 ns [98], choosing a longer delay will eliminate PAH interference on the LII signal. Further, interference from C_2, OH and O were blocked by using the narrow bandpass filter (485-500 nm). The plateau region may result because of larger soot particles and agglomeration in very rich flames condition, [77, 87]. The strength of LII signal depend on the total surface area of all the particles combined and the temperature of soot particles. For a given volume, larger particles will have smaller surface area and lower temperatures (for the same laser fluence) compared to smaller particles. Therefore, the emitted black body radiations will be weaker resulting in a plateau region.

In all flames investigated, relative H-atom TPLIF line images were obtained at 15-mm HAB location. Figure 3.8 shows the variation of H-atom LIF signal and the equilibrium H-atom number density (#/cm^3) calculated using the Cantera equilibrium code, along with f_V profile obtained using 1064-nm LII as described in Figure 3.7. The experimental data shown corresponds to the HAB = 15 mm. The H-atom 2pLIF signal corresponds to the total integrated signal of 300 single-laser-shot on-CCD accumulations and the uncertainty was determined as 5% of the data value at that point.

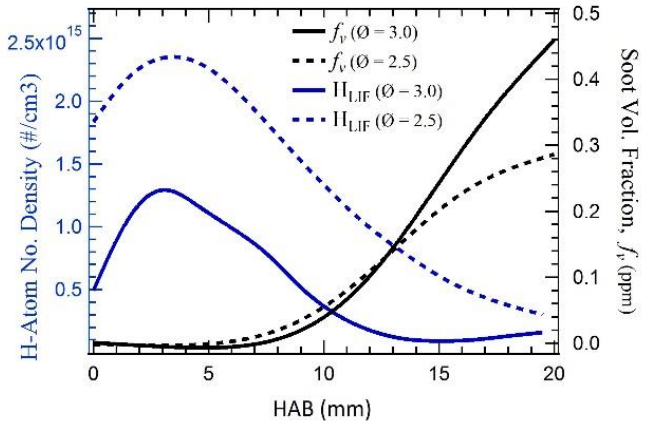

Figure 3.9: Variation of H-atom LIF signal and f_v as a function of HAB reprinted from [119].

The maximum calculated [H] is observed at around Φ=1.3 which is also the Φ corresponding to the maximum adiabatic flame temperature. Moreover, LIF signal started to decrease as Φ is increased further. This general behavior is well predicted by the experimental H-atom profile, although a complete agreement may not be expected because of the non-adiabatic nature of the flat flame. Moreover, fv starts to increase with increasing Φ. This behavior can be partially attributed to the decrease in flame temperature as a result of incomplete combustion in rich flames. Lower flame temperatures reduce the

reaction rates, thereby, producing less intermediate radical species such as H-atom. Thus, the data in Figure 3.8 suggests f_V is inversely proportional to [H] under rich flame conditions investigated.

To further investigate this phenomenon, the integrated f_V obtained using 1064-nm LII and H-atom 2pLIF signals as a function of HAB are plotted for $\Phi = 2.5$ and 3.0 flames in Figure 3.9. A monotonous increase in f_V is observed for the entire range of Φ. The particle diameter increases with HAB and thus, LII signal increases [77]. LII signal was negligible for heights very close to the surface, because the flame lift-off as evident from Figure 3.2 and Figure 3.6 above. It can also be observed that in approximately 5–10 mm HAB region, the f_V is slightly higher for $\Phi = 2.5$ flame as compared to $\Phi = 3.0$ flame. This observation can be explained by the higher flame lift-off for higher Φ.

In contrast, the peak H-atom signal is observed at approximately 3-mm HAB location for both Φ. The reaction zone lies several mm above the burner surface because of the flame lift-off as evident from OH PLIF image shown in Figure 3.3. This observation is also in good agreement with previous H-atoms concentration profiles in similar flat flames [10, 14]. Moreover, with increasing HAB, the H-atom concentration decreased because of lower flame temperature and wall quenching effects from the disc. While it is not possible to establish a direct relationship between H-atom concentration and f_V, an overall inverse proportionality is observed for the flame conditions investigated in this study.

3.3 Summary

In this study, the dependence of soot formation on H-atom concentration was investigated in a selected set of premixed C_2H_4/air flames. The spatially resolved soot volume fractions, f_V were obtained using LII and relative H-atom concentration profiles were generated using recently demonstrated fs-2pLIF techniques. The soot formation mechanisms suggest that H-atoms are being formed and consumed during PAH formation. However, the net [H] depends on the rates of these reactions and the spatial location of the flame. 2-D LII images were obtained using three different excitation/detection wavelength schemes. There is a strong dependence of f_V and [H] on the flame temperature. It can be concluded that the lower flame temperatures result in reduced [H] and supports soot formation (as evident from Figure 3.4 and 3.9). The present study can be a significant step forward in developing and validating 2-D flame models for rich hydrocarbon flames, taking into account the soot formation mechanisms and the role of key reactive intermediates such as hydrogen atoms.

4. THREE-PHOTON LIF DETECTION OF ATOMIC HYDROGEN*

In many recent studies, ultrashort, femtosecond 2-photon (2p) laser-induced fluorescence (LIF) of H-atom has been demonstrated using 205-nm excitation. However, 205-nm- deep UV pulses can be problematic in practical devices containing thick transmissive optics and also susceptible to photolytic production at high laser energies. In the present study, we investigate the 3-photon (3p) excitation scheme of H-atom by using red-shifted 307.7-nm fs laser pulses. Efficient 3p excitation resulting from intense fs laser pulses enable 3pLIF detection of H, which was previously unattainable in most flame conditions using ns or ps excitation. Measurements are reported in atmospheric pressure $CH_4/O_2/N_2$ Bunsen jet flames and premixed CH_4/air and H_2/air calibration flames and compared with similar 2pLIF schemes with fs pulses. Saturation effects, photolytic interferences, and stimulated emission effects are studied, as well as benefits of 3pLIF in diagnostic hardware with thick optical windows are discussed.

4.1 Multi-Photon Excited H-atom Detection

H-atom detection using two photon LIF has been discussed in detail in section 2.2.3. Even though, 2pLIF is a very powerful diagnostic tool for detecting H-atom, its implementation in practical combustion devices having thick optical windows is very limited due to the absorption of DUV (205-nm) wavelength.

---

*Part of this chapter is reprinted with permission from "Three-photon-excited laser-induced fluorescence detection of atomic hydrogen in flames" by A. Jain, Y. Wang, and W. D. Kulatilaka, Optics Letters 44 (2019) 5945-5948. Copyright [2019] by The Optical Society of America.

This section summarizes different schemes that have been implemented to detect H-atom via multi-photon excitation in different flames and plasma devices.

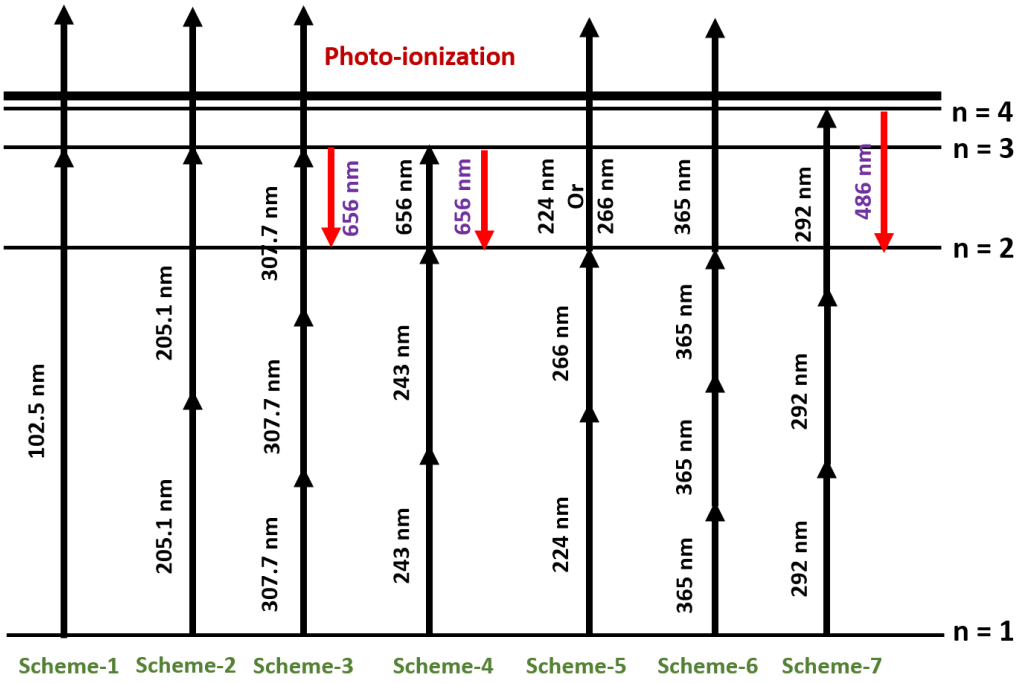

Figure 4.1: Energy level diagram for H-atom.

Figure 4.1 summarizes all the multi-photon excitation schemes that can be implemented for the detection of H-atom in flames and plasma devices. Detection of ground state H-atom by resonant three photon ionization scheme (Scheme-5) have been demonstrated by Bjorklund et al. [122, 123].

In scheme-5, the absorption of three photons (two photons at frequency of ω_1 (266-nm) and one photon at the frequency of ω_2 (224-nm)) results in ionization. For resonance enhancement $\omega_1 + \omega_2$ must be in resonance with $n = 1 \rightarrow n = 2$ transition. Further, other linear combinations of ω_1 and ω_2 were neglected since the power density of ω_2 was negligible compared to ω_1. The main disadvantage of this technique is that the excitation

wavelength of 224-nm falls within γ-band of nitric oxide (NO) and thus, the resulting ionization signals interferes with the H-atom signal whenever H-atom is being probed in the flames containing nitrogen.

A similar excitation scheme using resonance four photon (4p) ionization (λ = 365 nm) was demonstrated by Tjossem et al. [124] in 1983. The main advantage of this ionization schemes is the utilization of a single dye-laser and no frequency doubling as compared to the three-photon ionization demonstrated by Bjorklund et al. Further, red-shifting the wavelength from UV (224-nm and 266-nm in 3p ionization) to near-visible (365-nm) potentially eliminated the photolysis and other laser induced interferences arising from shorter wavelengths. However, in 4p ionization, very high laser intensities are required because of weaker cross-sections (3p absorption process) and significant interferences from NO have also been found [125].

Thus, in order to implement any multi-photon excitation scheme two generalities will be applicable in all the cases:

(i) Red-shifting the wavelength is always recommendable because longer wavelength has low energy photon which are less-likely to photo-dissociate the species as compared to shorter wavelengths, thereby, reducing the interference caused by photolysis.

(ii) Lesser the number of resonance photons, better it will be, since a greater number of photons required for resonance transitions reduces the absorption cross-sections significantly.

Unfortunately, both conditions (i) and (ii) are not simultaneously satisfied in most situations. Therefore, all these multi-photon excitation schemes have their own advantages and disadvantages.

The detection of H-atom via 3pLIF was first demonstrated by Alden et al. [126] in 1984 (Scheme-7). The electrons were excited from the ground state, n = 1→→→ n = 4 via 3p absorption at an excitation wavelength of 292-nm. The fluorescence (Balmer-β radiation) was collected at λ = 486-nm resulting from the spontaneous transition decay from n = 4 → n = 2. In addition to Balmer- β radiation, electrons can be transferred from n = 4 to n = 3 via collisions and thus, results in Balmer-α radiation (λ = 656-nm) via spontaneous decay from n = 3 → n = 2. However, authors mentioned that the strength of Balmer-α radiation, in this case, is only 10% that of Balmer- β radiation.

Further, it should be noted that the authors were unsuccessful in demonstrating 3p excitation technique from n = 1 to n = 3 (λ = 307-nm) and from n = 1 to n = 5. The reason being, in the former case the laser power was too low. Also, the OH interferences at 307-nm could not be eliminated because of the lack of filter technology that time. However, interferences from the background levels set the limitations for the latter case.

Further, Goldsmith [16, 125] compared the three multi-photon excitation techniques (2p excitation (λ = 205-nm) (Scheme-2), 3p excitation (λ = 292-nm) (Scheme-7) and two step laser excitation using two photons (λ = 243-nm) followed by a single photon (λ = 656-nm)) (Scheme-4) for the detection of H-atom in low pressure acetylene-oxygen-argon flame. The results for the H-atom fluorescence yield obtained by using the above-mentioned multi-photon excitation schemes were recorded at different heights

above the burner (HAB). It was observed that for 20-80 mm HAB, the LIF profiles are in good agreement for all the schemes. However, just above the surface of the burner (0-20 mm HAB), it was realized that two-step excitation scheme is the most reliable, as mentioned by the authors. The reason being, 2pLIF suffer from unidentified interference, resulting in a sharp H-atom LIF peak near the burner surface. However, the large 3pLIF signal in the range 0-20 mm HAB is due to the production of H-atom from the photolysis of acetylene and interference from electronically excited C_2 molecules. The Swan band emission from these C_2 molecules can significantly interfere with observed H-atom LIF emission. Thus, authors recommended to implement two-step excitation scheme to obtain more reliable signals.

In 1990, Goldsmith et al. [127] proposed another single laser two-step excitation scheme to detect H-atom using 2 photons of λ = 243-nm followed by a single photon of λ = 486-nm instead of 656-nm (as used in the previous two-step excitation scheme). The use of single laser helped in the easement of the process by making the experimental setup less expensive and less susceptible to complexities. In the recent decade, several researchers have applied 3p excitation scheme (λ = 292-nm) to detect H-atom in diamond forming flames [128], counter flow diffusion flames [129] and to detect and discriminate individual bio-aerosol particle [130].

To summarize, the only reported 3pLIF experiments are limited to the 3p excitation wavelength using 292-nm pulses in atmospheric-pressure flames. However, 307.7-nm 3pLIF experimental attempts via pumping to the commonly used n=3 state have not been reported thus far. It is expected that Balmer-α (n=3 $\rightarrow$ n = 2) emission cross-

sections are an order of magnitude or more, higher than that of Balmer-β (n=4 → n = 2) [131] as well as the efficiency of the fs wavelength generation scheme of commercial optical parametric devices are approximately a factor of two higher at 307 nm compared to 292-nm. These are two primary motivations for the present study, during which we successfully implement the 307.7-nm fs-duration pulses for 3pLIF detection of H in a variety of flame conditions.

4.2 Comparison of 2pLIF and 3pLIF detection schemes

4.2.1 Related Instrumentation

Figure 4.2 shows a schematic of the fs-laser experimental apparatus used for the comparison of 2pLIF and 3pLIF schemes during the present study. It consisted of a 1-kHz repetition-rate Ti: sapphire laser (Spectra Physics, Model: Solstice Ace) that generated approximately 80-fs duration laser pulses. The peak pulse energy of the output beam at 800-nm was 6 mJ/pulse. After the parametric conversion and subsequent frequency mixing steps, the resulting 205.1-nm beam had a peak output energy of 10 μJ/pulse, while the peak output energy of the 307.7-nm beam was 50 μJ/pulse. After a set of guiding mirrors, a plano-convex converging lens (+500-mm for 205.1-nm and +1000 mm for 307.7 nm, Lattice Electro Optics, Part Nos UF-PX-25.4-500 & UF-PX-25.4-500) was used to focus the beam at the center of the $CH_4/O_2/N_2$ premixed Bunsen jet flame having an exit diameter of 4-mm.

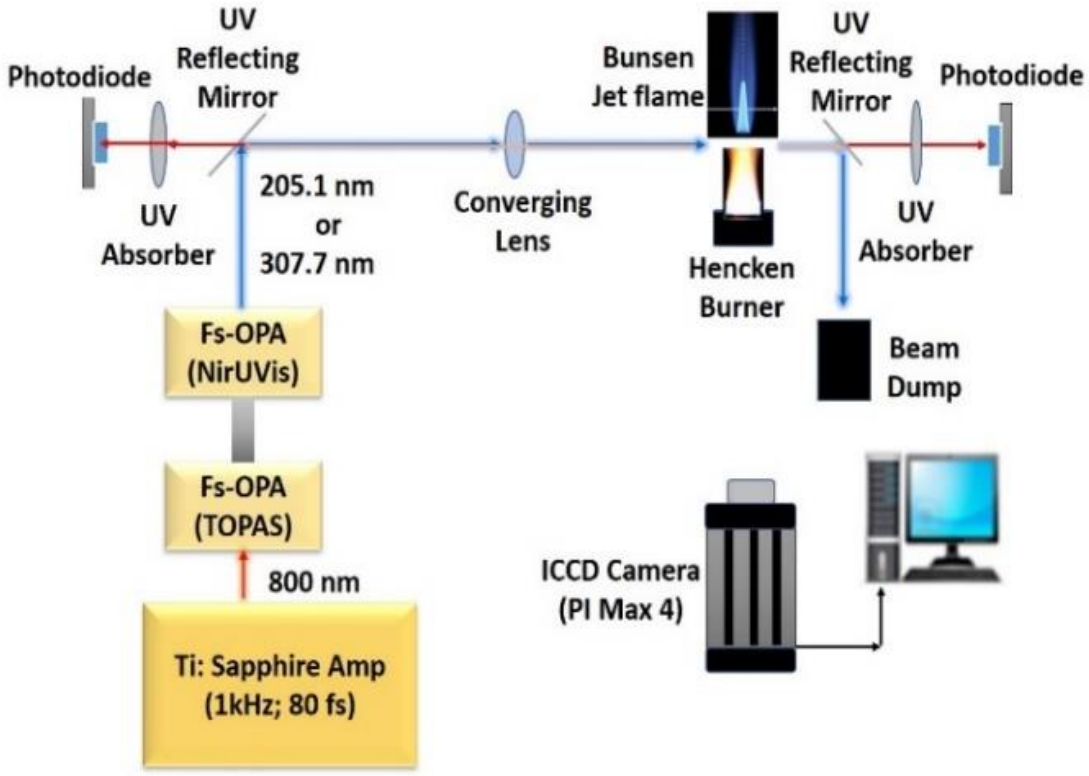

Figure 4.2: Schematic of the experimental apparatus reprinted from [132].

The flame equivalence ratio (Φ) was maintained at 1.0 (CH_4: 0.3 slpm, O_2: 0.6 slpm, and N_2:1.7 slpm), and operated with dry air shroud flow of 10 slpm flown through a 50-mm diameter annular honeycomb for flame stabilization. The H-atom line images were recorded using an intensified CCD (ICCD) camera (Princeton Instruments Model: PI-Max4) with a typical intensifier gate width of 50 ns encompassing the laser pulse. A 656 ± 3 nm (Andover Corporation; Part number # 656FS03-25) filter was employed with the camera lens to avoid any flame and scattered laser light interferences. The SE signal was also recorded for both forward and backward lasing directions using two fast

photodiodes (Thorlabs; Model: DET 210). Plexiglass UV absorber plates were placed in front of the photodiodes to eliminate trace quantities of excitation UV laser beams interfering with the SE signal detected. In all measurements, the background signals were recorded separately by blocking the excitation laser beam and then subtracted off from the corresponding signals.

4.2.2 Results and Discussion

We investigated 3pLIF detection of H using λ =307.7-nm fs-duration laser pulses and compare the advantages and limitations of this scheme with the commonly used 2p excitation method. Measurements are reported in premixed $CH_4/O_2/N_2$ Bunsen flames as well as premixed adiabatic CH_4/air calibration flames.

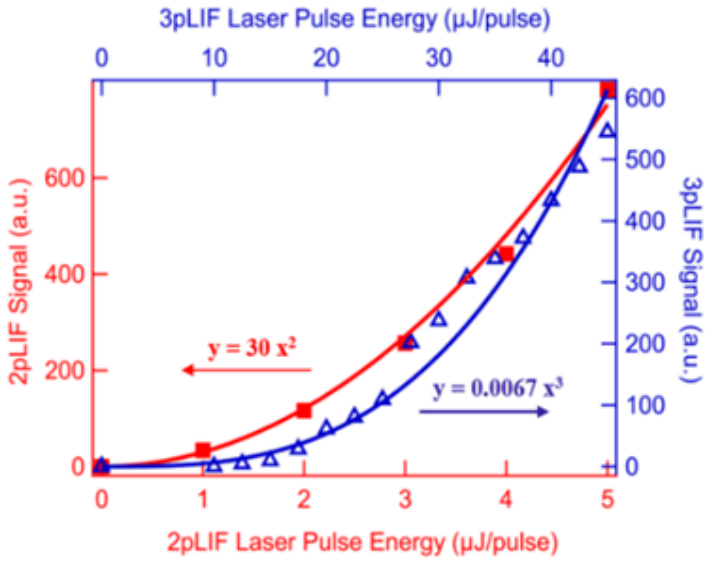

Figure 4.3: Dependence of 2pLIF and 3pLIF signals as a function of laser energy. Solid lines represent the curve fits given by the shown equations reprinted from [132]

In general, $Sig_{LIF} \propto I^n$, where I = laser fluence and n = number of photons involved in the excitation process from the ground electronic state to the upper electronic

state. Thus, the 2pLIF signal and the 3pLIF signal should be proportional to I^2 and I^3 respectively, before reaching the saturation regime. Experiments were conducted by Figure 4.3 shows the variation in the 2pLIF and 3pLIF signals as a function of laser pulse energy. The estimated beam diameters of the collimated beams prior to final focusing lens for 2p and 3p LIF cases are 3 mm and 7 mm, respectively. As expected, the 2pLIF signal exhibited quadratic dependence on laser pulse energy. The 3pLIF signal demonstrated a nearly cubic dependence on laser pulse energy, particularly below approximately 30 μJ/pulse, while a linear dependence with moderate deviation at higher laser pulse energies observed, which may result from plasma generation at the focal point of the beam. It should be noted that Brockhinke et al. [129] have reported a nearly linear power dependence when using ps-duration pulses. To minimize plasma generation, 1000-mm focal length converging lens was used for all 3pLIF studies as mentioned previously. Each data point in Fig. 4.3 correspond to an average of 3 ICCD frames where each frame is also an average of 150 and 800 laser shots for 2pLIF and 3pLIF, respectively. The ICCD gain was maintained at 80% in both cases.

For the same imaging parameters and laser pulse energy, the 2pLIF signal is approximately 40 times stronger than the 3pLIF signal, primarily because of the weaker three-photon cross-section as compared to that of the two-photon scheme. As seen in Fig. 4.3, the 2p and 3p LIF signals of H-atom did not reach the saturation regime. Because of the quadratic and cubic laser power dependencies, in the absence of photolytic production, the photo-ionization effects can be estimated to be negligible in the pulse energy regimes investigated. The substantial presence of photoionization effects would have caused a

considerable deviation from the quadratic and cubic dependencies for 2pLIF and 3pLIF, respectively. A detailed investigation of potential photolytic production of H-atoms from other H-containing flame radicals is discussed in the subsequent section.

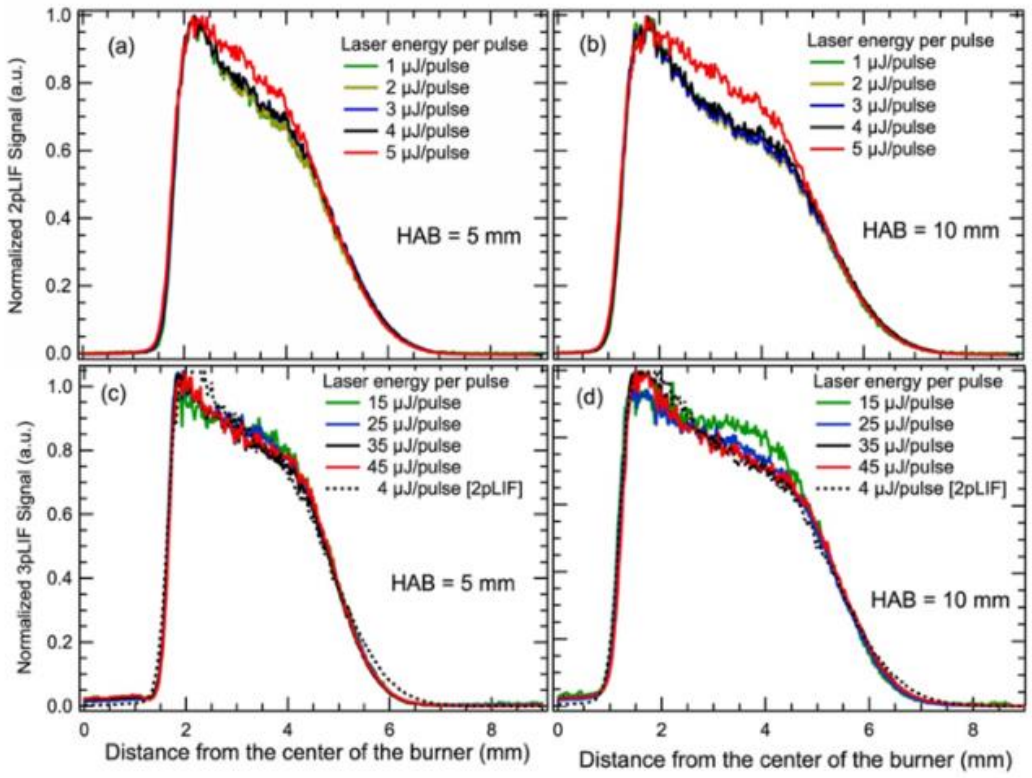

Figure 4.4: H-atom LIF line profiles as a function of distance from the center of the burner, for different laser energies. (a) 2pLIF at HAB = 5 mm, (b) 2pLIF at HAB = 10 mm, (c) 3pLIF at HAB = 5 mm, and (d) 3pLIF at HAB = 10 mm. 2pLIF profiles corresponding to 4µJ/pulse cases are also overlaid in (c) and (d) for easy comparison reprinted from [132].

The relative shape of the fluorescence line image recorded through sharp flame structure gradients can be used to estimate the photolytic production of H-atom by intense excitation laser pulses. Shown in Figure 4.4 are the spatial variations of the H-atom line profiles for 2pLIF and 3pLIF schemes as a function of the radial distance from the center of the Bunsen burner. The laser pulse energies were varied from minimum to maximum

using a variable neutral density filter, and the results for the height above the burner (HAB) of 5-mm and 10-mm are shown. Since the jet flame was axisymmetric, the signal is only shown for the right half of the flame. Each data set corresponds to an average of 3 ICCD frames with each frame containing on-CCD accumulations of 150 and 800 laser shots for 2pLIF and 3pLIF cases respectively. All line profiles are normalized to the peak signals, as this enabled comparison of H-atom line profile shapes, and visualization of any deviation as the laser pulse energy is increased. As expected, the absolute signal levels increased with an increase in HAB. The central region of the bright inner cone in the jet flame corresponds to the part of the unburned premixed gas mixture. Therefore, H-atom concentration is zero in that region of the flame. Further, since the diameter of the combustion zone increases with increasing HAB, wider fluorescence signal profiles are observed at higher HAB locations. The sharp rise in signal intensity at a distance of approximately 2-mm from the center represented the edge of the bright central cone, the area of the stationary flame front with highest flame temperature and the reactive radical concentration.

For 2pLIF cases, near-overlap of the spatial line profiles was observed for pulse energies ranging from 1–4 μJ/pulse. This observation is an indication of negligible photo-dissociation of methyl radical (CH_3) in the flame front and vibrationally excited water vapor present in high concentrations in combustion products zone [13, 25, 26]. Photolysis of water can produce H-atom in the product zone of the flame in levels significantly higher than those naturally present in the flame [25, 26]. However, for the highest pulse energy of 5 μJ/pulse, change in H-atom line profile shape was observed in comparison to those

with the lower pulse energies. This observation is potential excess H-atom resulting from the photolytic production by the laser pulse. Therefore, 2pLIF studies should be performed below 4 μJ/pulse to obtain interference-free H-atom profiles in these flames. As described above, pulse energies used for 3pLIF scheme were significantly larger than that for 2pLIF scheme. Therefore, the ionization effects and potential laser sparks for 3pLIF were minimized by using a 1000-mm long focal length lens. This method enabled imaging of the H-atom fluorescence signals nearly free of photolytic interferences, as evident from the excellent overlap of spatial line profiles. It should also be noted that the per photon energy decrease by almost 33% when the laser wavelength is tuned from 205-nm to 307-nm, a feature which was previously thought to be advantageous in terms reducing photolytic interferences [128] amid the reduced 3p excitation efficiency. At the lowest-pulse-energy case in 3pLIF, at 10-mm HAB, the shape did not match well with the other profiles as seen in Figure 4.4 (d). This discrepancy is attributed to the reduced signal-to-noise ratio, which is approximately 3.5x lower in the 15 μJ/pulse case as compared to that of the 45 μJ/pulse case.

For quantitative H-atom concentration measurements, it is also essential to investigate the effects of SE on the fluorescence quantum yield for both 2p and 3p excitation schemes. It is shown in Figure 4.5 the forward propagating SE signal recorded as a function of laser pulse energy at the 5-mm and 10-mm HAB locations during 2pLIF. The backward lasing SE emission signal was also recorded using the similar photodiode placed opposite to the direction of beam propagation (not shown in Figure 4.5). However, a similar dependence of SE emission on power was observed for forward and backward

lasing. Overall, the SE signal at 10-mm HAB is higher than that at 5-mm HAB for all laser pulse energies because of the increase in H-atom number density along the beam path primarily due to the longer flame region at higher HAB locations.

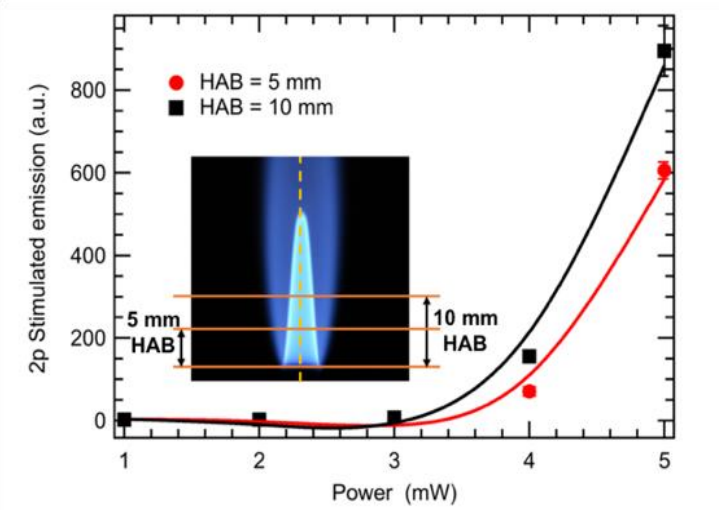

Figure 4.5: 2-photon stimulated emission profiles as a function of laser power at HAB = 5 mm and 10 mm. Solid lines are smoothing spline fits to guide the eye reprinted from [132].

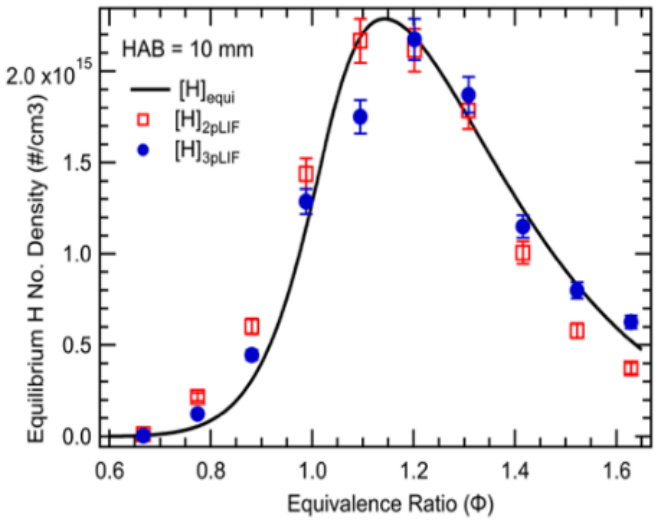

Figure 4.6: 2pLIF and 3pLIF H number density as a function of Φ reprinted from [132].

Further, highly non-linear dependence of the SE signal on laser pulse energy was observed. The SE signal was negligible for lower laser energies, and a sharp onset of SE generation was observed at energies greater than 4μJ/pulse. Higher SE emission increased the loss rate of the excited state population, which resulted in less intense fluorescence signals. Interestingly, there was no detectable SE signal for all 3pLIF cases. We attribute this observation to the significantly less excited-state population in the case of 3pLIF scheme because of lower 3p excitation cross-sections.

To demonstrate the applicability of fs 3pLIF scheme for practical flame studies, H-atom LIF signals using 2p and 3p excitation schemes were measured as a function of Φ in a series of premixed adiabatic CH_4/air flame stabilized over a Hencken calibration burner. The raw LIF signals are compared with equilibrium H-atom number densities calculated using CANTERA code in Figure 4.6. No fluorescence quenching corrections are applied to these measurements, and the relative LIF profile shape is scaled to match with the calculated H-atom number density profile. The experimental data from 2pLIF and 3pLIF follow the equilibrium calculations; although, the 3pLIF scheme demonstrates approximately a 20% better fit based on root-mean-square error method. We attribute this observation to, reduced photolytic production and SE interferences in the 3pLIF scheme.

Furthermore, to demonstrate the practical advantages of red-shifting the excitation wavelength to reduce transmission losses through windows, we inserted two 10-mm thick UV fused silica (UVFS) optical windows (Lattice Electro Optics; Part #: UF-WP-2038) in the laser beam. Interestingly, for 3pLIF excitation scheme at λ = 307.7-nm, the pulse energy decreased from 45 μJ/pulse to 40 μJ/pulse, whereas for 2pLIF scheme at λ = 205.1-

nm, the optical windows absorbed more than 50% of the UV pulse energy. Subsequently, no 2pLIF signal could be detected because of the low signal-to-noise ratio even in $\Phi = 1.1$ flame. Furthermore, in the $\Phi = 1.1$ flame, the 3pLIF signal dropped by ~60% when above 20-mm thick UVFS optical path length was introduced. Therefore, these observations suggest in addition to the absorption losses of the excitation laser energy, the higher order nonlinear effects and the resultant reduction in multi-photon excitation efficiency are significantly less problematic in 3pLIF scheme as compared to 2pLIF scheme when using fs laser pulses. Therefore, we expect the 3pLIF using λ = 307.7-nm photons to have additional benefits for imaging diagnostics of H-atom in facilities fitted with thick optical windows such as high-pressure flames and various practical combustion systems such as IC engines and gas turbines test rigs. It should be noted however though single-laser shot imaging diagnostics are not feasible with the level of pulse energies available in present-day commercial fs-laser systems.

4.3 H-atom Detection in Adiabatic Flames via 3pLIF

In the present study, we investigate fs-3pLIF for detecting H-atom in adiabatic atmospheric hydrogen-air flames. The results were found to be in agreement with the numerical calculation data (obtained from [23]) and equilibrium measurements.

4.3.1 Experimental Details

A similar experimental setup, as described in section 4.2.1, was used with few modifications. A converging lens (+1000 mm focal length) was used to focus the 307.7-nm output beam at the center of H_2/air flame (with dry air shroud flow of 10 slpm)

established over 1.5” X 1.5” Hencken burner. The equivalence ratio (Φ) was varied from 0.8 (Air flow rate = 50 slpm; H_2 flow rate = 16.8 slpm)-2.2 (Air flow rate = 50 slpm; H_2 flow rate = 46.2 slpm) and the height above the burner (HAB) was varied from 0 mm to 50 mm by translating the burner vertically. The fluorescence images were captured using an intensified CCD (ICCD) camera (Model: Princeton Instruments PIMax4) with a gate width of 100 ns. An additional narrow band pass filter (656 ± 3 nm) was put inside the camera lens to avoid interferences from other species (OH) and flame emissions. The background signal was captured separately and subtracted from individual images to obtain the absolute H-atom signal.

4.3.2 Results and Discussion

The results of equivalence ratio scan, height scan and power scan were done on the Hencken burner without the central tube, thereby ensuring the uniform adiabatic flame region.

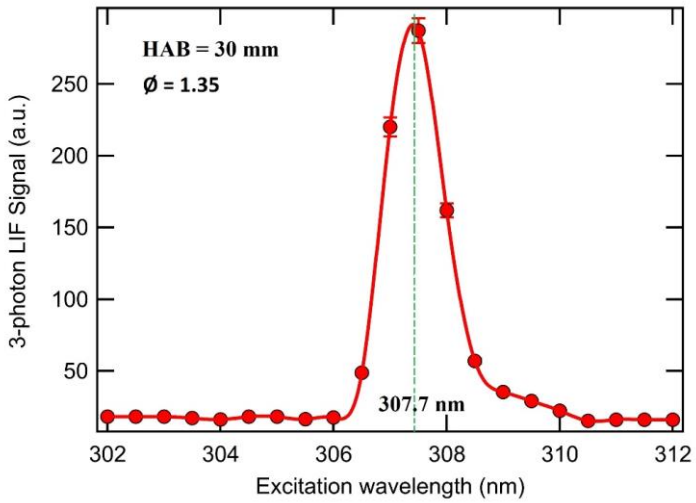

Figure 4.7: 3pLIF signal intensity as a function of excitation wavelength in H_2/air flame.

Figure 4.7 shows the variation of 3pLIF signal intensity as a function of excitation wavelength for 3-photon transition from n=1 to n= 3 at Φ = 1.35. Each data set is an average of 30 measurements and 800 on-ccd accumulations. The maximum signal was observed at 307.7 nm (marked in green color) and thus, it was chosen to be the optimum excitation wavelength for 3pLIF. Further, the full width half maximum (FWHM) of the excitation line is about 2-nm.

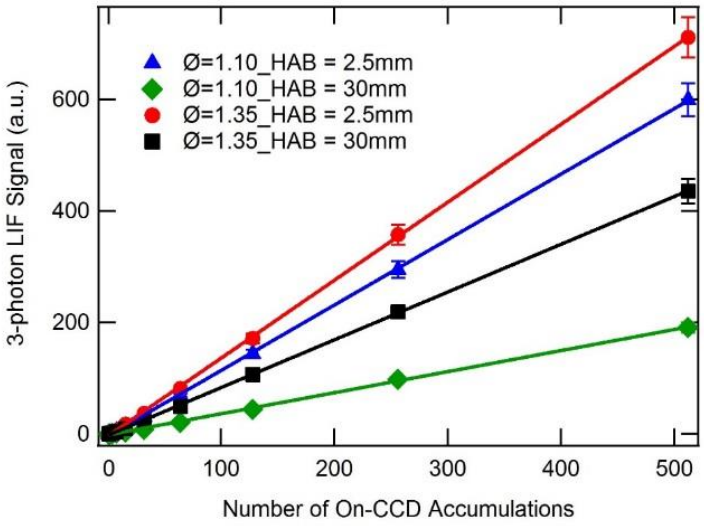

Figure 4.8: Variation of 3pLIF signal intensity and # on-CCD accumulations.

Figure 4.8 shows the variation of 3pLIF signal as a function of number of on-ccd accumulations. The uncertainty has been calculated as a standard deviation over 30 measurements. This was done as reference test to detect the sensitivity of the 3pLIF in H-atom. Each data point is an average of 20 individual measurements taken at 100% gain and gate width of 100 ns. Further, the data was collected for Φ = 1.1 and 1.35 at HAB of 2.5 mm (just above the surface of the burner) and 30 mm (equilibrium position for Φ = 1.1 and 1.35). For all these cases, monotonous increment in LIF signal was observed for

an increment in # on-ccd accumulations. However, it should be noted that the signal was almost negligible up to 32 on-ccd accumulations. Thus, we had chosen 800 on-ccd's for all the further measurements. It was realized that signal decreased drastically with increase in HAB. A detailed discussion of this result has been given in the follow-up sections.

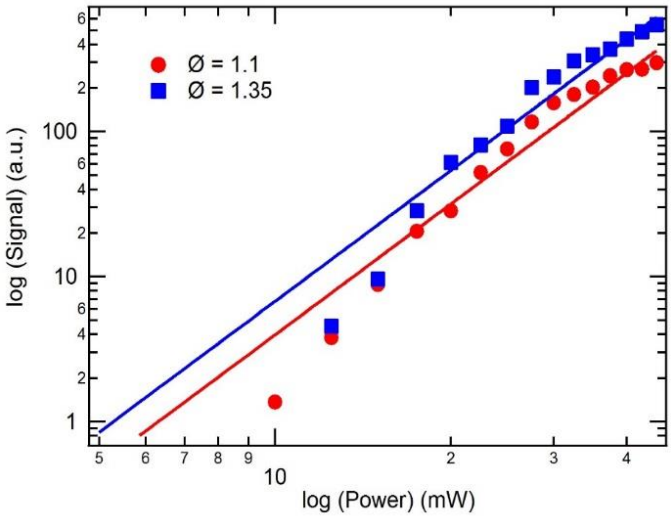

Figure 4.9: Variation of LIF signal as a function of laser power in H_2/air flame.

Figure 4.9 shows the variation of LIF signal as a function of laser power for Φ = 1.1 and 1.35. A variable neutral density filter was placed in the path of the laser beam to vary the laser power. When there is no saturation, the LIF signal is given by:

$$Sig_{LIF} \propto I^n$$

$$log_{10}(Sig_{LIF}) = c + nlog_{10}(I)$$

Where,

I = laser intensity

n = number of photons involved in the transition from the ground electronic state to the excited electronic state

c = constant

Each data set is an average of 30 measurements and 800 on-ccd accumulations and uncertainty was calculated as standard deviation over 3 individual frames. A linear dependence was observed for both the equivalence ratios, implying that LIF signal is not in the saturation regime. Further, there is slight deviation from the ideal trend for lower powers due to lower signal to noise ratio. Moreover, aberrations at higher power can be attributed to the photolysis of different species. These photolytic interferences were minimized by using a long focal length (+ 1000 mm) converging lens. The equivalence ratio and height scan measurements were recorded for the maximum laser energy of 45 μJ/pulse to maximize the signal to noise ratio without saturating the signal.

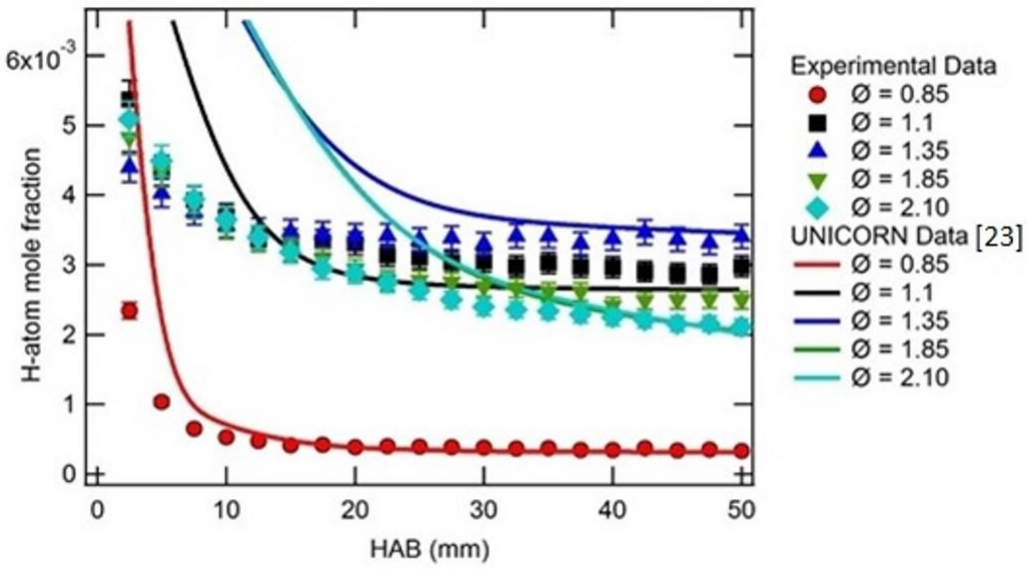

Figure 4.10: Vertical H mole fraction profiles along the centerline of the burner for a series of flames ranging from lean (Φ = 0.8) to very rich (Φ = 2.10). Calculated H mole fraction using numerical modeling code data were extracted from [23].

The H-atom mole fraction has been shown as a function of HAB along the center line of the Hencken burner for different Φ in Figure 4.10. The experimental data has been plotted alongside the numerical calculations obtained from Ref [23]. Further details of the UNICORN code can be found elsewhere [133, 134]. Figure 4.10 provides important information for identifying the regions of chemical equilibrium above the burner for different Φ. This in turn, will be helpful in characterizing the use of Hencken burner as a standard calibration burner.

Each experimental data set is an average of 3 individual frames, each having 30 measurements with 800 on-CCD accumulations, 100% gain and 100 ns gate width. The uncertainty has been calculated as a standard deviation over three frames. In general, the results are in excellent agreement with those obtained on the similar experimental setup using Laser-Induced Polarization Spectroscopy (LIPS) [23]. Further, the mole fraction has been calculated from the H number density using the equilibrium temperature at that particular Φ. It should be noted that the agreement of fs-3pLIF results with numerical calculation was better as compared to H mole fractions obtained using LIPS.

It was observed that vertical H mole fraction profiles agreed with the numerical calculations for slightly leaner (Φ = 0.85) and richer flames (Φ = 1.1 and 1.35) for distances more than 20-mm HAB. However, for very rich flames (Φ = 1.85 and 2.10) numerical code could not predict the actual H-atom mole fractions. Further, the saturation in mole fraction above 30-mm HAB for Φ = 0.85, 1.1 and 1.35 reveals that chemical equilibrium has been attained for these Φ above 20-mm HAB, however, the flame at Φ = 1.85 and 2.10 could not reach the equilibrium even at 50-mm HAB.

It should be noted that for all these experiments, different Φ have been obtained by varying only the mass flow rate of gaseous fuel (H_2 gas) and the flow rate of oxidizer (air) was kept constant. Thus, the fluid velocity increased above the surface of the burner with an increase in Φ. This reduced the residence time of the radicals in the flame for higher Φ. This is the main reason for the slower equilibrium approach of richer flames compared to lean flames. The detailed reasoning about chemical kinetics has been explained elsewhere [23].

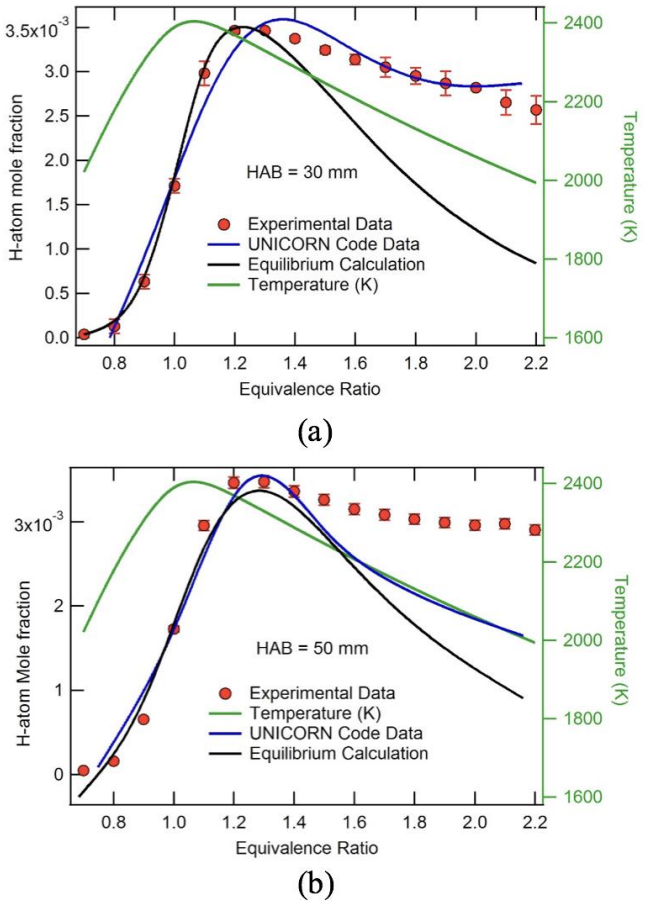

Figure 4.11: Comparison of experimental H-atom mole fraction with equilibrium calculations and numerical data calculation at (a) 30-mm HAB and (b) 50-mm HAB.

Figure 4.11 demonstrates the H-atom mole fraction as a function of Φ for a series of flames ranging from lean to very rich at 30-mm and 50-mm HAB. Further, the equilibrium temperature distribution (calculated using STANJAN) for different Φ and a comparison between the experimental, equilibrium and numerically calculated values is also depicted in Figure 4.11. Each data point is an average of 30 measurements and 800 on-ccd accumulations recorded at 100 percent gain and 100 ns gate width. Further, for each data point, the uncertainty has been evaluated as 5% of the base value.

An excellent agreement was observed between experimental and numerically calculated values at 30-mm HAB up to Φ = 1.8, however, for richer flames the numerical values of mole fraction were found to be higher, as also evident from Figure 4.10. Moreover, at 30-mm HAB, the equilibrium calculations exactly matched the experimental profile until stoichiometric condition and the peak value was obtained at Φ slightly greater than 1.0. However, we observed a monotonous decrease in the equilibrium mole fraction values as the flame got richer. The equilibrium temperature varied from 2000 K to 2400 K with maximum at Φ = 1.0.

At 50-mm HAB, the equilibrium and numerically calculated values are in good agreement with the experimental data for lean and slightly richer flames. However, for Φ > 1.3, the numerically calculated H mole fractions were significantly lower than the experimental measurements. Further, as evident from Figure 4.10 and Figure 4.11 (b), for Φ > 1.5, the adiabatic equilibrium values were found to be even lower than the numerical mole fraction values.

This data validates the acceptability of mole fractions obtained from equilibrium calculations and numerical modeling using UNICORN code. It should be noted that the flow just above the surface of the burner is very complex because of the mixing between the fuel and air coming out of numerous small tubes. Moreover, since it is the region of diffusion flame in the non-equilibrium zone, it is difficult to model and calculate the H-atom mole fraction in this region numerically. Further, the uncertainty in experimental measurements in this region was also very high. Thus, a slight deviation from the experimental values was observed near the surface of the burner. For the Hencken calibration burner, the code seems to work well only for a certain range of HAB and did not predict the concentrations correctly for greater heights for very rich flames. The deviations might arise from turbulence as a result of large fluid velocities at high equivalence ratios and particularly with an increase in HAB, the turbulent effects become more dominant.

4.4 Summary

In summary, we investigated 3pLIF detection of H-atom using λ =307.7-nm fs-duration laser pulses and compare the advantages and limitations of this scheme with the commonly used 2p excitation method. Measurements are reported in premixed $CH_4/O_2/N_2$ Bunsen flames as well as premixed adiabatic CH_4/air and H_2/air calibration flames. The primary advantage of the 2pLIF scheme is the comparatively higher excitation efficiency. However, the DUV excitation wavelength of 205.1-nm can be absorbed by thick optical windows of practical combustion hardware limiting its widespread applicability, which can be largely avoided using the 3pLIF scheme. Moreover, the energy per photon is higher

in the case of 2p excitation; thus, 2pLIF signals appear to be more susceptible to photolytic interferences. In the range of 3p pulse energies investigated, no photolytic interferences and SE were observed. Typical 3pLIF signal is approximately a factor of 40 weaker than 2pLIF signals because of weaker 3p absorption cross-sections. Furthermore, the 3pLIF scheme utilizes red-shifted UV photons near 307-nm, thereby making it more suitable for diagnostics in realistic combustion hardware containing thick optical windows.

5. SIMULTANEOUS IMAGING OF ATOMIC HYDROGEN AND HYDROXYL RADICALS

Atomic hydrogen (H-atom) and hydroxyl radical (OH) are two key intermediate species in the combustion of hydrocarbon fuels. The spatial and temporal distribution of H-atom is useful to better understand the ignition/extinction processes and soot formation pathways, whereas OH distribution profiles can yield flame structure and reaction zone in different flames conditions. In the present study, simultaneous laser-induced fluorescence (LIF) measurements of H-atom and OH are obtained using a single ultrashort femtosecond-duration laser pulse near λ = 307.7-nm. Measurements are performed in CH_4-air and C_2H_4-air flames stabilized over the Hencken calibration burner. Recently developed three-photon LIF (3pLIF) technique is used for H-atom, whereas the same excitation laser pulse can simultaneously excite OH $A^2\Sigma^+ \leftarrow X^2$ (0,0) transition. Red-shifting the excitation wavelength to 307.7-nm as opposed to commonly used two-photon excitation using 205-nm deep-ultra-violet (DUV) laser pulses enables the reduction of absorption losses of excitation laser pulse energy when transmitting through thick optical windows of high-pressure vessels, for example. Furthermore, the efficiency of the fs wavelength generation scheme of commercial optical parametric devices are approximately a factor of two higher near 307.7-nm as compared to 292-nm. In this study, H-atom and OH number densities have been reported for a range of flame equivalence ratios in CH_4/air and C_2H_4/air flames established over the Hencken calibration burner. Simultaneous imaging of H-atom and OH in premixed Bunsen flame are also discussed.

The present study shows the potential of using a single laser pulse for imaging multiple chemical species in flames.

5.1 H-atom and OH Radical Excitation Schemes

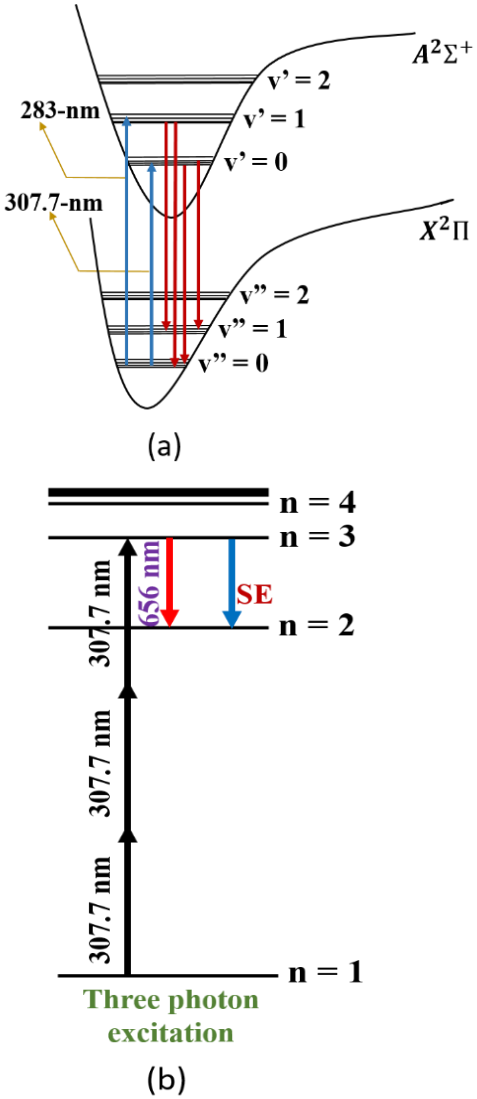

Figure 5.1: Energy level diagrams showing excitation and emission schemes for (a) OH-LIF, and (b) H-atom 3pLIF.

The background and different excitation schemes of H-atom and OH radicals have already been discussed in detail in Section 4.1 and Section 2.2.4 respectively.

Interestingly, the 3pLIF wavelength of H-atom overlaps with $X^2\Pi$ (v"=0) $\rightarrow$ $A^2\Sigma^+$ (v'= 0) transition of OH, paving the way for simultaneous excitation of H-atom and OH using a single broadband fs pulse. Figure 5.1 (a) shows the energy level diagram of OH depicting the excitation at λ = 307.7-nm of $X^2\Pi$ (v" = 0) $\rightarrow$ $A^2\Sigma^+$ (v' = 0) band. The fluorescence signal can be detected primarily from the v' = 0 $\rightarrow$ v" = 0 in the range of 305–320 nm. A weak emission in the 280–290 nm range can also be excited from the vibrationally excited v'=1 state. Figure 5.1 (b) shows the H energy level diagram depicting the 3-photon excitation scheme of n =1$\rightarrow\rightarrow\rightarrow$n=3 at λ = 307.7 nm. Fluorescence can be detected from the n =3$\rightarrow$ n=2 decay at 656 nm. In the present study, we use a single broadband fs laser pulse centered near 307.7 nm for simultaneous excitation-detection of H and OH in flames. Measurements were performed in a range of near-adiabatic flames stabilized over the Hencken calibration burner, and subsequent fluorescence imaging is presented in a premixed Bunsen jet flame. The experimental details and the results are discussed in the subsequent sections.

5.2 Related Instrumentation for OH Imaging

Figure 5.2 shows the schematic of the experimental apparatus used for the simultaneous detection of H-atom and OH in laboratory flames. The 1-kHz-repetition-rate, 800-nm-wavelength pump beam was generated using an amplified Ti: Sapphire laser (Spectra Physics Model: Solstice Ace). The peak pulse energy was 6mJ/pulse with approximately 80-fs pulse width. The pump beam was then passed through a series of parametric conversion, frequency-doubling and mixing stages inside an optical parametric

amplifier (OPA) to generate an output of λ=307.7 nm with maximum pulse energy of 40 μJ/pulse.

The collimated beam λ =307.7-nm output beam was focused using an f = +1000-mm converging lens (Lattice Electro Optics, Part No. # UF-PX-25.4-1000), and passed through the center of the CH_4/air and C_2H_4/air flames established over a 25.4-mm x 25.4-mm a Hencken calibration burner. The flame equivalence ratio (Φ) was varied from 0.7–1.6 and a 20-slpm dry air was used as shroud to stabilize the flame. Subsequently, simultaneous line images of H-atom and OH were obtained by focusing the beam onto a premixed $CH_4/O_2/N_2$ flame stabilized on a Bunsen jet flame burner having an exit diameter of 4 mm. In this flame, Φ was set at either 1.0 (CH_4: 0.3 slpm, O_2: 0.6 slpm, and N_2: 1.7 slpm) or 1.35 (CH_4: 0.4 slpm, O_2: 0.6 slpm, and N_2: 1.7 slpm). A dry air shroud flow of 10 slpm flown through a 50-mm diameter annular honeycomb was used for flame stabilization. The height above the burner (HAB) was varied from 0 to 15-mm by mounting the burners on a vertical translation stage. For 2D imaging, a laser sheet was generated using a telescopic lens combination of concave cylindrical lens (f = -75 mm) and a converging spherical lens (f = +100-mm).

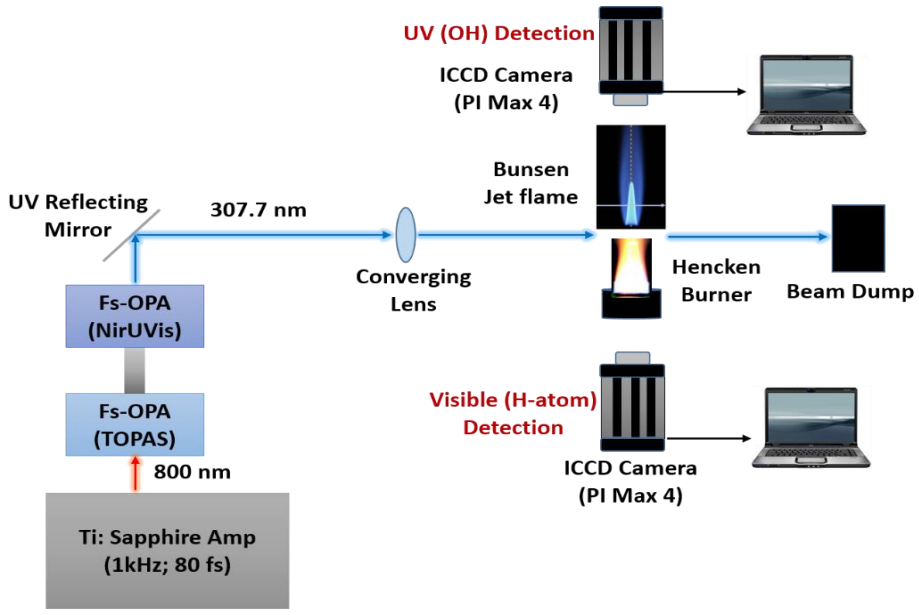

Figure 5.2: Schematic representing the experimental apparatus.

Initially, the fluorescence signal spectrum from OH was recorded using a spectrometer (Princeton Instruments Model: Isoplane SCT320) with 1200 lines/mm grating, and the integrated signal in the range of 310–320 nm is used as the OH LIF signal. However, for simultaneous detection of H and OH, two visible and UV grade intensified CCDs (ICCD) cameras (Princeton Instruments; Model: PIMAX4) were used. The ICCD cameras were placed orthogonally to the direction of laser beam on either side of the flame. The typical ICCD gate width was 100 ns and the gain was set at 100%. In order to avoid spectral interferences, a 656 ± 3 nm filter (Andover Corporation, Part number #: 656FS03-25), and a 285 ± 7.5 nm filter (Semrock; Part #: FF01-285/14-25) were placed in front of the camera lens for capturing H and OH images respectively. During all experiments, the backgrounds were recorded separately by blocking the excitation laser beam, and subtracted off from the signals.

5.3 Results and Discussion

Figure 5.3 shows the variation of the recorded LIF signal of H-atom and OH as a function of excitation wavelength in CH_4/air flame stabilized over the Hencken burner. Also shown are the simulated OH spectra using the LIFBASE software package as well as the recorded laser spectral profile at the peak H-atom location. The excitation laser pulse having a bandwidth of approximately 2-nm full-width at half maximum (FWHM) was scanned across the entire excitation wavelength range.

Subsequently, the laser wavelength was fixed at λ = 307.7-nm in order to excite H-atom and OH as per the energy level diagram shown in Figure 5.1. All the measurements were recorded at HAB of 10-mm. Each 3pLIF H-atom data set is an average of 30 spectra, each containing 800 on-CCD accumulations. Each OH data point is an average of 30 spectra and 100 on-CCD accumulations were used. The uncertainties in both the cases were calculated as the standard deviation over 30 individual frames. It can be observed from the Figure 5.3 that the 3pLIF profile of H-atom matched well with that of the laser beam, indicating narrowband H atomic line convoluted with spectrum of the broadband fs laser. A good agreement is also obtained between experimental and low-resolution simulated OH excitation spectrum. An important inference which can be derived from the Figure 5.3 is that the peak intensity location of 3pLIF spectrum of H-atom and the first peak of OH LIF spectrum show a good overlap near λ = 307.7-nm indicating simultaneous excitation-detection of H-atom and OH can be performed using a single broadband fs pulse.

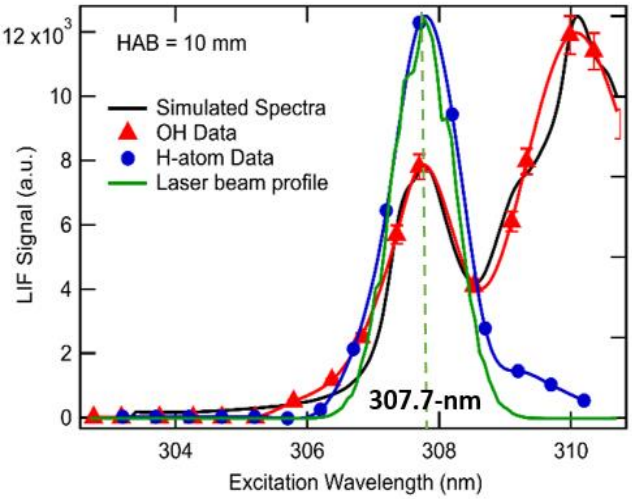

Figure 5.3: OH and H excitation scan along with laser beam profile and OH simulated spectra.

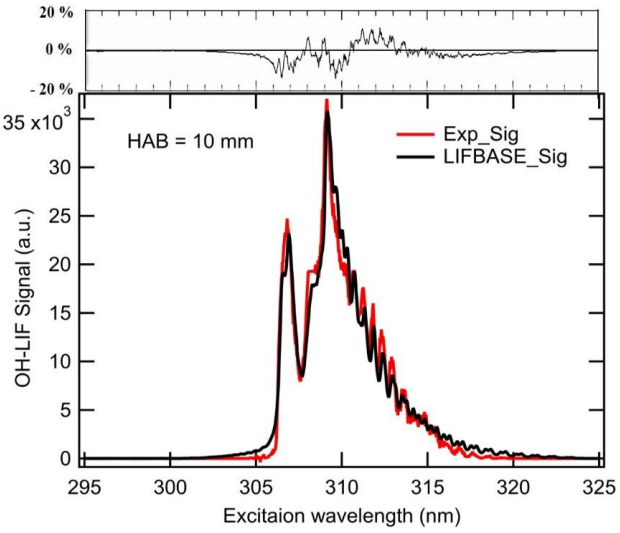

Figure 5.4: Experimental and calculated OH emission spectra from the v'=0 → v" = 0 band of OH. The root mean square error is shown on the top.

Shown in Figure 5.4 are the high-resolution experimental and simulated OH emission spectrum from v' = 0 → v" = 0 vibrational manifold of $A^2\Sigma^+ \rightarrow X^2\Pi$ electronic transition. The simulated spectrum was calculated at the adiabatic flame temperature of

Φ=1.0 CH_4/air flame (2236 K) and at 1-atm pressure. The experimental emission spectrum was obtained using the 1200 lines/mm grating. The root-mean-square error between the simulated and experimental spectra are shown at the top of the figure.

The two emission peaks are observed near λ=307-nm and λ=310-nm. However, as mentioned above, the OH LIF signal reported in Figure 5.3 and for all subsequent measurments are the value of integrated OH emission signal in the range of 310–320 nm in order to avoid the scattering interference from the 307.7-nm excitation laser. Furthermore, during the same excitation process, v' = 1 → v" = 0 emission between 280–295-nm from the vibrationally populated v' =1 level could also be observed, although that intensity is ~ 30 times weaker compared to v' = 0 → v" = 0 emission.

Shown in Figure 5.5 is the variation of OH LIF and H-atom 3pLIF signal intensity as a function of laser pulse energy obtained at HAB=10-mm location in the Φ =1.0 CH_4/air flame established over the Hencken burner. The pulse energy was varied by a inserting a variable neutral density filter in the path of the laser beam. Each data point is an average of 30 measurements over 800 and 100 on-CCD accumulations for H and OH respectively. Error bars were evaluated as 5% of the base value of each data point. For unsaturated regime, the LIF signal intensity is given by $Sig_{LIF} \propto I^n$, where, I = laser intensity, n = number of photons involved in the excitation transition. Accordingly, n=1 dependence for OH LIF was observed for the entire range of laser energies whereas and n=3 dependence was observed for 3pLIF of H for laser pulse energy below 30 μJ/pulse. The deviation from cubic dependence at higher laser pulse energies can be attributed to plasma

generation at the focal point of the beam as well as interferences caused by the photo-dissociation of other H containing species in the flame at higher laser energies [135].

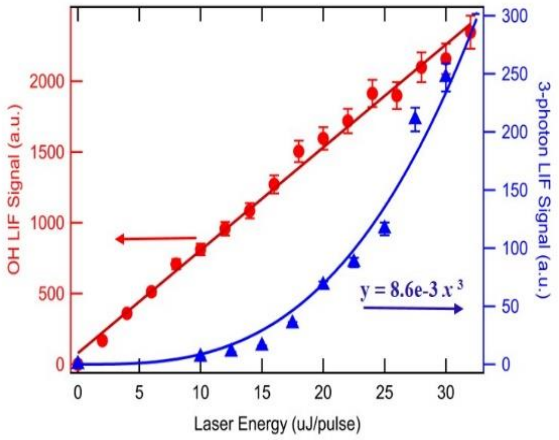

Figure 5.5: Variation of OH LIF and H-atom 3pLIF signal as a function of laser pulse energy.

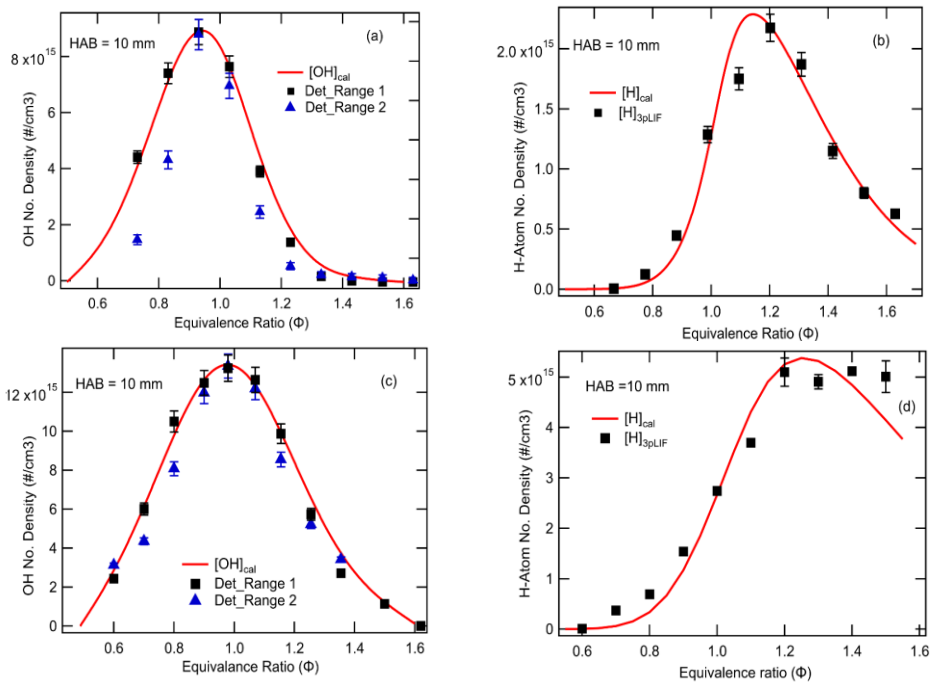

Figure 5.6: (a) and (c) OH number density in CH_4/Air and C_2H_4/Air flame respectively; (b) and (d) H-atom number density in CH_4/Air and C_2H_4/Air flame respectively along with calculated equilibrium values.

Subsequently, OH signals were recorded on the spectrometer in a series of CH_4 /air flames stabilized over the Hencken calibration burner at 10-mm HAB location. Figure 5.6(a) and (b) show the variation of OH and H-atom number density respectively, as a function of Φ ranging from lean (Φ = 0.6) to very rich (Φ = 1.6) flame conditions. In Figure 5.6(a), the spectrally integrated OH signals are shown for two ranges, namely 310–320 nm region corresponding to v'=0 $\rightarrow$ v"=0 emission (Range 1), and 278–292 nm region corresponding to v'=1 $\rightarrow$ v"=0 emission (Range 2). As mentioned earlier, the signal intensity in Range 2 was lower than in Range 1. The 3pLIF signal of H-atom recorded using direct imaging is shown in Figure 5.6(b). Each data set is an average of 30 spectra with 100 and 800 on-CCD accumulations for OH and H-atom, respectively.

The equilibrium OH and H-atom number densities calculated using CANTERA code are also shown in each figure. A good agreement was observed between experimental (Range 1) and numerically calculated OH profiles. The OH profile obtained using Range 2 is narrower than that from Range 1 as well as calculated profile, which can be due to the low signal-to-noise (S/N) in Range 2. As seen in Figure 5.6 (b), 3pLIF signal of H-atom matches well with the equilibrium calculations. Similarly, OH and H profiles were recorded in a series of C_2H_4/air flames and the results are shown in Figure 5.6 (c) and (d). The agreement between experimental and calculated OH profiles is improved compared to the CH_4/air case, which is expected to result for increased OH signal levels for both detection ranges. In Figure 5.6 (d), a good agreement of experimental and equilibrium values was observed for the lean and stoichiometric flames. However, a slight increase in the experimental H-atom signal levels is observed on the rich end beyond

Φ=1.4, which is attributed to interference from soot incandescence [119]. Recall, as seen in Figure 5.1, H-atom emissions are observed in the visible region (656-nm) whereas OH emission is constrained in the UV region of the spectrum. Since LII emissions are more prominent in the visible region of the spectrum, leakage soot interference can still be observed in rich flames [119].

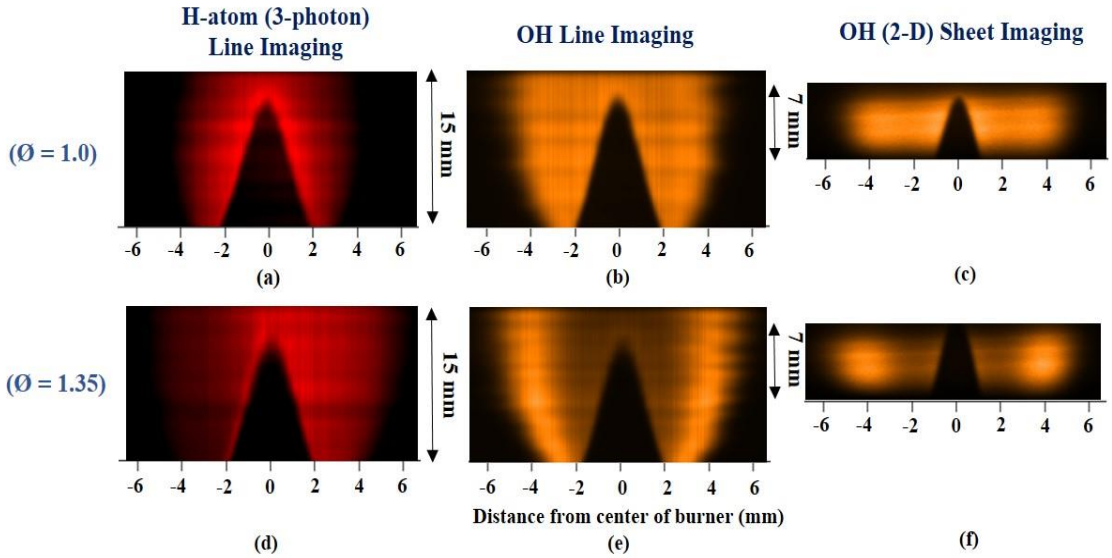

Figure 5.7: Vertically stacked LIF line profiles of H-atom and OH radical as a function ofΦ; (c) and (f) 2-D sheet imaging of OH as a function of Φ.

The major advantage of the present approach is the capability for simultaneous imaging of OH and H-atom using a single laser pulse. Although we could record single laser shot OH images using a laser sheet of approximately 7-mm high (shown in Figure 5.7 (c) and Figure 5.7 (f)), H-atom 3pLIF signals become indistinguishable because of the low H-atom concentration and weak 3p excitation efficiency. Hence, we recorded simultaneous line images of H-atom and OH by using a nearly collimated excitation laser beam focused through the f = +1000 mm spherical lens. Each line profile is an average of

30 frames with 800 and 100 on-CCD accumulations in H-atom and OH cameras respectively. For H-atom imaging, a 656 ± 3 nm band-pass filter was mounted in front of the ICCD camera. However, the OH fluorescence signal was recorded from the v' = 1 → v" = 0 emission band using 285 ± 7.5 nm filter. As described above, it is possible to obtain approximately factor of 35 more OH signal from the v' =0 → v" = 0 emission band, however that would require a custom-designed bandpass filter in the 310 –320 nm spectral range, which was not available during the present experiment. Therefore, single-shot 2D images could not be recorded for OH PLIF.

The simultaneous line images of H-atom and OH were recorded in the Φ = 1.0 premixed Bunsen jet flame while translating the burner vertically in steps of 0.1 mm. The line images are then combined to generate 2D H-atom and OH profiles which are shown in Figure 5.7 (a) & (b) respectively. As expected, the spatial distribution of both species is axisymmetric with respect to the vertical axis of the flame. No H-atom and OH signal was observed in central conical region where only cold premixed reactants (unburned fuel-air mixture) are present. A rapid increase in H-atom and OH concentrations is observed at the flame front, and the signals go to zero as marched radially outwards because of the combustion products mixing with the ambient air and cooling down rapidly. A secondary flame front can be clearly seen in the OH image (Figure 5.7 (d)) in the Φ=1.35 flame where excess fuels is reacting with outside air diffusing into the flame. A similar observation has been reported by Lucht et al. [46, 47].

5.4 Summary

Simultaneous detection of H-atom and OH was demonstrated using ultrashort fs-duration laser pulses in a range of CH_4/air and ethylene C_2H_4/air flames stabilized over a Hencken calibration burner and a Bunsen jet burner. H-atom has been detected using recently demonstrated fs 3pLIF technique at λ=307.7-nm excitation as opposed to the frequently used 2pLIF at λ = 205.1 nm. The 205.1-nm DUV laser pulses can be absorbed in practical combustion systems containing thick transmissive optical windows, a problem that can be alleviated to a greater extent by using 307.7-nm 3pLIF. In the present study, 3pLIF of H-atom and single-photon LIF of OH were achieved using a single 307.7-nm fs laser pulse. The observed fluorescence signals of H and OH follow linear and cubic laser energy dependencies, respectively. H-atom and OH number densities were recorded as a function of Φ in CH_4/air and C_2H_4/air flames established over the Hencken calibration burner. For H-atom, the experimental data are in good agreement with the equilibrium number density in CH_4/air and C_2H_4/air flames, although suspected interferences for soot incandescence can be seen for Φ >1.3 in the latter case. Furthermore, the experimental concentrations of OH obtained from v' = 0 $\rightarrow$ v" = 0 emission band integrated in the 310–320-nm wavelength range are in good agreement with calculated equilibrium number densities in CH_4/air and C_2H_4/air flames. Lastly, simultaneous H-atom and OH fluorescence line profiles are imaged simultaneously using two ICCD cameras for Φ = 1.0 and Φ = 1.35 in $CH_4/O_2/N_2$ Bunsen jet flames. Although it is possible to 2D images of OH under these conditions, low number density and reduced 3p excitation cross sections prohibit 2D imaging of H-atom under present conditions.

6. IMAGING APPLICATIONS OF DIRECT FREQUENCY CONVERSION SYSTEMS

The ultra-short optical pulses in the UV and VUV region are of significant interest for investigating ultrafast processes including temporal studies of photo-dissociating molecules and dynamic processes occurring on the metal surfaces at near Fermi levels. In combustion, high repetition rate fs pulses enable efficient non-linear excitation and potentially eliminates photolytic interferences (details have been discussed in the previous chapters).

However, ultra-short fs pulses generated by Ti: Sapphire oscillators mostly reside in the near-infrared (IR) region, which is of little significance. In order to implement these pulses for the potential applications listed above, the pulse frequency needs to be tuned to the UV/ VUV region. Unfortunately, the conversion of these IR pulses to UV is a highly inefficient process in terms of power and pulse duration. One of the most convenient ways to achieve this frequency conversion is to use the commercially available optical parametric amplifier (OPA) followed by frequency doubling and mixing stages. However, the conversion efficiencies of these commercial units are well below 1%, as a result of which, the output UV pulse energy is usually insufficient for high-temperature imaging applications such as 2pLIF of H-atom and N-atom. Therefore, in order to overcome these limitations, researchers have successfully demonstrated direct frequency conversion schemes to tune IR fs pulses using non-linear β-Barium-Borate (BBO) crystals.

The concept of direct frequency quadrupling was first demonstrated by Ringling et al. [136] in 1993. The researchers were able to obtain 180-fs VUV pulses in the range

of 189 nm to 200-nm. The maximum pulse energy of 2 μJ/pulse, 20-Hz repetition rate at 193-nm and 4 μJ/pulse, 1-kHz repetition rate at 200-nm was produced. Figure 6.1 shows the spectrum of 193-nm fs pulse with 50 on-CCD accumulated shots. The FWHM is around 0.4 nm for 100-fs pulse width. The smooth spectrum shows that there are no distortions in the pulse shape even after the fourth harmonic generation.

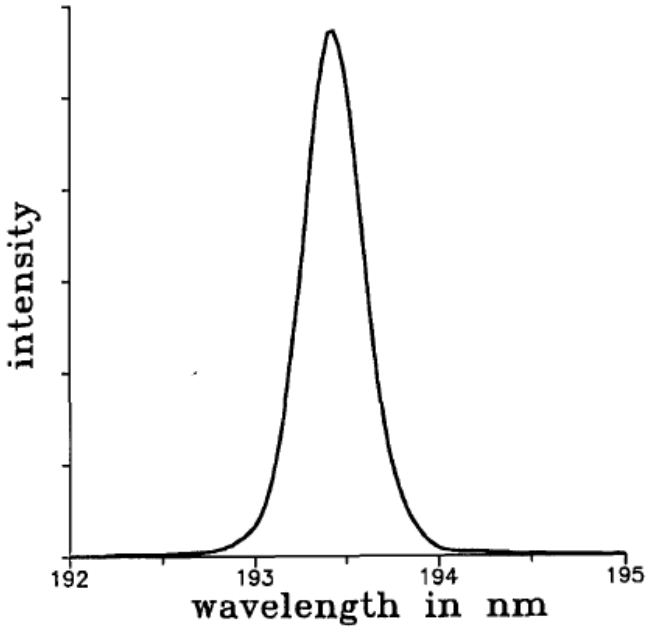

Figure 6.1: Spectrum of 193-nm fs pulses with FWHM = 0.4 nm reprinted from [136].

Further, Rotermund et al. [137] and Petrov et al. [138] demonstrated, for the first time, the generation of fourth harmonic fs pulses (at MHz repetition rate) from a mode-locked Ti: Sapphire laser. The authors reported maximum average power of 6 mW for 165 fs pulse width and 15 mW for 340-fs pulse width at 82 MHz.

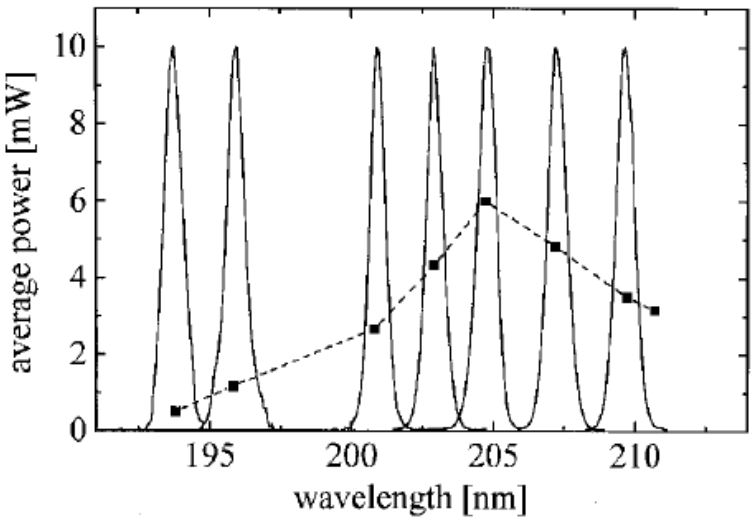

Figure 6.2: Spectra showing tunability at the FHG scheme with average power shown corresponding to each FHG wavelength reprinted from [137].

Figure 6.2 shows the tunability range of FH wavelengths using 0.1 mm thick FHG BBO crystal. The figure also shows the average power (marked with solid squares) corresponding to each wavelength. It was observed that the maximum FHG power was obtained at 205-nm, corresponding to the fundamental wavelength of 820-nm. Further, the lower pulse energies below 200-nm is a result of lower THG and FHG efficiency of the BBO crystals for wavelengths less than 200-nm.

6.1 Frequency Tripling and Quadrupling Stage

From the discussion so far, the need for direct frequency tuning of fs laser pulses is necessitated for direct imaging applications of minor species (H-atom, N-atom etc.) in different flames. Figure 6.3 shows the direct FHG setup used for generating UV and VUV wavelengths. The Ti: Sapphire amplifier can be tuned to generate a fundamental pump beam in the range of 750-850 nm at 1kHz repetition rate with a beam diameter of approximately 10 mm. However, the pump beam wavelength was set to 850-nm for OH

detection. The 10 mm diameter pump beam with pulse energy of 2.3 mJ/pulse was down collimated to ~ 4 mm by passing it through a telescopic combination of +200 mm focal length convex lens (Part # UF-PX-25.4-200-800, Lattice Electro Optics) and -70 mm focal length concave lens (Part # UF-PC-25.4-70-800, Lattice Electro Optics).

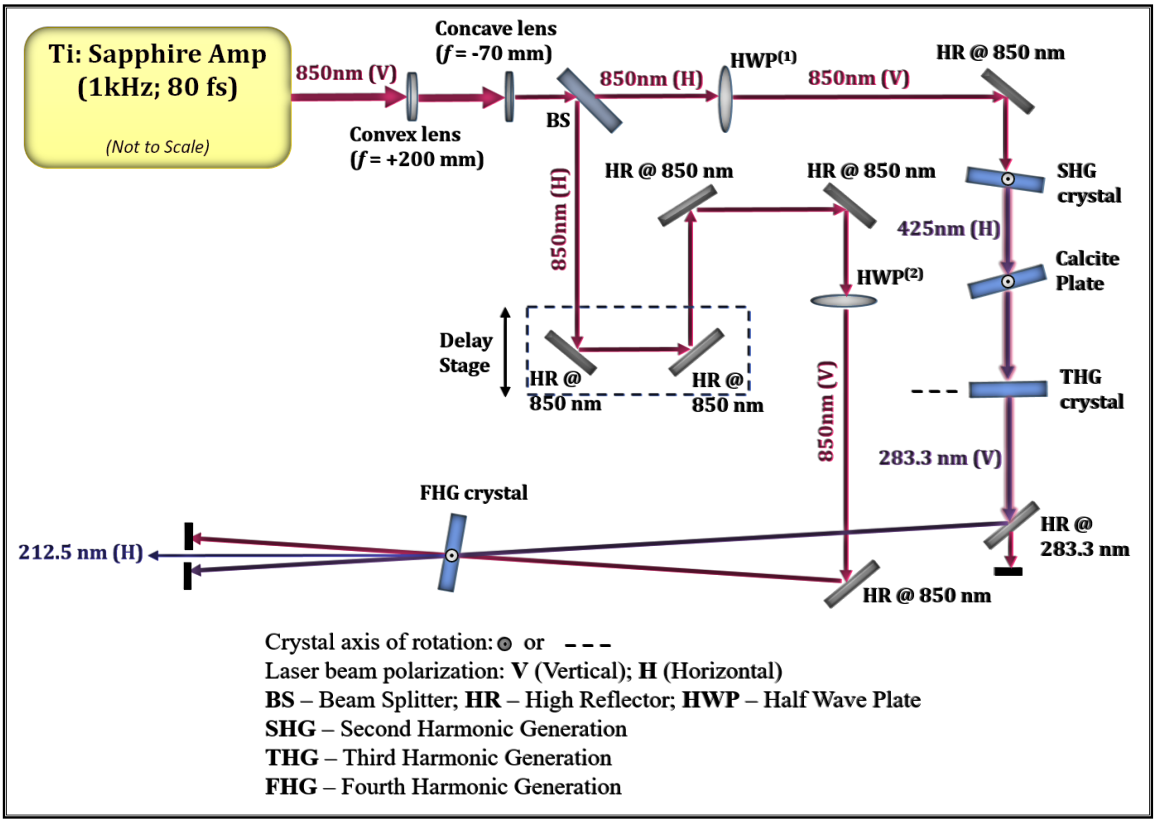

Figure 6.3: Schematic of direct THG and FHG setup.

Further, a 30/70 beam splitter (BS) (Part # FABS-800-840-Rp30-45-UF-1006, Lattice Electro Optics) was used to split the pump beam in order to send 30% of the fundamental pump energy to the delay stage. However, the polarization got changed when the beam passes through the beam splitter and thus a half-wave plates ($HWP^{(1)}$ and

HWP$^{(2)}$) (Part # CWO-800-02-08-R10; Lattice Electro Optics) were introduced in the beam path to change the polarization back to original (V).

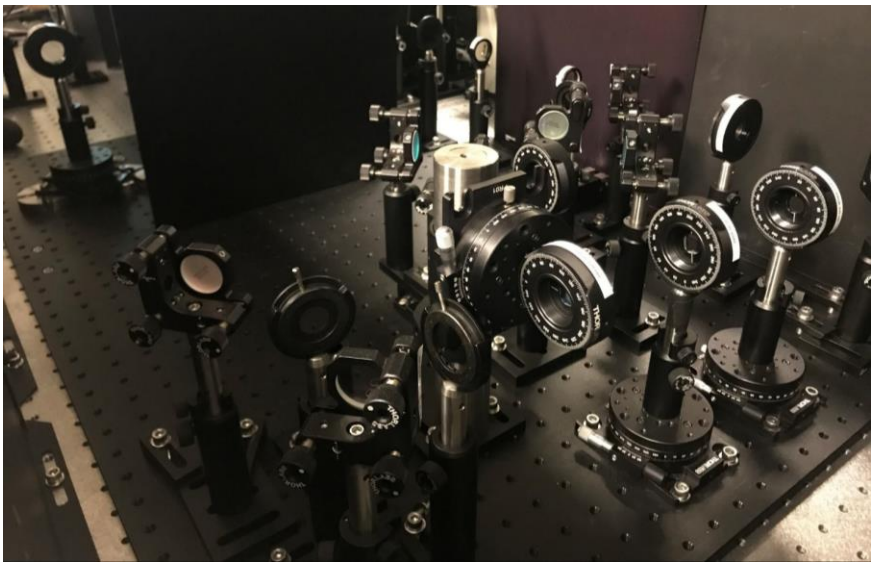

(a)

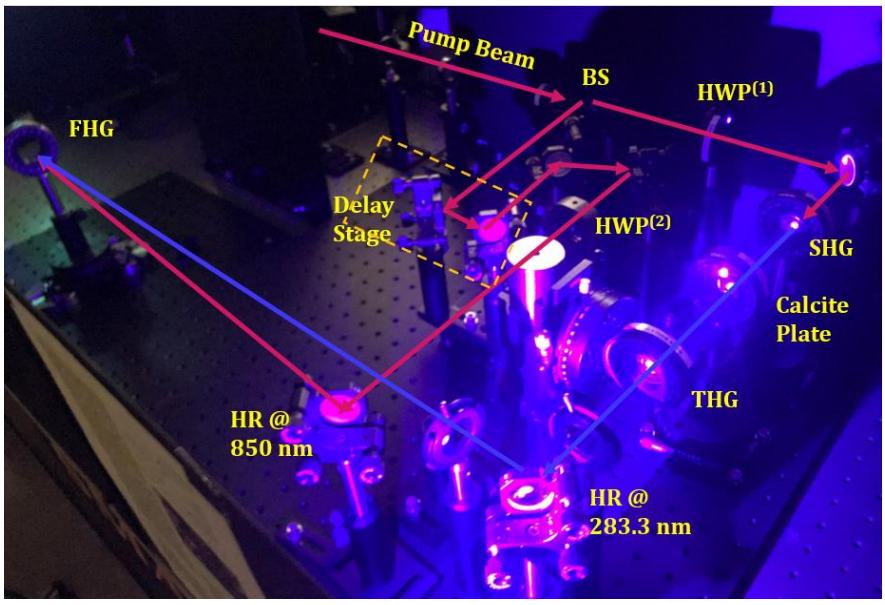

(b)

Figure 6.4: Digital image of the FHG setup (a) non-working condition (b) working condition.

Further, the beam reflecting from 850-nm high reflection (HR) mirror (Part # BB1-E03-750-1100 nm, Thor Labs) was allowed to pass through the series of BBO crystals starting from SHG crystal (Part # BTC12100-SHG820(I)-AR; 12.7 x 12.7 x 1.0 mm; phase-matching angle $\theta = 28.5^{\circ}$; Newlight Photonics), calcite crystal (Part # CAL12330-AR820/410; 12.7 x 12.7 x 3.3 mm; Newlight Photonics) and finally THG crystal (Part # BTC12100-THG820(II)-AR; 12.7 x 12.7 x 1.0 mm; phase-matching angle $\theta = 53.5^{\circ}$; Newlight Photonics). The calcite plate was introduced to compensate for the delay between SHG and THG processes. Thus, after passing through THG crystal, the fundamental IR pump beam gets converted to 283.3 nm UV beam. It should be noted that since the conversion efficiency of these BBO crystals is not 100%, some part of the fundamental beam still remains unconverted and thus, a 283-nm HR mirror (Part # WRX-280-315-45-UF-1025; Lattice Electro Optics) was used after THG crystal to reflect only the UV beam. The pump beam transmits through the 283-nm HR mirror and gets blocked by a beam dump as shown in the schematic.

The delay stage (linear accuracy ~ 1μm) controls the temporal overlap of the pump beam (passing through the delay stage) and the THG beam. These two beams were made to spatially overlap (crossing angle ~ 2-3 degrees) at the BBO FHG crystal (Part # BTC12040-FHG820(I)-P, 12.7 x 12.7 x 0.4 mm, phase matching angle $\theta = 61.4^{\circ}$; Newlight Photonics), thereby resulting in a non-linear overlap and generation of 212.5 nm wavelength UV beam. The 850-nm and 283-nm beam also passes through the FHG crystal and gets blocked by the beam dump. It should be noted that this entire setup was assembled

on a 24" x 24" breadboard and is thus, portable and can be used with any other laser system as well.

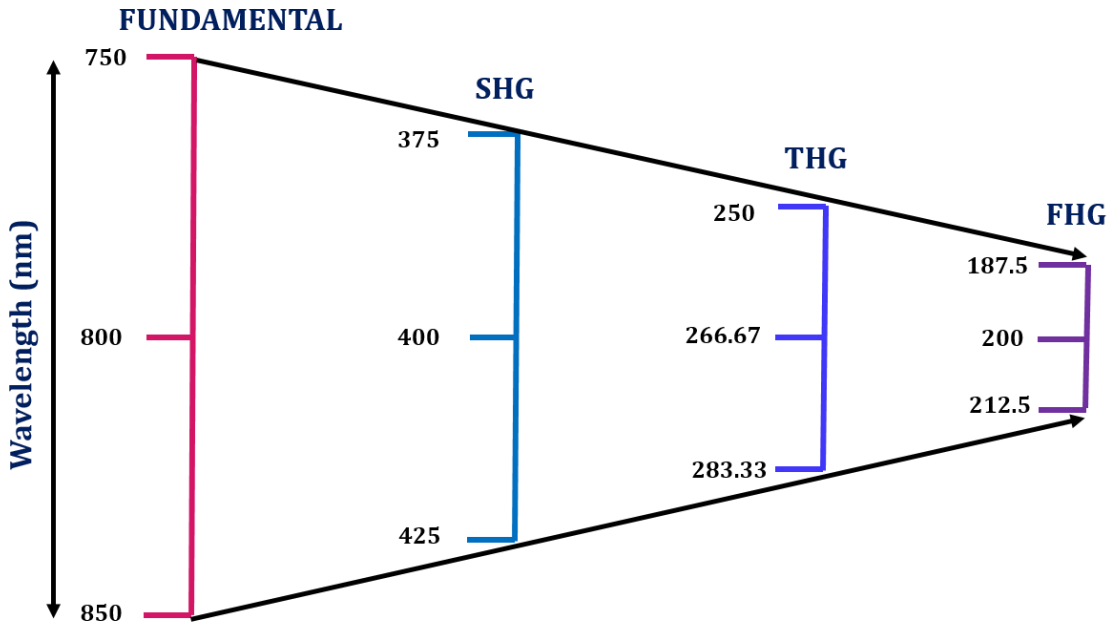

Figure 6.5: Complete wavelength tuning range of the direct frequency tuning apparatus.

Figure 6.5 shows the complete wavelength range covered by direct frequency tuning setup. As mentioned before, the fundamental pump beam from the Ti: Sapphire laser can be tuned from 750-850 nm and thus, SHG can be obtained from 375-425 nm. The corresponding wavelength range for THG is from 250-284 nm. More importantly, the tuning range for FHG wavelengths are from 190-212 nm with an average laser pulse energy of ~ 35 μJ/pulse for input pump beam energy of 2.0 mJ/pulse. However, it should be noted that electron excitation using wavelengths below/around 200-nm is very challenging because of the absorption of the laser by the air molecules near those VUV wavelengths. An application of the 200.6-nm excitation wavelength for O-atom detection has been discussed in Section 6.3.

6.2 Hydroxyl Radical Imaging in Turbulent Diffusion Flames

Figure 6.6 shows the schematic of the experimental apparatus used for the detection of OH in CH_4/H_2 diffusion turbulent flames.

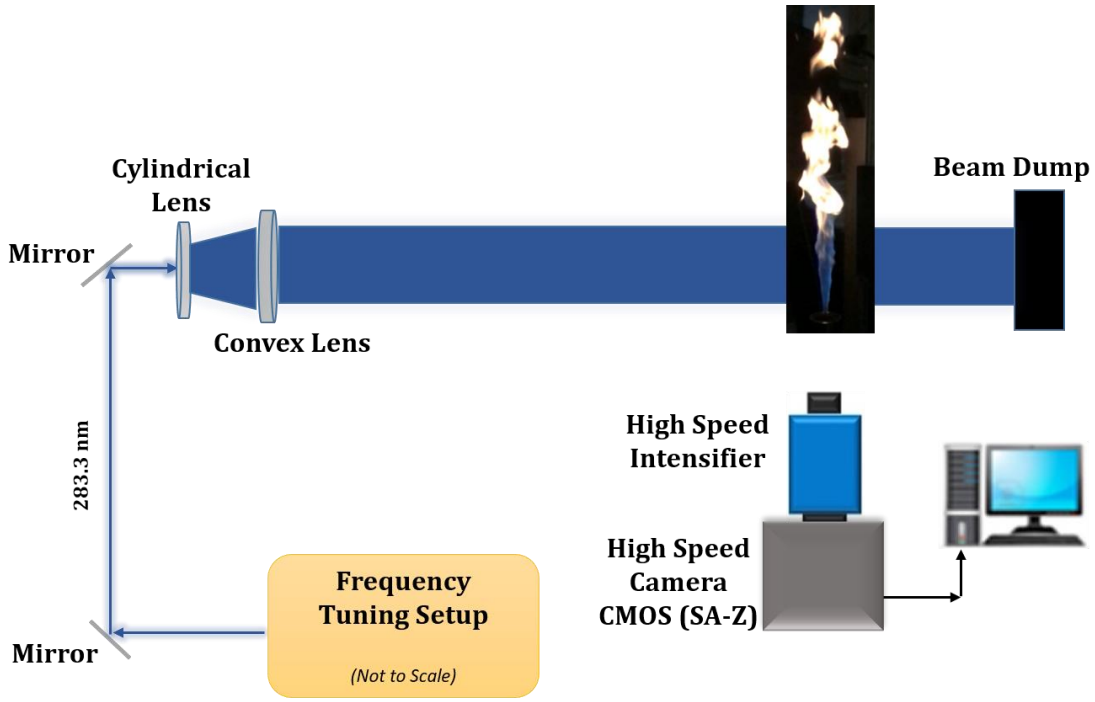

Figure 6.6: Schematic of the experimental apparatus.

The UV excitation wavelength used for the detection of OH was centered at 283-nm. This THG beam can be obtained from the frequency tuning apparatus (explained in Section 6.1) by blocking the part of the fundamental pump beam going through the delay stage after the pump beam passes through the BS. Therefore, by removing the FHG crystal (from its location as shown in Figure 6.3), the output beam coming of the frequency tuning setup will be a ~ 5mm diameter, THG, near-gaussian beam centered at 283-nm with a pulse energy of 90 μJ/pulse. A telescopic arrangement of -25 mm focal length, plano-

concave cylindrical lens (Part # LK 4767; Thor Labs) and +300 mm focal length convex lens (Part # UF-PX-25.4-300; Thor Labs) were used to generate a laser sheet of approximately 50 mm height and approximately 0.5mm thickness. The central portion of the sheet (~ 45 mm height) was made to pass through the diffusion H_2/air flame established on the Hencken burner and a turbulent diffusion CH_4/H_2 flame established over the jet burner. The details of the flame flow rate and burner setup have been discussed later in this chapter. The 283-nm UV beam was used to excite $Q_1(5)$ rotational transition of the OH $A^2\Sigma^+$-$X^2\prod$ (1,0), followed by (0,0) and (1,1) fluorescence imaging through a 315±15-nm bandpass filter. Fluorescence images were recorded using a high-speed ICCD camera (for calibration purposes) and a high-speed complementary metal-oxide-semiconductor (CMOS) camera coupled with an UV high-speed image-relay optics (IRO) intensifier. The details of this apparatus have been discussed later in the chapter.

The spectra shown in Figure 6.7 were obtained using a fiber-coupled spectrometer (Model: Flame S; Ocean Optics). The spectra have been integrated over a time frame of 100 milliseconds and is an average of 10 scans. Figure 6.7 (a) represents the spectrum of the fundamental laser beam (output of the Ti: Sapphire amplifier) centered at 850-nm. It can be observed that the beam profile is not exactly Gaussian. This is primarily due to the fact that the tuning range of the amplifier is from 750-850 nm, thus, when the amplifier is set to operate at 850-nm, the gain-pulling effect slightly dominates and the resulting beam profile looks like the one shown in the figure. The FWHM of the fundamental beam is around 20 nm. Further, Figure 6.7(b) represents the spectrum of the fs-THG beam centered at around 283.3-nm. The FWHM of the THG pulse is around 4-nm. The Gaussian profile

of the THG beam is a good indicator of the efficiency of the direct frequency tuning and thereby, justifying the reliability of the process.

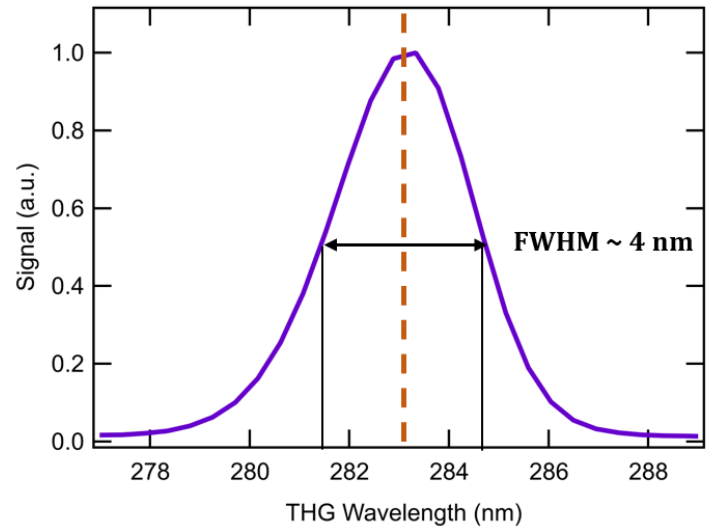

(a)

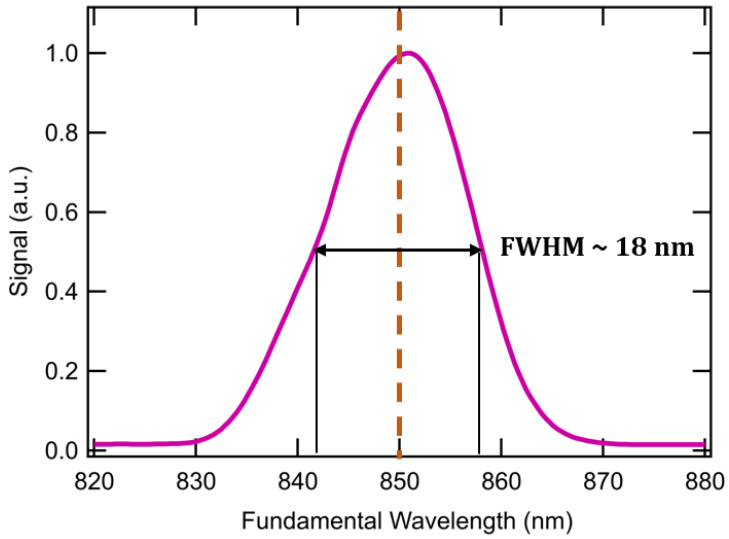

(b)

Figure 6.7: Spectrum of the (a) fundamental beam and (b) THG beam.

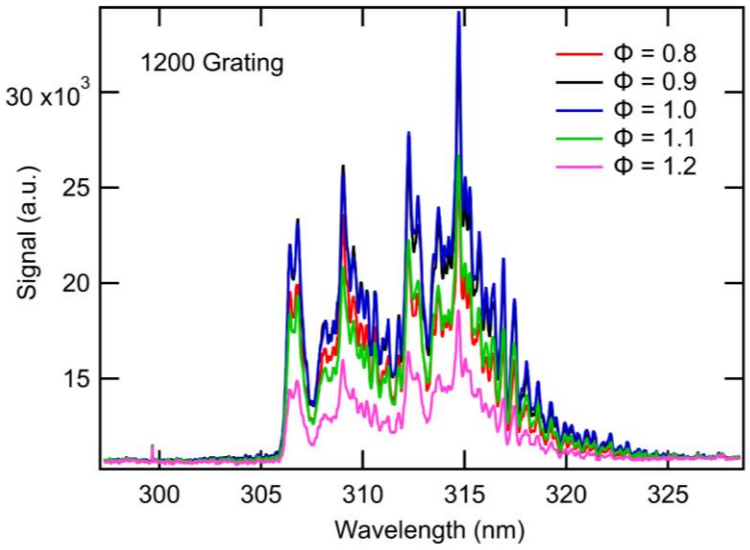

(a)

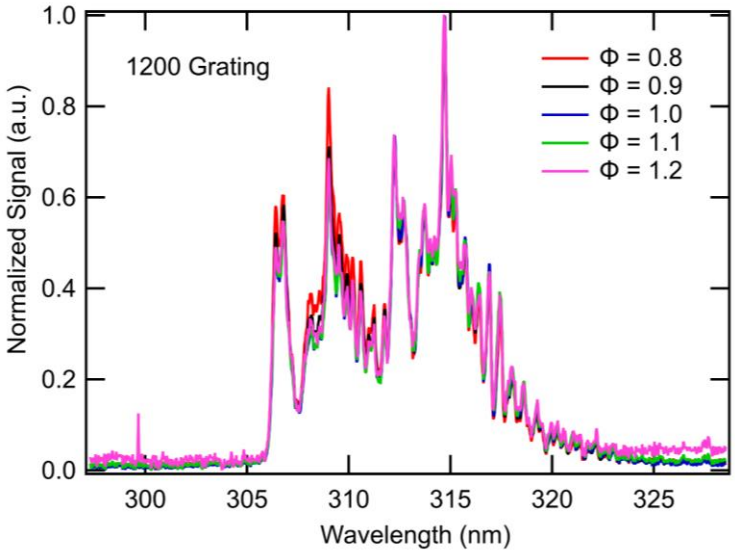

(b)

Figure 6.8: (a) Regular (b) Normalized OH-PLIF spectra recorded using 1200 lines/mm grating for different equivalence ratios.

Figure 6.8 (a) and (b) shows the OH-PLIF spectrum obtained using 1200 lines/mm grating corresponding to the (0,0) and (1,1) fluorescence emission resulting from the

excitation of mainly $Q_1(5)$, $Q_1(7)$ and $Q_1(9)$ lines in OH using the fs THG beam centered at 283.3-nm.

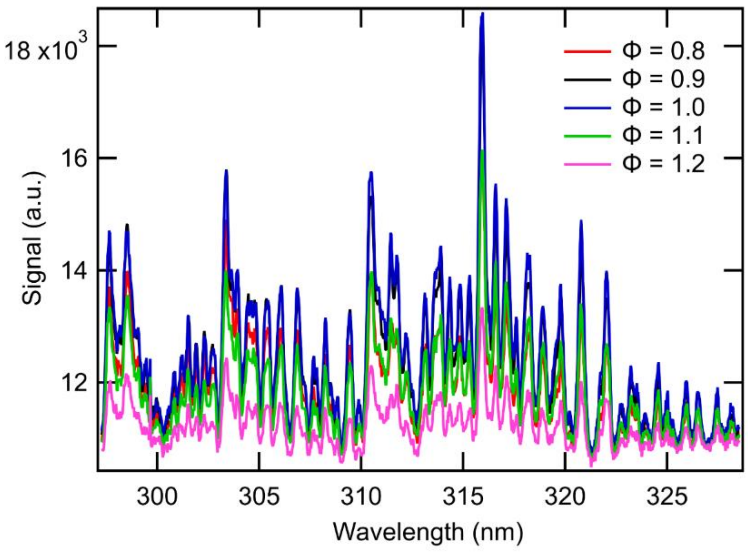

(a)

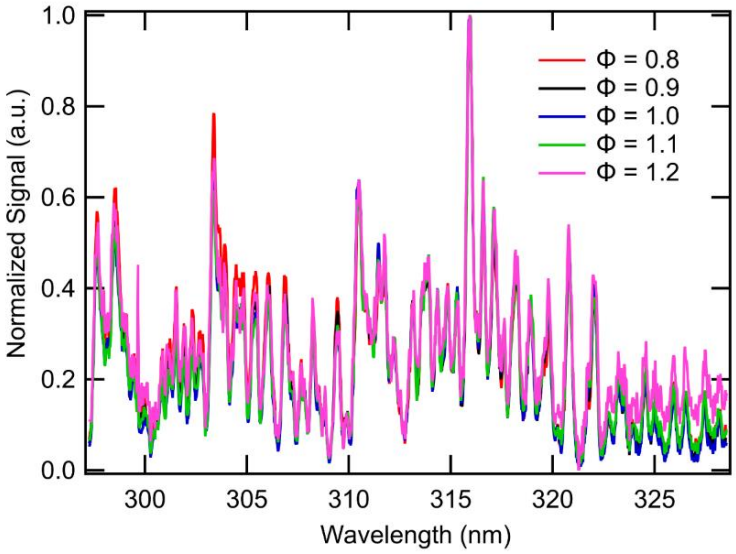

(b)

Figure 6.9: (a) Regular (b) Normalized OH-PLIF spectra recorded using 2400 lines/mm grating for different equivalence ratios.

Figure 6.9 (a) and (b) represents the OH-PLIF spectrum obtained for the similar conditions as that of Figure 6.8 but at a higher resolution grating of 2400 lines/mm. The spectra were recorded for a series of C_2H_4/air flames established over a Hencken calibration burner at different equivalence ratios ranging from lean ($\Phi = 0.8$) to rich ($\Phi = 1.2$). Each spectral line is an average of 50 frames, each with 600 laser shot on-CCD accumulations. The fluorescence emission was captured using a collimator placed orthogonal to the beam (passing 10-mm above the burner surface). A fiber optic cable was used to transmit the fluorescence emission from the collimator to the entrance slit (slit width = 100 μm) of the spectrometer (Model: IsoPlane 320; Princeton Instruments) coupled with an ICCD camera (Model: PIMax4; Princeton Instruments). The typical ICCD gate width was 50 ns and the gain was set at 100%. Further, out of the three gratings installed in the spectrometer (150 lines/mm low-resolution grating, 1200 lines/mm medium resolution grating and 2400 lines/mm high-resolution grating), 1200 lines/mm and 2400 lines/mm grating were used to record the spectra shown in Figure 6.8 and Figure 6.9 respectively. Moreover, before characterizing the spectra, the spectrometer was calibrated for wavelength correction using standard LED light source based Hg and Ne-Ar calibration lamps (Model: IntelliCal; Princeton Instruments).

It can be observed from the spectra represented in Figure 6.8 (a) and Figure 6.9 (a) that the maximum signal strength was obtained at the stoichiometric condition ($\Phi = 1.0$), however, very weak signal intensity was observed at $\Phi = 1.2$. The variation of equilibrium temperature at different Φ, resulted in different OH signal intensity in the flame zone. Further, peak-normalized OH-PLIF spectra at 1200 lines/mm and 2400 lines/mm grating

have been represented in Figure 6.8 (b) and Figure 6.9 (b) respectively. An excellent overlap of the spectral profiles at different Φ can be observed indicating negligible spectral interferences even in the richer flames. However, slight aberrations can be observed at Φ = 1.2 for the spectral range higher than 322 nm. These might be because of normalization at low signal to noise (S/N) ratio in richer flames. These results represent the advantages of excitation using broadband fs laser pulses as compared to the traditionally used ns pulses.

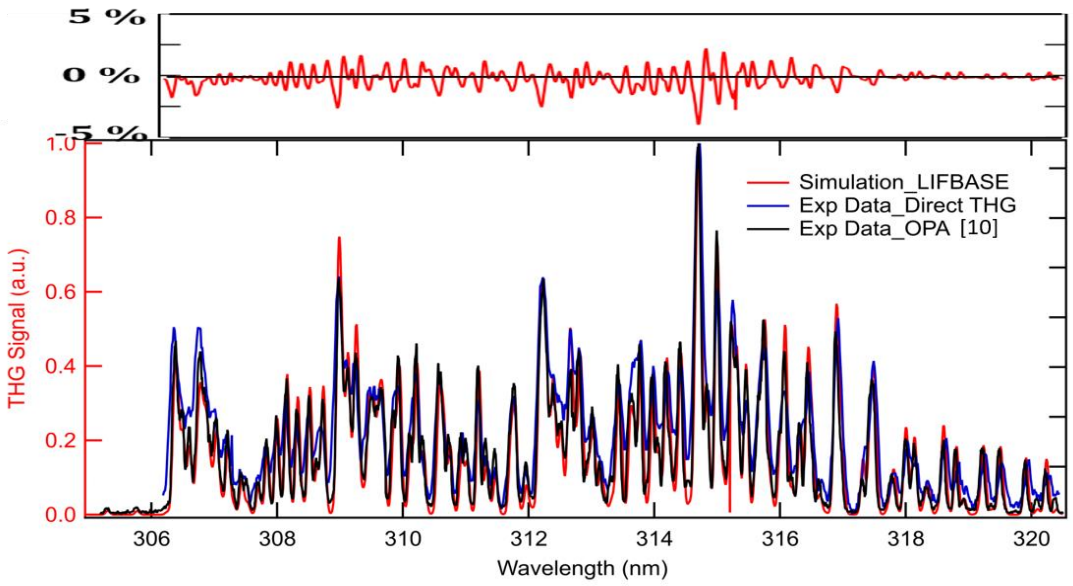

Figure 6.10: Comparison of OH-PLIF spectra obtained using THG with the simulated spectra obtained using LIFBASE and the spectra obtained using 283-nm generated from OPA.

An analogy of the OH-PLIF spectra, recorded using 2400 lines/mm grating, for (0,0) and (1,0) fluorescence emission in the C_2H_4/air flame is shown in Figure 6.10. The OH-PLIF spectra recorded using the THG beam (output of the direct frequency tuning setup) has been compared with the experimental data obtained using 283-nm beam

generated using commercial OPA [55] and with simulated spectra obtained using LIFBASE software package. The root-mean-square error (in the range of 306-nm – 321-nm) between the simulated and experimental THG spectra are shown at the top of the figure. The simulated spectrum was rotationally thermalized at 2200 K and is not vibrationally thermalized. An excellent overlap of the detailed rovibrational spectra obtained using different techniques suggests that direct frequency tuning method works as good as commercial OPA for UV excitation of different species. Further, it should be noted that collisional quenching can result in broadening and shifting of narrowband ns pulses, thereby, reducing the efficiency of the excitation scheme. However, the broadening effect have been observed to be minimal in case of ultrashort fs laser pulses. Therefore, fs laser pulses can be effectively used for diagnostics at elevated pressures.

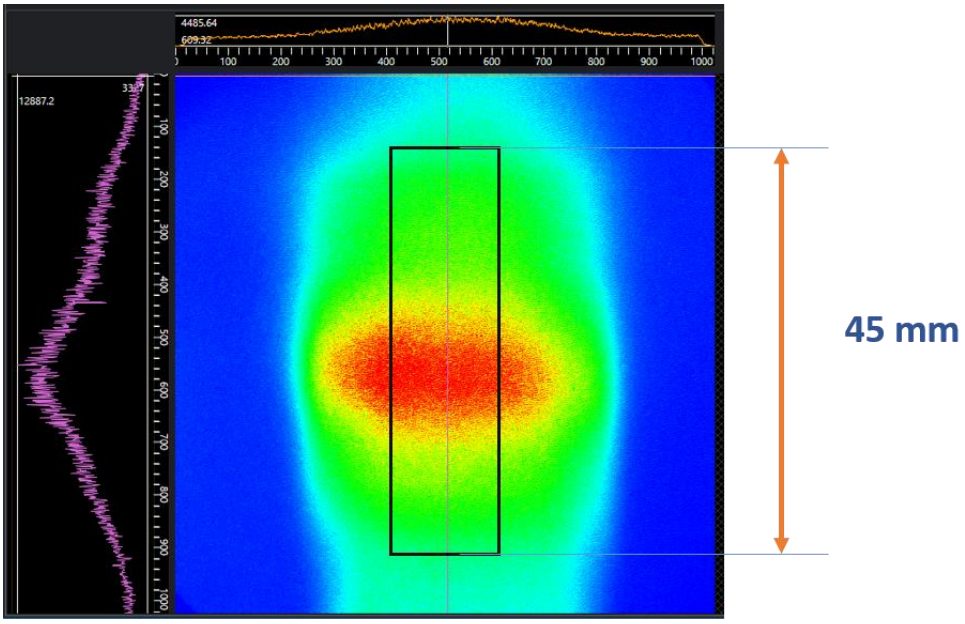

Figure 6.11: Laser sheet beam profile.

Figure 6.11 represents the beam sheet profile used to detect 2-D OH images in uniform H_2/air flame (Φ = 1.0) established over the Hencken calibration burner. The variation of the signal along the vertical axis (shown on the left in purple color) represents the near-Gaussian profile. The signal was averaged in the uniform region (represented by a rectangle) along the horizontal axis to get the vertical beam profile. The height of the laser sheet is marked in the figure as ~ 45 mm. The beam profile will be used to correct for the variations arising due to uncertainties in the intensity along with the height of the laser sheet for the images shown in Figure 6.13.

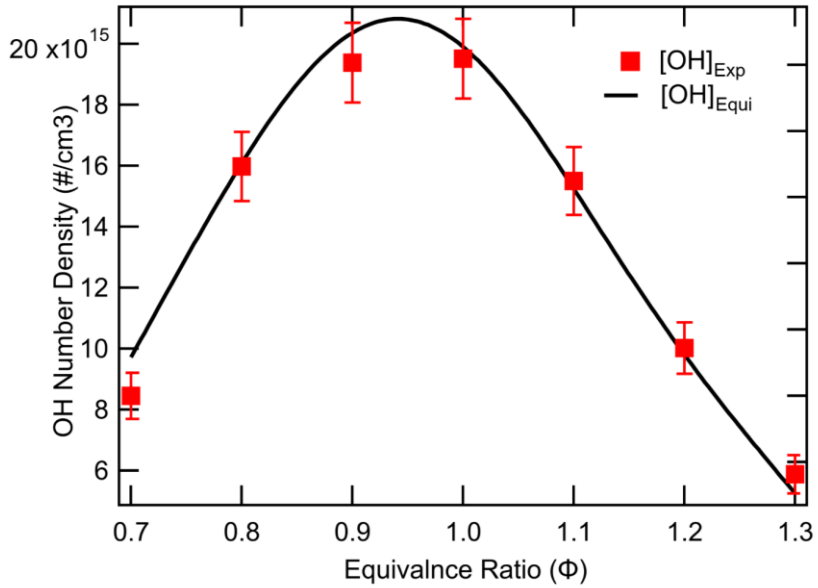

Figure 6.12: Variation of OH number density as a function of Φ in H_2/air flame.

Figure 6.12 shows the variation of OH number density as a function of Φ in H_2/air flame established over a Hencken calibration burner. The Φ was varied from 0.7 - 1.3 by keeping the air flow rate constant at 52 slpm and varying the H_2 flow rate from 15-28 slpm. Each experimental data point is an average of 25 frames and 100 on-CCD laser accumulations recorded at 100% gain and 50 ns gate width.

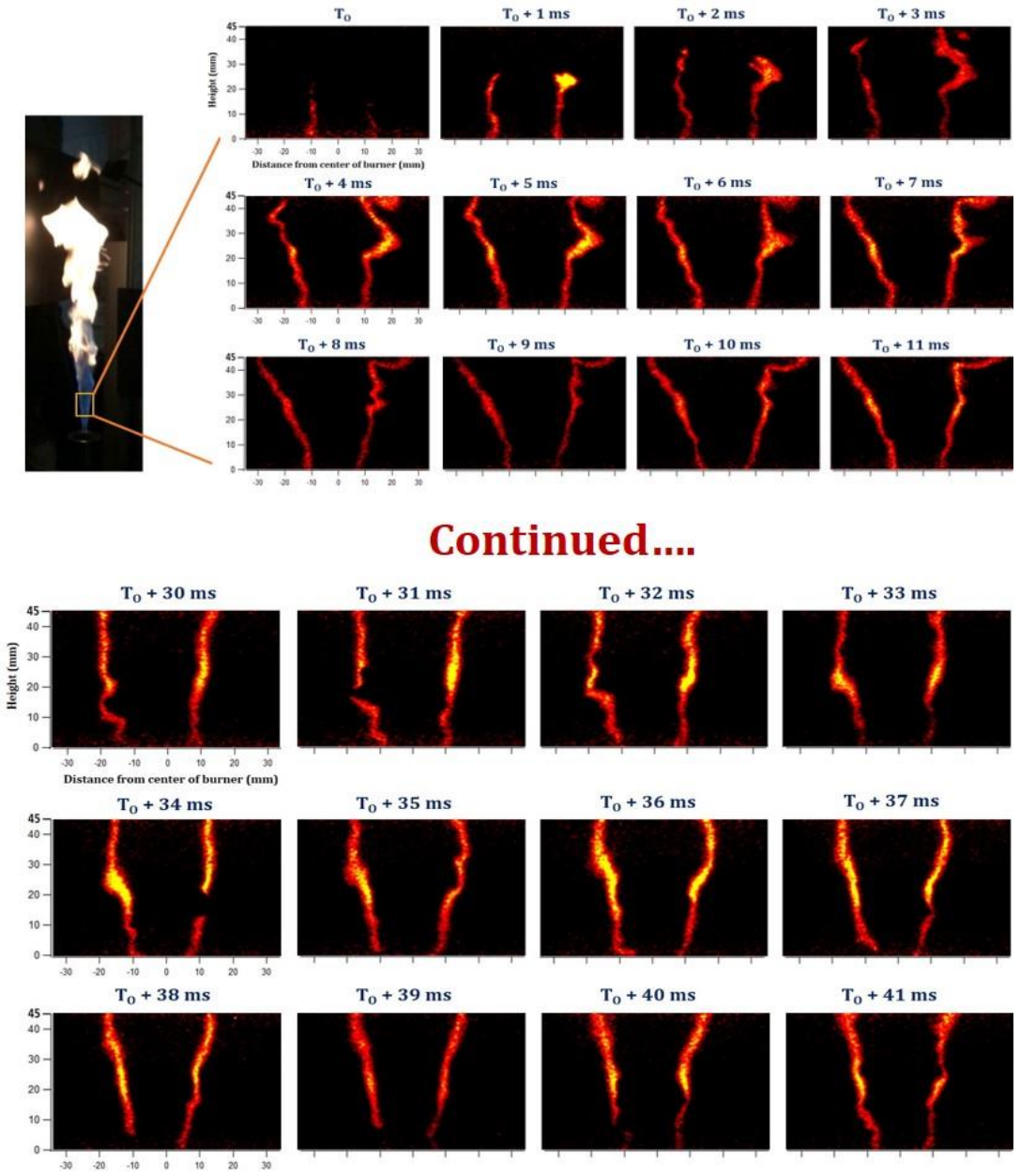

Figure 6.13: Consequent single-laser-shot OH-PLIF images at 1 kHz repetition rate demonstrating the flame development and dynamic flame structure in the CH_4/H_2 diffusion flame.

The uncertainty has been estimated as the standard deviation over the individual frames. It can be observed from the figure that experimental data is in good agreement

with the numerical OH number density obtained from CANTERA equilibrium code. Further, OH number density increased with increasing Φ up to Φ = 1.0 and then showed a monotonous decrement afterward. The maximum OH concentration was observed in the stoichiometric flame. Further, a slight deviation from numerical calculations can be observed in the lean flame. This is due to the heat loss to the burner surface and CANTERA calculations neglect the heat transfer effects.

Figure 6.13 represents consecutive 2-D OHPLIF images recorded in CH_4/H_2 (1:1) turbulent diffusion jet flames established over the Bunsen jet burner. The combined total flow rate of CH_4 and H_2 was 24 slpm (Reynolds Number ~ 3000) flowing through the central tube of diameter ~ 4.5 mm. A guard flow of dry air (50 slpm flow rate) was maintained through the annular region having a diameter of 50.8 mm. Further, the images were recorded using a high-speed CMOS camera (Model: SA-Z; Photron) (operating at 1kHz frame rate) coupled with a high-speed UV intensifier (Model: HS-IRO; LaVision) operating at 70% gain and 50-ns gate width. A 50-mm focal length, *f*/1.8 UV lens coupled with a 315 ± 10 nm bandpass filter was used to capture the OH fluorescence.

The first set of images in the figure (shown on the top) demonstrates the process of flame development just after the ignition and the set of images at the bottom represents dynamic flame structures after the flame has been stabilized. It can be observed that it took almost 30 ms after the ignition to stabilize the flame on the jet burner. It should be noted that all the images were corrected for the variations in intensity along the vertical axis using the beam profile shown in Figure 6.11. The OH-PLIF signal is negligible along the central cone because of the presence of cold reactants coming out of the nozzle along the

central axis. However, peak OH-PLIF signal is at the two flame fronts, where enough oxidizer is present for combustion. Further, local ignition and extinction events along with the flame wrinkling can be clearly observed from the consecutive single-laser-shot OH-PLIF images. Lastly, the S/N ratio was obtained at the ratio of the mean value of the signal and standard deviation of the signal corresponding to 0.8 mm x 0.8 mm area of the flame. However, the peak value of S/N was approximately 25. The S/N ratio is slightly lower compared to the one obtained in our previous work (using OPA) [55], it is mainly because of larger laser sheet height (~45 mm) in this study as compared to ~15 mm laser sheet used in the previous study. It should be noted that previously we could not make a 45-mm sheet because of low power output (~ 30 μJ/pulse) from the OPA. Therefore, OH-PLIF detection using THG can be more advantageous compared to OPA when diagnosing in complex flow fields of practical interest.

6.3 Atomic Carbon and Oxygen Detection

This section will highlight more applications in which direct frequency tuning setup can be advantageous compared to commercial OPA to detect minor intermediate species having excitation wavelengths in UV and VUV regions.

6.3.1 Atomic Carbon (C-atom) Detection

C-atom can be excited from the ground state $2p^2\ ^3P \rightarrow\rightarrow 2p3p\ ^3P$ via 2-photon excitation at an excitation wavelength of around 280-nm (as shown in Figure 6.14) and the fluorescence emission resulting from transition $2p3p\ ^3P \rightarrow 2p3s\ ^3P$ can be detected in the range of 906-913 nm [139, 140]. Other 2p excitation schemes for C-atom have also been demonstrated by researchers [141-144].

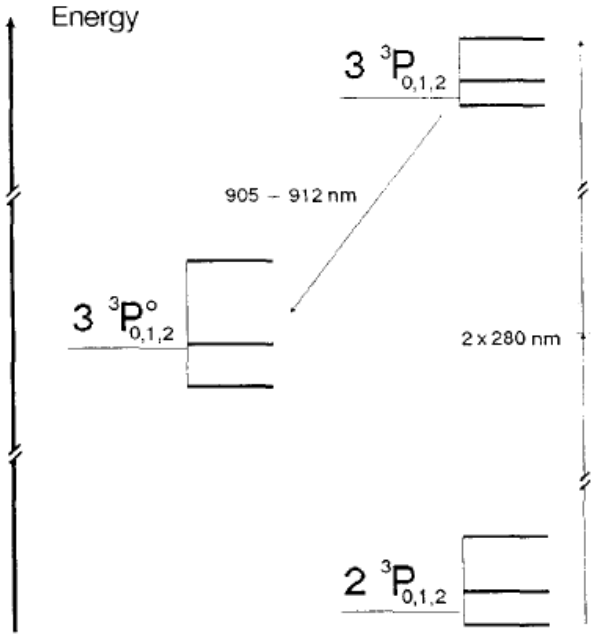

Figure 6.14: Schematic of the energy level diagram of C-atom reprinted from [139].

Figure 6.15 shows the excitation and emission spectra in C-atom at different transitions recorded at 100 torrs in a C_2H_2/O_2 flame.

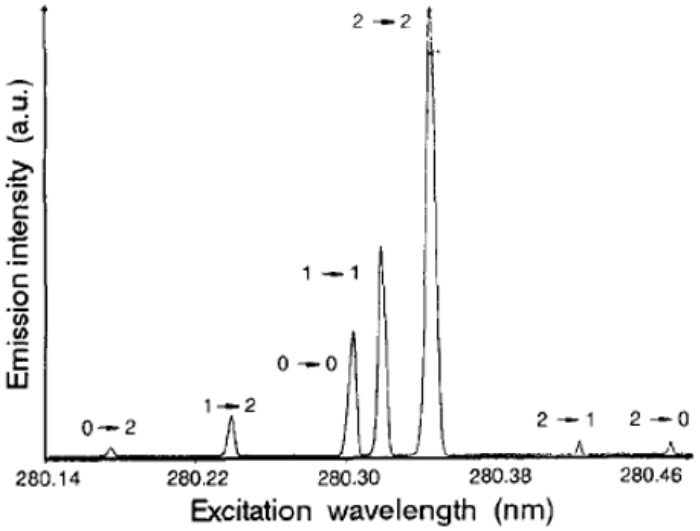

(a)

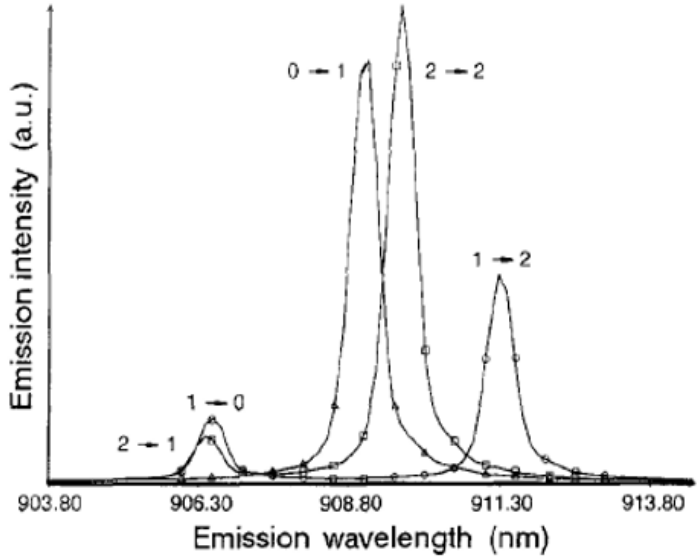

(b)

Figure 6.15: (a) Excitation (b) Emission spectra in C-atom recorded for different transitions reprinted from [139]

The authors have mentioned various attempts in the past that were unsuccessful in detecting C-atom via LIF; therefore, the emission spectra are shown in Figure 6.15 (b) had

been recorded via stimulated emission (SE) (being 10^4 times stronger than LIF). However, the quantification of the SE signal was questionable.

In our direct frequency tuning setup, we changed the fundamental pump beam wavelength to 840-nm, thereby, generating a THG broadband fs pulse of wavelength 280-nm with average pulse energy of 90 μJ/pulse. In order to detect C-atom, rich C_2H_4/air flames ($\Phi = 1.6$ and $\Phi = 1.7$) were established on the Mckenna burner. The pulse energy was modulated by putting a variable neutral density filter in the beam path. The beam was focused on the flame using a converging lens of focal length +200 mm (the pulse energy was reduced in order to avoid the plasma generation at the focal point). In order to detect the fluorescence signal, a spectrometer (Model: IsoPlane 320; Princeton Instruments) with 300 lines/mm grating was setup. The ICCD gate width was 50 ns and the gain was set at 100% with 700 laser shot on-CCD accumulations. In principle, this is capable of exciting all the lines shown in Figure 6.15 (a). However, we were unsuccessful in detecting C-atom in hydrocarbon flames via 2pLIF. This result is primarily due to the weaker absorption cross-section of C-atom at this excitation wavelength, resulting in a very weak fluorescence signal (similar observations have been mentioned by other researchers as well). Further, significant amount of photo-chemically generated C-atom is produced in the hydrocarbon flames which is substantially higher in concentration as compared to the natural C-atoms, making their detection even more difficult in sooting flames via LIF.

6.3.2 Atomic Oxygen (O-atom) Detection

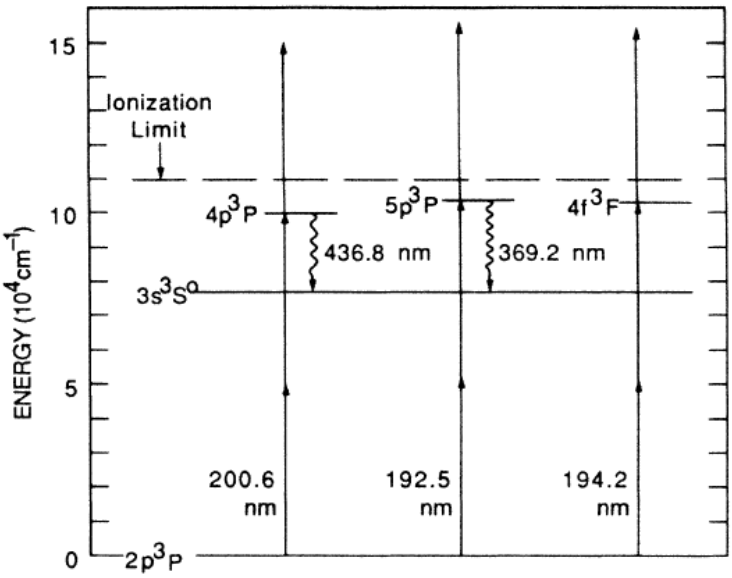

Figure 6.16: Energy level diagram of O-atom depicting various VUV 2p excitation schemes reprinted from [145].

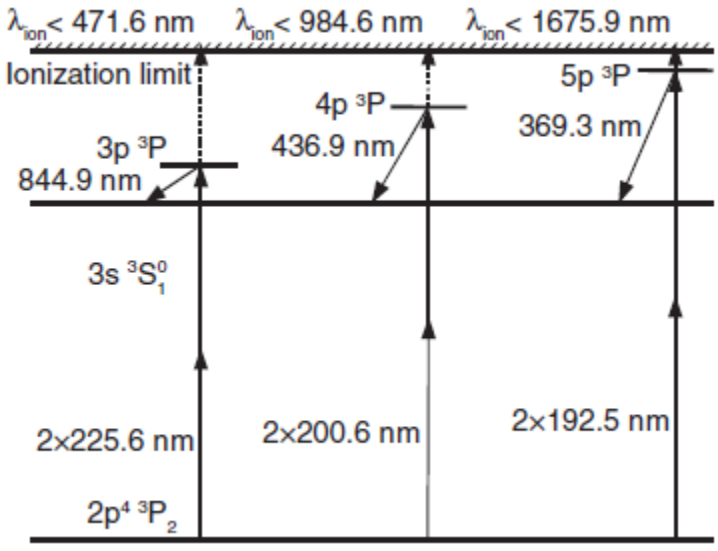

Figure 6.17: Schematic of the energy level diagram of O-atom reprinted from [8].

Figure 6.16 and Figure 6.17 represents various 2p excitation schemes in O-atom. O-atom can be excited from the ground state $2p^4\ ^3P \rightarrow\rightarrow 2p^3 4p\ ^3P$ via 2-photon excitation at an excitation wavelength of around 200-nm (as shown in Figure 6.17) and the fluorescence emission resulting from transition $4p\ ^3P \rightarrow 3s\ ^3S$ can be detected at around 437-nm in the visible spectrum. However, it should be noted that this excitation scheme has not been experimentally demonstrated so far, mainly because of the low pulse energy available in the VUV range around 200-nm.

In our direct frequency tuning setup, we changed the fundamental pump beam wavelength to 800-nm, thereby, generating an FHG broadband fs pulse of wavelength 200-nm with an average pulse energy of around 30 μJ/pulse. We tried to detect the O-atom in CH_4/air flame established over the Hencken burner at $\Phi = 1.0$. The beam was focused on the flame using a converging lens of focal length +200 mm (the pulse energy was reduced in order to avoid the plasma generation at the focal point). In order to detect the fluorescence signal, a spectrometer (Model: IsoPlane 320; Princeton Instruments) with 300 lines/mm grating was setup. The ICCD gate width was 50 ns and the gain was set at 100% with 1000 laser shot on-CCD accumulations. However, we were unsuccessful in detecting O-atom using the above mentioned 2p excitation scheme . The strength of the fluorescence emission at 437-nm was very weak and could not be easily detected. This is primarily because of the excitation in the VUV region which significantly limits the absorption cross-sections and the excited state population [145, 146].

6.4 Summary

Optical parametric amplifiers (OPA) are traditionally being used for frequency conversion of the ultrashort pulses from IR to UV; however, the implementation of OPA is limited by its low conversion efficiency. As a result, the output UV beam generated from OPA does not have enough pulse energy for the excitation and detection of minor intermediate species. Therefore, as an alternative to OPA, direct frequency tuning schemes using non-linear BBO crystals were discussed. In this study, the fundamental beam wavelength (set at 850-nm) was used to generate THG fs pulse centered at 283.3-nm with an average pulse energy of 90 μJ/pulse. The THG beam was used to detect OH radical in H_2/air flame established over the Hencken calibration burner. Further, high-resolution OH spectra in C_2H_4/air flames were recorded and the results were compared with the simulated spectra and previous experimental results. Lastly, a laser sheet was used to study the 2D flame development and dynamic flame structure via OH detection in CH_4/H_2 (1:1) diffusion flame established over the Bunsen jet burner. Overall, per-pulse conversion efficiency of ~ 4.5% (~14% more than what has been reported by researchers previously) around 283-nm at 1kHz was achieved as compared to below 0.6 % conversion efficiency of OPA. Therefore, this more efficient and compact system is a significant leap towards the diagnostics of various species of interest (such as N, O and Kr), whose detection is very challenging mainly because of the limited pulse energies available in the UV and VUV regime.

7 CONCLUSION AND RECOMMENDATIONS FOR FUTURE WORK

7.1 Conclusion

Laser diagnostics using ultrashort fs laser pulses have been demonstrated for the detection of minor intermediate species of H-atom and OH radicals in harsh environments and complex flow fields by implementing LIF as the primary detection technique. Further, because of their broadband nature and low average power, fs pulses offer several advantages over traditionally used ns and ps pulses in terms of higher multi-photon excitation efficiency, lower photolytic interferences, and high-repetition-rate imaging. Over the past few years, fs pulses are being implemented for the detection of H-atom and OH radicals. In this study, we implemented these existing methodologies to understand more complex combustion chemistry of soot formation by determining the role of H-atom concentration on soot formation pathways. The spatially resolved soot volume fraction, f_V was obtained using LII, and relative H-atom concentration profiles were generated using the recently demonstrated fs-2pLIF technique. 2-D LII images were obtained using three different excitation/detection wavelength schemes. A strong dependence of f_V and [H] on the flame temperature was observed. It was concluded that the lower flame temperatures result in reduced [H] and may promote soot formation. This study can be a significant step forward in developing and validating 2-D flame models for rich hydrocarbon flames, taking into account the soot formation mechanisms and the role of key reactive intermediates such as H-atoms.

It has been realized that the existing 2pLIF detection scheme (using $\lambda = 205$ nm) for H-atoms can be problematic in devices containing thick transmissive optics because

of the absorption of deep-UV wavelengths. Moreover, DUV wavelengths are susceptible to photolytic production at higher excitation pulse energies. Thus, 3p excitation scheme of H-atom by using red-shifted 307.7-nm fs laser pulses was investigated. In the range of 3p pulse energies investigated, no photolytic interferences and SE were observed. However, the typical 3pLIF signal is approximately a factor of 40 weaker than 2pLIF signals because of weaker 3p absorption cross-sections. However, the 3pLIF scheme utilizes red-shifted UV photons near 307-nm, thereby making it more suitable for diagnostics in realistic combustion hardware containing thick optical windows.

The utilization of this new LIF scheme also enabled the extension of the existing diagnostics for simultaneous multi-species imaging. As a result, simultaneous detection of H-atom (via 3pLIF) and OH (via single-photon LIF) was demonstrated using the excitation wavelength of $\lambda = 307.7$ nm. The simultaneous detection provides an insight for the understanding of light species transport and preferential diffusion via determination of the spatial location of H-atom formation and consumption with respect to the reaction zone marked by OH radicals.

Optical parametric amplifiers (OPA) are traditionally used for frequency conversion of the ultrashort pulses from near-IR to UV regimes for fs-laser diagnostics experiments. However, the implementation of OPA is limited by its low conversion efficiency which, results in low output UV pulse energy which is usually insufficient for single-laser-shot 2-D imaging of intermediate species such as H, OH, and O in practical flow fields. Therefore, as an alternative to OPA, direct frequency conversion schemes using nonlinear BBO crystals are discussed. An average pulse energy of 90 μJ/pulse is

reported, when pumped by 2mJ/pulse of 850-nm input. The THG beam was used to detect OH radicals in different flames. Overall, per-pulse conversion efficiency of ~ 4.5% (~ 14% more than what has been reported by in previous studies) around 283-nm at 1 kHz was achieved. The present THG system is not only more efficient, but also compact, stable and economical than commercial OPA systems, hence a significant step towards the OH PLIF diagnostics of various flames of practical relevance.

7.2 Recommendations for Future Work

It has been realized that quantitative measurement of minor intermediate species using incoherent techniques like LIF is very challenging, particularly because these techniques are limited by their dependence on collisional quenching. The sensitivity of LIF on pressure, temperature, and species-dependent collisions result in inaccuracies in quantifying the fluorescence quantum yields. For LIF, the uncertainty in measurement is linearly proportional to the uncertainty in determining the quenching rates. Therefore, as an alternative, coherent techniques, with similar detection sensitivity as that of LIF, like degenerate four-wave mixing (DFWM) can be used for the detection of intermediate species in different laboratory flames using femtosecond laser pulses. Further, DFWM is not explicitly sensitive to quenching. It should be noted that DFWM has been demonstrated in the past, but was limited in terms of detection efficiency due to the availability of nanosecond and picosecond laser systems. Thus we believe that the implementation of fs-laser pulses will add a new dimension to this prior research.

Further, all the experimentation in this study has been performed in the atmospheric pressure flames. It would be very interesting to study the ultra-short pulse

laser diagnosis in practically relevant high-pressure combustion systems. In our laboratory, we are in the process of setting up a high-pressure burner for such follow-on studies. We believe that the investigation of H-atoms using the FHG scheme and OH radical using the THG scheme in high-pressure flames using the direct frequency conversion system will take us a step closer in understanding the reaction chemistry in actual combustion systems such as internal combustion engines and gas turbines that operate at very high pressures.

REFERENCES

[1] M.J. Dyer, D.R. Crosley, Two-dimensional imaging of OH laser-induced fluorescence in a flame, Optics Letters 7 (1982) 382-384.

[2] G. Kychakoff, R.D. Howe, R.K. Hanson, J.C. McDaniel, Quantitative visualization of combustion species in a plane, Applied Optics 21 (1982) 3225-3227.

[3] J.A. Gray, R. Trebino, Two-photon-resonant four-wave-mixing spectroscopy of atomic hydrogen in flames, Chemical Physics Letters 216 (1993) 519-524.

[4] K. Niemi, V.S.-v.d. Gathen, H.F. Döbele, Absolute atomic oxygen density measurements by two-photon absorption laser-induced fluorescence spectroscopy in an RF-excited atmospheric pressure plasma jet, Plasma Sources Science and Technology 14 (2005) 375.

[5] W.K. Bischel, B.E. Perry, D.R. Crosley, Detection of fluorescence from O and N atoms induced by two-photon absorption, Applied Optics 21 (1982) 1419-1429.

[6] B. Li, D. Zhang, J. Liu, Y. Tian, Q. Gao, Z. Li, A Review of Femtosecond Laser-Induced Emission Techniques for Combustion and Flow Field Diagnostics, Applied Sciences 9 (2019) 1906.

[7] A.C. Eckbreth, Laser diagnostics for combustion temperature and species, Abacus Press (1988) p. 630.

[8] H.F. Döbele, T. Mosbach, K. Niemi, V.S.-v.d. Gathen, Laser-induced fluorescence measurements of absolute atomic densities: concepts and limitations, Plasma Sources Science and Technology 14 (2005) S31.

[9] U. Czarnetzki, K. Miyazaki, T. Kajiwara, K. Muraoka, M. Maeda, H.F. Döbele, Comparison of various two-photon excitation schemes for laser-induced fluorescence spectroscopy in atomic hydrogen, Journal of Optical Society of Amercia B 11 (1994) 2155-2162.

[10] R.P. Lucht, J.T. Salmon, G.B. King, D.W. Sweeney, N.M. Laurendeau, Two-photon-excited fluorescence measurement of hydrogen atoms in flames, Optics Letters 8 (1983) 365-367.

[11] J.E.M. Goldsmith, Two-photon-excited stimulated emission from atomic hydrogen in flames, Journal of Optical Society of Amercia B 6 (1989) 1979-1985.

[12] J.E.M. Goldsmith, Two-step saturated fluorescence detection of atomic hydrogen in flames, Optics Letters 10 (1985) 116-118.

[13] J.E.M. Goldsmith, Photochemical effects in 205-nm, two-photon-excited fluorescence detection of atomic hydrogen in flames, Optics Letters 11 (1986) 416-418.

[14] J.T. Salmon, N.M. Laurendeau, Absolute concentration measurements of atomic hydrogen in subatmospheric premixed $H_2/O_2/N_2$ flat flames with photoionization controlled-loss spectroscopy, Applied Optics 26 (1987) 2881-2891.

[15] J. Bittner, K. Kohse-Höinghaus, U. Meier, S. Kelm, T. Just, Determination of absolute H atom concentrations in low-pressure flames by two-photon laser-excited fluorescence, Combustion and Flame 71 (1988) 41-50.

[16] J.E.M. Goldsmith, Multiphoton-excited fluorescence measurements of atomic hydrogen in low-pressure flames, Symposium (International) on Combustion 22 (1989) 1403-1411.

[17] J.T. Salmon, N.M. Laurendeau, Concentration measurements of atomic hydrogen in subatmospheric premixed C2H4/O2/Ar flat flames, Combustion and Flame 74 (1988) 221-231.

[18] L. Gasnot, P. Desgroux, J.F. Pauwels, L.R. Sochet, Improvement of two-photon laser induced fluorescence measurements of H- and O-atoms in premixed methane/air flames, Applied Physics B 65 (1997) 639-646.

[19] P. Ding, M. Ruchkina, Y. Liu, M. Alden, J. Bood, Femtosecond two-photon-excited backward lasing of atomic hydrogen in a flame, Optics Letters 43 (2018) 1183-1186.

[20] C. Winters, V. Petrishchev, Z. Yin, W.R. Lempert, I.V. Adamovich, Surface charge dynamics and OH and H number density distributions in near-surface nanosecond pulse discharges at a liquid / vapor interface, Journal of Physics D: Applied Physics 48 (2015) 424002.

[21] K. Niemi, V.S.-v.d. Gathen, H.F. Döbele, Absolute calibration of atomic density measurements by laser-induced fluorescence spectroscopy with two-photon excitation, Journal of Physics D: Applied Physics 34 (2001) 2330-2335.

[22] J.A. Gray, J.E.M. Goldsmith, R. Trebino, Detection of atomic hydrogen by two-color laser-induced grating spectroscopy, Optics Letters 18 (1993) 444-446.

[23] W. D. Kulatilaka, Two-color, two-photon laser-induced polarization spectroscopy (LIPS) measurements of atomic hydrogen in near-adiabatic, atmospheric pressure hydrogen/air flames, Combustion and Flame 137 (2004) 523-537.

[24] W.D. Kulatilaka, J.H. Frank, B.D. Patterson, T.B. Settersten, Analysis of 205-nm photolytic production of atomic hydrogen in methane flames, Applied Physics B 97 (2009) 227-242.

[25] W.D. Kulatilaka, J.H. Frank, T.B. Settersten, Interference-free two-photon LIF imaging of atomic hydrogen in flames using picosecond excitation, Proceedings of the Combustion Institute 32 (2009) 955-962.

[26] W.D. Kulatilaka, B.D. Patterson, J.H. Frank, T.B. Settersten, Comparison of nanosecond and picosecond excitation for interference-free two-photon laser-induced fluorescence detection of atomic hydrogen in flames, Applied Optics 47 (2008) 4672-4683.

[27] W.D. Kulatilaka, J.R. Gord, V.R. Katta, S. Roy, Photolytic-interference-free, femtosecond two-photon fluorescence imaging of atomic hydrogen, Optics Letters 37 (2012) 3051.

[28] C.A. Hall, W.D. Kulatilaka, J.R. Gord, R.W. Pitz, Quantitative atomic hydrogen measurements in premixed hydrogen tubular flames, Combustion and Flame 161 (2014) 2924-2932.

[29] C.A. Hall, R.W. Pitz, Numerical simulation of premixed H2–air cellular tubular flames, Combustion Theory and Modelling 20 (2016) 328-348.

[30] I.A. Mulla, A. Dowlut, T. Hussain, Z.M. Nikolaou, S.R. Chakravarthy, N. Swaminathan, R. Balachandran, Heat release rate estimation in laminar premixed flames using laser-induced fluorescence of CH2O and H-atom, Combustion and Flame 165 (2016) 373-383.

[31] W.D. Kulatilaka, J.R. Gord, S. Roy, Femtosecond two-photon LIF imaging of atomic species using a frequency-quadrupled Ti:sapphire laser, Applied Physics 116 (2014) 7-13.

[32] J. B Schmidt, S. Roy, W. Kulatilaka, I. Shkurenkov, I. V Adamovich, W. Lempert, J. R Gord, Femtosecond, two-photon-absorption, laser-induced-fluorescence (fs-TALIF) imaging of atomic hydrogen and oxygen in non-equilibrium plasmas, Journal of Physics D: Applied Physics 50 (2017) 17.

[33] M.G. Allen, R.K. Hanson. Planar Laser-Induced-Fluorescence Monitoring Of OH In A Spray Flame, Optical Engineering 25 (1986) 251309.

[34] N.M. Laurendeau, J.E.M. Goldsmith, Comparison of Hydroxyl Concentration Profiles using Five Laser-Induced Fluorescence Methods in a Lean Subatmospheric-Pressure H_2/O_2/Ar Flame, Combustion Science and Technology 63 (1989) 139-152.

[35] B. Yip, M.F. Miller, A. Lozano, R.K. Hanson, A combined OH/acetone planar laser-induced fluorescence imaging technique for visualizing combusting flows, Experiments in Fluids 17 (1994) 330-336.

[36] A. Cessou, D. Stepowski, Planar Laser Induced Fluorescence Measurement of [OH] in the Stabilization Stage of a Spray Jet Flame, Combustion Science and Technology 118 (1996) 361-381.

[37] M. Aldén, H. Edner, G. Holmstedt, S. Svanberg, T. Högberg, Single-pulse laser-induced OH fluorescence in an atmospheric flame, spatially resolved with a diode array detector, Applied Optics 21 (1982) 1236-1240.

[38] M. Sweeney, S. Hochgreb, Autonomous extraction of optimal flame fronts in OH planar laser-induced fluorescence images, Applied Optics 48 (2009) 3866-3877.

[39] X. Chen, T.B. Settersten, Investigation of OH X2Π collisional kinetics in a flame using picosecond two-color resonant four-wave-mixing spectroscopy, Applied Optics 46 (2007) 3911-3920.

[40] K.K. Venkatesan, J. Zhang, G.B. King, N.M. Laurendeau, M.W. Renfro, Hydroxyl space-time correlation measurements in partially premixed turbulent opposed-jet flames, Applied Physics B 89 (2007) 129-140.

[41] G.H. Dieke, H.M. Crosswhite, The ultraviolet bands of OH Fundamental data, Journal of Quantitative Spectroscopy and Radiative Transfer 2 (1962) 97-199.

[42] J.A. Coxon, Optimum molecular constants and term values for the X2Π($v \leq 5$) and A2Σ+($v \leq 3$) states of OH, Canadian Journal of Physics 58 (1980) 933-949.

[43] D.R. Crosley, G.P. Smith, Two-photon spectroscopy of the A 2Σ+–X 2Πi system of OH, The Journal of Chemical Physics 79 (1983) 4764-4773.

[44] K.L. Steffens, J. Luque, J.B. Jeffries, D.R. Crosley, Transition probabilities in OH A 2Σ+–X 2Πi: Bands with v′=2 and 3, The Journal of Chemical Physics 106 (1997) 6262-6267.

[45] J.E.M. Goldsmith, N.M. Laurendeau, Two-photon-excited fluorescence measurements of OH concentration in a hydrogen–oxygen flame, Applied Optics 25 (1986) 276-283.

[46] R.P. Lucht, D.W. Sweeney, N.M. Laurendeau, Laser-Saturated Fluorescence Measurements of OH in Atmospheric Pressure CH4/O2/N2 Flames Under Sooting and Non-Sooting Conditions, Combustion Science and Technology 42 (1985) 259-281.

[47] R.P. Lucht, D.W. Sweeney, N.M. Laurendeau, Laser-saturated fluorescence measurements of OH concentration in flames, Combustion and Flame 50 (1983) 189-205.

[48] R.P. Lucht, D.W. Sweeney, N.M. Laurendeau, M.C. Drake, M. Lapp, R.W. Pitz, Single-pulse, laser-saturated fluorescence measurements of OH in turbulent nonpremixed flames, Optics Letters 9 (1984) 90-92.

[49] R.J. Cattolica, S.R. Vosen, Two-dimensional measurements of the [OH] in a constant volume combustion chamber, Symposium (International) on Combustion 20 (1985) 1273-1282.

[50] P.H. Paul, H.N. Najm, Planar laser-induced fluorescence imaging of flame heat release rate, Symposium (International) on Combustion 27 (1998) 43-50.

[51] M.G. Allen, K.R. McManus, D.M. Sonnenfroh, P.H. Paul, Planar laser-induced-fluorescence imaging measurements of OH and hydrocarbon fuel fragments in high-pressure spray-flame combustion, Applied Optics 34 (1995) 6287-6300.

[52] B. Atakan, J. Heinze, U.E. Meier, OH laser-induced fluorescence at high pressures: spectroscopic and two-dimensional measurements exciting the A–X (1,0) transition, Applied Physics B 64 (1997) 585-591.

[53] G. Singla, P. Scouflaire, C. Rolon, S. Candel, Planar laser-induced fluorescence of OH in high-pressure cryogenic LOx/GH2 jet flames, Combustion and Flame 144 (2006) 151-169.

[54] A. Jain, Y. Wang, C. Schweizer, W.D. Kulatilaka, Investigation of Flow-Flame Interactions in Kerosene Piloted Liquid-Spray Flames Using Simultaneous OH and PAH PLIF, AIAA Scitech Forum (2020).

[55] Y. Wang, A. Jain, W. Kulatilaka, Hydroxyl radical planar imaging in flames using femtosecond laser pulses, Applied Physics B 125 (2019) 90.

[56] K. Smyth, P.J.H. Tjossem, A. Hamins, J.H. Miller, Concentration measurements of OH· and equilibrium analysis in a laminar methane-air diffusion flame, Combustion and flame 79 (1990) 366-380.

[57] J.M. Seitzman, R.K. Hanson, P.A. DeBarber, C.F. Hess, Application of quantitative two-line OH planar laser-induced fluorescence for temporally resolved planar thermometry in reacting flows, Applied Optics 33 (1994) 4000-4012.

[58] C. Kaminski, J. Hult, M. Aldén, High Repetition Rate Planar Laser Induced Fluorescence of OH in a Turbulent Non-Premixed Flame, Applied Physics B 68 (1999) 757–760.

[59] T.R. Meyer, S. Roy, T.N. Anderson, J.D. Miller, V.R. Katta, R.P. Lucht, J.R. Gord, Measurements of OH mole fraction and temperature up to 20 kHz by using a diode-laser-based UV absorption sensor, Applied Optics 44 (2005) 6729-6740.

[60] W.D. Kulatilaka, P.S. Hsu, J.R. Gord, S. Roy, Point and planar ultraviolet excitation/detection of hydroxyl-radical laser-induced fluorescence through long optical fibers, Optics Letters 36 (2011) 1818-1820.

[61] P. Hsu, W. Kulatilaka, S. Roy, A. Patnaik, J. Gord, Development of an All-Fiber-Coupled, Pulsed, Ultraviolet Laser-Induced-Fluorescence (UV-LIF) Detection System for OH Radicals in Practical Combustion Devices, AIAA Forum (2012) 1058.

[62] P.S. Hsu, W.D. Kulatilaka, S. Roy, J.R. Gord, Investigation of optical fibers for high-repetition-rate, ultraviolet planar laser-induced fluorescence of OH, Applied Optics 52 (2013) 3108-3115.

[63] P. Hsu, W. Kulatilaka, N. Jiang, S. Kostka, S. Roy, A. Patnaik, J. Gord. Fiber-Coupled High-Speed OH-PLIF Imaging in Turbulent Flames. In: editor^editors. 28th Aerodynamic Measurement Technology, Ground Testing, and Flight Testing Conference including the Aerospace T&E Days Forum (2012) 2881.

[64] K.W.D.G.J.R. Stauffer H U, S. Roy, Laser-induced fluorescence detection of hydroxyl (OH) radical by femtosecond excitation, Optics Letters 36 (2011) 1776.

[65] H.U. Stauffer, S. Roy, W.D. Kulatilaka, J.R. Gord, Detailed calculation of hydroxyl (OH) radical two-photon absorption via broadband ultrafast excitation, Journal of Optical Society America B 29 (2012) 40-52.

[66] T. Paschal, P. Parajuli, M. A. Turner, E. Petersen, W. Kulatilaka, High-Speed OH* and CH* Chemiluminescence Imaging and OH Planar Laser-Induced Fluorescence (PLIF) in Spherically Expanding Flames, AIAA Scitech Forum (2019) 0574.

[67] Y. Wang, A. Jain, W. Kulatilaka, Simultaneous measurement of CO and OH in flames using a single broadband, femtosecond laser pulse, Combustion and Flame 214 (2020) 358-360.

[68] B. Quay, T.W. Lee, T. Ni, R.J. Santoro, Spatially resolved measurements of soot volume fraction using laser-induced incandescence, Combustion and Flame 97 (1994) 384-392.

[69] R.L. Vander Wal, K.J. Weiland, Laser-induced incandescence: Development and characterization towards a measurement of soot-volume fraction, Applied Physics B 59 (1994) 445-452.

[70] M. Frenklach, H. Wang, Detailed modeling of soot particle nucleation and growth, Symposium (International) on Combustion 23 (1991) 1559-1566.

[71] M. Frenklach, Reaction mechanism of soot formation in flames, Physical Chemistry Chemical Physics 4 (2002) 2028-2037.

[72] A. Violi, A.F. Sarofim, T.N. Truong, Mechanistic pathways to explain H/C ratio of soot precursors, Combustion Science and Technology 174 (2002) 205-222.

[73] A. Violi, T.N. Truong, A.F. Sarofim, Kinetics of Hydrogen Abstraction Reactions from Polycyclic Aromatic Hydrocarbons by H Atoms, The Journal of Physical Chemistry A 108 (2004) 4846-4852.

[74] G. Blanquart, H. Pitsch, Analyzing the effects of temperature on soot formation with a joint volume-surface-hydrogen model, Combustion and Flame 156 (2009) 1614-1626.

[75] A.C. Eckbreth, Effects of laser-modulated particulate incandescence on Raman scattering diagnostics, Journal of Applied Physics 48 (1977) 4473-4479.

[76] R.J. Santoro, H.G. Semerjian, R.A. Dobbins, Soot particle measurements in diffusion flames, Combustion and Flame 51 (1983) 203-218.

[77] B. Axelsson, R. Collin, P.-E. Bengtsson, Laser-induced incandescence for soot particle size measurements in premixed flat flames, Applied Optics 39 (2000) 3683-3690.

[78] T. Mouton, X. Mercier, M. Wartel, N. Lamoureux, P. Desgroux, Laser-induced incandescence technique to identify soot nucleation and very small particles in low-pressure methane flames, Applied Physics B 112 (2013) 369-379.

[79] P. Desgroux, A. Faccinetto, X. Mercier, T. Mouton, D. Aubagnac Karkar, A. El Bakali, Comparative study of the soot formation process in a “nucleation” and a “sooting” low pressure premixed methane flame, Combustion and Flame 184 (2017) 153-166.

[80] Y. Wang, A. Makwana, S. Iyer, M. Linevsky, R.J. Santoro, T.A. Litzinger, J. O’Connor, Effect of fuel composition on soot and aromatic species distributions in

laminar, co-flow flames. Part 1. Non-premixed fuel, Combustion and Flame 189 (2018) 443-455.

[81] C.R. Shaddix, K.C. Smyth, Laser-induced incandescence measurements of soot production in steady and flickering methane, propane, and ethylene diffusion flames, Combustion and Flame 107 (1996) 418-452.

[82] B. Mewes, J.M. Seitzman, Soot volume fraction and particle size measurements withlaser-induced incandescence, Applied Optics 36 (1997) 709-717.

[83] C. Betrancourt, F. Liu, P. Desgroux, X. Mercier, A. Faccinetto, M. Salamanca, L. Ruwe, K. Kohse-Höinghaus, D. Emmrich, A. Beyer, A. Gölzhäuser, T. Tritscher, Investigation of the size of the incandescent incipient soot particles in premixed sooting and nucleation flames of n-butane using LII, HIM, and 1 nm-SMPS, Aerosol Science and Technology 51 (2017) 916-935.

[84] L.A. Melton, Soot diagnostics based on laser heating, Applied Opt. 23 (1984) 2201-2208.

[85] M.Y. Choi, A. Hamins, G.W. Mulholland, T. Kashiwagi, Simultaneous optical measurement of soot volume fraction and temperature in premixed flames, Combustion and Flame 99 (1994) 174-186.

[86] M.Y. Choi, G.W. Mulholland, A. Hamins, T. Kashiwagi, Comparisons of the soot volume fraction using gravimetric and light extinction techniques, Combustion and Flame 102 (1995) 161-169.

[87] T.R. Melton, A.M. Vincitore, S.M. Senkan, The effects of equivalence ratio on the formation of polycyclic aromatic hydrocarbons and soot in premixed methane flames, Symposium (International) on Combustion 27 (1998) 1631-1637.

[88] T.R. Melton, F. Inal, S.M. Senkan, The effects of equivalence ratio on the formation of polycyclic aromatic hydrocarbons and soot in premixed ethane flames, Combustion and Flame 121 (2000) 671-678.

[89] T. Aizawa, H. Kosaka, Y. Matsui, 2-D Imaging of Soot Formation Process in a Transient Spray Flame by Laser-induced Fluorescence and Incandescence Techniques, SAE International (2002).

[90] M. Hofmann, W.G. Bessler, C. Schulz, H. Jander, Laser-induced incandescence for soot diagnostics at high pressures, Applied Optics 42 (2003) 2052-2062.

[91] P. Desgroux, X. Mercier, K.A. Thomson, Study of the formation of soot and its precursors in flames using optical diagnostics, Proceedings of the Combustion Institute 34 (2013) 1713-1738.

[92] P.-E. Bengtsson, M. Aldén, Application of a pulsed laser for soot measurements in premixed flames, Applied Physics B 48 (1989) 155-164.

[93] F. Migliorini, S. De Iuliis, F. Cignoli, G. Zizak, How “flat” is the rich premixed flame produced by your McKenna burner?, Combustion and Flame 153 (2008) 384-393.

[94] M.F. Campbell, G.A. Bohlin, P.E. Schrader, R.P. Bambha, C.J. Kliewer, K.O. Johansson, H.A. Michelsen, Design and characterization of a linear Hencken-type burner, Review of Scientific Instruments 87 (2016) 115114.

[95] R.L. Vander Wal, Laser-induced incandescence: detection issues, Applied Optics 35 (1996) 6548-6559.

[96] F. Goulay, P.E. Schrader, L. Nemes, M.A. Dansson, H.A. Michelsen, Photochemical interferences for laser-induced incandescence of flame-generated soot, Proceedings of the Combustion Institute 32 (2009) 963-970.

[97] H.A. Michelsen, Probing soot formation, chemical and physical evolution, and oxidation: A review of in situ diagnostic techniques and needs, Proceedings of the Combustion Institute 36 (2017) 717-735.

[98] C. Schulz, B.F. Kock, M. Hofmann, H. Michelsen, S. Will, B. Bougie, R. Suntz, G. Smallwood, Laser-induced incandescence: recent trends and current questions, Applied Physics B 83 (2006) 333.

[99] M. Frenklach, H. Wang, Detailed Mechanism and Modeling of Soot Particle Formation, in: H. Bockhorn (Ed.), Soot Formation in Combustion: Mechanisms and Models, Springer Berlin Heidelberg, Berlin, Heidelberg, (1994) 165-192.

[100] H.F. Calcote, Mechanisms of soot nucleation in flames—A critical review, Combustion and Flame 42 (1981) 215-242.

[101] K.H. Homann, H.G. Wagner, Some new aspects of the mechanism of carbon formation in premixed flames, Symposium (International) on Combustion 11 (1967) 371-379.

[102] B.S. Haynes, H.G. Wagner, Soot formation, Progress in Energy and Combustion Science 7 (1981) 229-273.

[103] R. Lemaire, A. Faccinetto, E. Therssen, M. Ziskind, C. Focsa, P. Desgroux, Experimental comparison of soot formation in turbulent flames of Diesel and surrogate Diesel fuels, Proceedings of the Combustion Institute 32 (2009) 737-744.

[104] R. Lemaire, E. Therssen, P. Desgroux, Effect of ethanol addition in gasoline and gasoline–surrogate on soot formation in turbulent spray flames, Fuel 89 (2010) 3952-3959.

[105] R. Lemaire, E. Therssen, J.F. Pauwels, P. Desgroux, Experimental comparison of soot formation in turbulent flames of kerosene and surrogate model fuels, International workshop on combustion generated fine carbonaceous particles (2007) 13-16.

[106] R. Mansmann, T. Terheiden, P. Schmidt, J. Menser, T. Dreier, T. Endres, C. Schulz, LIISim: a modular signal processing toolbox for laser-induced incandescence measurements, Applied Physics B 124 (2018).

[107] A. D'Anna, M. Commodo, M. Sirignano, P. Minutolo, R. Pagliara, Particle formation in opposed-flow diffusion flames of ethylene: An experimental and numerical study, Proceedings of the Combustion Institute 32 (2009) 793-801.

[108] A. El Bakali, X. Mercier, M. Wartel, F. Acevedo, I. Burns, L. Gasnot, J.F. Pauwels, P. Desgroux, Modeling of PAHs in low pressure sooting premixed methane flame, Energy 43 (2012) 73-84.

[109] R.P. Bambha, H.A. Michelsen, Effects of aggregate morphology and size on laser-induced incandescence and scattering from black carbon (mature soot), Journal of Aerosol Science 88 (2015) 159-181.

[110] W. Boyette, S. Chowdhury, W. Roberts, Soot Particle Size Distribution Functions in a Turbulent Non-Premixed Ethylene-Nitrogen Flame, Flow, Turbulence and Combustion 98 (2017) 1173-1186.

[111] T. Mouton, X. Mercier, P.J.A.P.B. Desgroux, Isomer discrimination of PAHs formed in sooting flames by jet-cooled laser-induced fluorescence: application to the measurement of pyrene and fluoranthene, Applied Physics B 122 (2016) 123.

[112] S. Bejaoui, X. Mercier, P. Desgroux, E. Therssen, Laser induced fluorescence spectroscopy of aromatic species produced in atmospheric sooting flames using UV and visible excitation wavelengths, Combustion and Flame 161 (2014) 2479-2491.

[113] S. Bejaoui, R. Lemaire, E. Therssen, Analysis of Laser-Induced Fluorescence Spectra Obtained in Spray Flames of Diesel and Rapeseed Methyl Ester Using the Multiple-Excitation Wavelength Laser-Induced Incandescence Technique with IR, UV, and Visible Excitations, Combustion Science and Technology 187 (2015) 906-924.

[114] I.A. Mulla, B. Renou, Simultaneous imaging of soot volume fraction, PAH, and OH in a turbulent n-heptane spray flame, Combustion and Flame 209 (2019) 452-466.

[115] D. Gu, Z. Sun, B.B. Dally, P.R. Medwell, Z.T. Alwahabi, G.J. Nathan, Simultaneous measurements of gas temperature, soot volume fraction and primary particle diameter in a sooting lifted turbulent ethylene/air non-premixed flame, Combustion and Flame 179 (2017) 33-50.

[116] S.E. Stein, J.A. Walker, M.M. Suryan, A. Fahr, A new path to benzene in flames, Symposium (International) on Combustion 23 (1991) 85-90.

[117] M. Frenklach, D.W. Clary, W.C. Gardiner, S.E. Stein, Detailed kinetic modeling of soot formation in shock-tube pyrolysis of acetylene, Symposium (International) on Combustion 20 (1985) 887-901.

[118] B.S. Jacob, S. Brian, S. James, R.G. James, R. Sukesh, Comparison of femtosecond- and nanosecond-two-photon-absorption laser-induced fluorescence (TALIF) of atomic oxygen in atmospheric-pressure plasmas, Plasma Sources Science and Technology 26 (2017) 055004.

[119] A. Jain, Y. Wang, W.D. Kulatilaka, Effect of H-atom concentration on soot formation in premixed ethylene/air flames, Proceedings of the Combustion Institute 37 (2019) 1289-1296.

[120] F. Vestin, M. Afzelius, C. Brackmann, P.-E. Bengtsson, Dual-broadband rotational CARS thermometry in the product gas of hydrocarbon flames, Proceedings of the Combustion Institute 30 (2005) 1673-1680.

[121] C. Meißner, J.W. Tröger, D.N. Kozlov, F. Beyrau, T. Seeger, Three-color vibrational CARS thermometry of fuel-rich ethylene/air flames using a potassium gadolinium tungstate Raman-active crystal as a source of narrowband probe radiation, Applied Optics 56 (2017) 77-83.

[122] G.C. Bjorklund, R.R. Freeman, R.H. Storz, Selective excitation of Rydberg levels in atomic hydrogen by three photon absorption, Optics Communications 31 (1979) 47-51.

[123] G.C. Bjorklund, C.P. Ausschnitt, R.R. Freeman, R.H. Storz, Detection of atomic hydrogen and deuterium by resonant three-photon ionization, Applied Physics Letters 33 (1978) 54-56.

[124] P.J.H. Tjossem, T.A. Cool, Detection of atomic hydrogen in flames by resonance four-photon ionization at 365 nm, Chemical Physics Letters 100 (1983) 479-483.

[125] J.E.M. Goldsmith. Multiphoton excitation techniques for combustion diagnostics, American Institute of Physics Conference Series (1986) 279.

[126] M. Aldén, A.L. Schawlow, S. Svanberg, P.L. Zhang, W. Wendt, Three-photon-excited fluorescence detection of atomic hydrogen in an atmospheric-pressure flame, Optics Letters 9 (1984) 211-213.

[127] J.E.M. Goldsmith, N.M. Laurendeau, Single-laser two-step fluorescence detection of atomic hydrogen in flames, Optics Letters 15 (1990) 576-578.

[128] K.E. Bertagnolli, R.P. Lucht, M.N. Bui-Pham, Atomic hydrogen concentration profile measurements in stagnation-flow diamond-forming flames using three-photon excitation laser-induced fluorescence, Journal of Applied Physics 83 (1998) 2315-2326.

[129] A. Brockhinke, A. Bülter, J.C. Rolon, K.J.A.P.B. Kohse-Höinghaus, ps-LIF measurements of minor species concentration in a counterflow diffusion flame interacting with a vortex, Applied Physics B 72 (2001) 491-496.

[130] D. Kiselev, L. Bonacina, J.-P. Wolf, Individual bioaerosol particle discrimination by multi-photon excited fluorescence, Optics Express 19 (2011) 24516-24521.

[131] B. Van Zyl, H. Neumann, H.L. Rothwell, R.C. Amme, Balmer-alpha and Balmer-beta emission cross sections for H+Ar collisions, Physical Review A 21 (1980) 716-729.

[132] A. Jain, Y. Wang, W.D. Kulatilaka, Three-photon-excited laser-induced fluorescence detection of atomic hydrogen in flames, Optics Letters 44 (2019) 5945-5948.

[133] V.R. Katta, L.P. Goss, W.M. Roquemore, Numerical investigations of transitional H2/N2 jet diffusion flames, AIAA Journal 32 (1994) 84-94.

[134] V.R. Katta, W.M. Roquemore, Numerical studies on the structure of two-dimensional H2/air premixed jet flame, Combustion and Flame 102 (1995) 21-40.

[135] W.D. Kulatilaka, J.R. Gord, V.R. Katta, S. Roy, Photolytic-interference-free, femtosecond two-photon fluorescence imaging of atomic hydrogen, Optics Letters 37 (2012) 3051-3053.

[136] J. Ringling, G. Korn, J. Squier, O. Kittelmann, F. Noack, Tunable femtosecond pulses in the near vacuum ultraviolet generatedby frequency conversion of amplified Ti:sapphire laser pulses, Optics Letters 18 (1993) 2035-2037.

[137] F. Rotermund, V. Petrov, Generation of the fourth harmonic of a femtosecond Ti:sapphire laser, Optics Letters 23 (1998) 1040-1042.

[138] V. Petrov, F. Rotermund, F. Noack, J. Ringling, O. Kittelmann, R. Komatsu, Frequency conversion of Ti:sapphire-based femtosecond laser systems to the 200-nm spectral region using nonlinear optical crystals, IEEE Journal of Selected Topics in Quantum Electronics 5 (1999) 1532-1542.

[139] M. Aldén, P.-E. Bengtsson, U. Westblom, Detection of carbon atoms in flames using stimulated emission induced by two-photon laser excitation, Optics Communications 71 (1989) 263-268.

[140] U. Westblom, P.E. Bengtsson, M. Aldén, Carbon atom fluorescence and C2 emission detected in fuel-rich flames using a UV laser, Applied Physics B 52 (1991) 371-375.

[141] P. Das, G.S. Ondrey, N.v. Veen, R. Bersohn, Two photon laser induced fluorescence of carbon atoms, The Journal of Chemical Physics 79 (1983) 724-726.

[142] R.L. Whetten, K.J. Fu, R.S. Tapper, E.R. Grant, Highly efficient production of neutral carbon atoms in the ultraviolet multiphoton fragmentation of aromatic molecules, The Journal of Physical Chemistry 87 (1983) 1484-1487.

[143] P.J.H. Tjossem, K.C. Smyth, Multiphoton ionization detection of CH, carbon atoms, and O2 in premixed hydrocarbon flames, Chemical Physics Letters 144 (1988) 51-57.

[144] H. Bergström, H. Hallstadius, H. Lundberg, A. Persson, Detection of carbon using amplified laser-induced fluorescence, Chemical Physics Letters 155 (1989) 27-31.

[145] D.J. Bamford, R.P. Saxon, L.E. Jusinski, J.D. Buck, W.K. Bischel, Two-photon excitation of atomic oxygen at 200.6, 192.5, and 194.2 nm: Absolute cross sections and collisional ionization rate constants, Physical Review A 37 (1988) 3259-3269.

[146] D.J. Bamford, L.E. Jusinski, W.K. Bischel, Absolute two-photon absorption and three-photon ionization cross sections for atomic oxygen, Physical Review A 34 (1986) 185-198.